CHALMERS
UNIVERSITY OF TECHNOLOGY

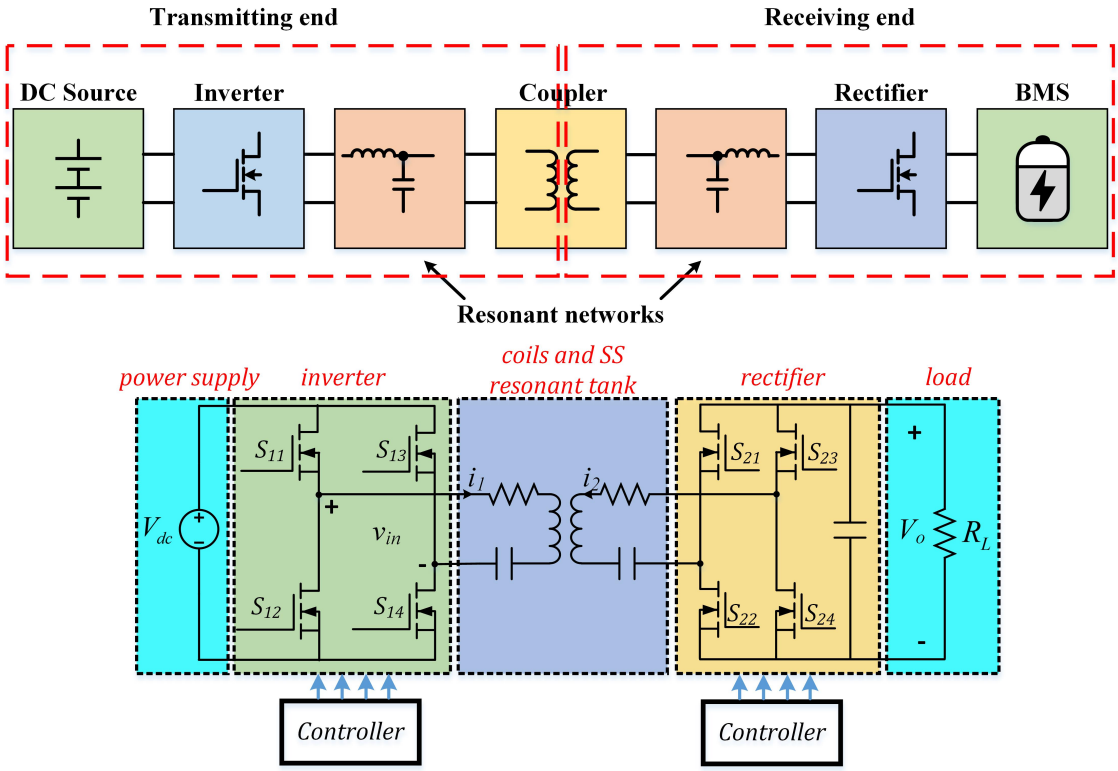

Modeling and Control of Inductive Power Transfer System with Misalignment and Load Independence

Master's thesis in Sustainable Electric Power Engineering and Electromobility

Linhua Lai

DEPARTMENT OF ELECTRICAL ENGINEERING
CHALMERS UNIVERSITY OF TECHNOLOGY
Gothenburg, Sweden 2024
www.chalmers.se

Master's thesis 2024

Modeling and Control of Inductive Power Transfer System with Misalignment and Load Independence

Linhua Lai

CHALMERS
UNIVERSITY OF TECHNOLOGY

Department of Electrical Engineering
Division of Power Engineering
Chalmers University of Technology
Gothenburg, Sweden 2024

Modeling and Control of Inductive Power Transfer System with Misalignment and Load Independence
LINHUA LAI

Supervisor: Junfei Tang, Chalmers University of Technology
Examiner: Yujing Liu, Chalmers University of Technology

Master's Thesis 2024
Department of Electrical Engineering
Division of Power Engineering
Chalmers University of Technology
SE-412 96 Gothenburg
Telephone +46 31 772 1000

Cover: Schematic of The Inductive Power Transfer System under Investigation

Typeset in LaTeX
Printed by Chalmers Reproservice
Gothenburg, Sweden 2024

Modeling and Control of Inductive Power Transfer System with Misalignment and Load Independence
LINHUA LAI
Department of Electrical Engineering
Chalmers University of Technology

Abstract

Inductive Power Transfer (IPT) presents a promising solution for electric vehicles (EVs), yet challenges persist in achieving high tolerance against coupling and load variations. To address this issue, new model and control scheme for IPT system are required. This thesis is dedicated to the modeling and control of an IPT system with a focus on misalignment and load tolerance.

To understand the properties and performance of the IPT system, this thesis begins with an investigation into the conventional model of an IPT system with a series-series resonant tank. Using the Finite Element Method (FEM), the electromagnetic field around the magnetic coupler is studied, providing insights into the relationship between misalignment and mutual inductance. Subsequently, an equivalent circuit is constructed for the IPT system. It becomes evident that under the conventional control scheme, the system's output power and efficiency are vulnerable to misalignment variations, posing a significant obstacle in power flow management.

To address this challenge, a novel digital control strategy is proposed. By synchronizing the inverter output voltage with the transmitter current, constant output power can be achieved in high coupling conditions. The control circuit is simple, as it only captures the zero crossing of the current in the transmitting coil. However, inherent propagation delays in the measurement and control circuit can lead to frequency drift and high switching losses, thereby compromising system efficiency and output power. In response, a digital control scheme with delay compensation is introduced, and the boundary of soft switching operation is investigated. It is concluded that soft switching operation can be achieved by applying the new control strategy. Experimental results reveal that within a misalignment range of $0-160$mm, the system maintains nearly constant output power. A peak efficiency of 92% can be attained when soft switching is realized in the inverter. This proposed control scheme enhances the robustness of the IPT system against misalignment variations, facilitating cost-effective hardware implementation and obviating the need for dual-side communication. However, the variation of load during power transfer can still cause change in output power.

Further analysis of power flow under various load conditions reveals the system's sensitivity to load variations. Leveraging the grid-connected rectifier, the DC-link voltage, crucial for the IPT system's output power, can be controlled to address the issue. Thus, the voltage controller of a three-phase Vienna rectifier is designed. Simulation results demonstrate that the rectifier has less than 1V output voltage ripple under 800V DC-link output voltage and 50kW output power, with a total

harmonic distortion of input current of 2.67%. Notably, the stability of the IPT system remains unaffected by variations in the DC-link voltage. Furthermore, the proposed control strategy provides more flexibility to the charging system without requiring additional DC-DC converters.

This thesis addresses the key challenges in IPT system design and control, offering innovative solutions to achieve robust, efficient, and adaptable EV charging systems. The proposed control schemes provide constant output power despite changes in coupling and load conditions. Therefore, the works in this thesis pave the way for the development of versatile, compact, and lightweight IPT systems.

Keywords: inductive power transfer, misalignment tolerance, digital control, power flow control, dual active bridge, three-phases rectifier, electromagnetic field, soft switching operation.

Acknowledgements

I would like to express my sincere gratitude to my supervisor, Dr. Junfei Tang, and my examiner, Prof. Yujing Liu, for their exceptional support, insightful advice, invaluable guidance throughout the entire process of this thesis, and generous permission to utilize laboratory equipment.

I am also deeply thankful to Dr. Jiasheng Huang from DTU for engaging discussions and sharing experiences. His suggestions played a pivotal role in shaping the direction of this thesis.

I am deeply indebted to my friends and colleagues for their encouragement, and kindness during the challenging times of this academic journey. Their support provided much-needed morale boosts and moments of respite.

Lastly, my deepest appreciation goes to my family, especially to my love, Bingher, for her unyielding belief in my abilities and her warm company throughout the chill winter. I would like to express my sincere thanks to my parents, for their unwavering support and encouragement.

Once again, thank you all for your contributions, guidance, and encouragement over the years.

Linhua Lai, Gothenburg, April 2024

List of Acronyms

Below is the list of acronyms that have been used throughout this thesis listed in alphabetical order:

AC	Alternating Current
DAB	Dual Active Bridge
DC	Direct Current
DD	Double-D
D-S	Drain to Source
DSP	Digital Signal Processor
EMI	Electromagnetic Interference
EV	Electrical Vehicle
IPT	Inductive Power Transfer
IR	Infrared
MOSFET	Metal Oxide Semiconductor Field Effect Transistor
PFC	Power Factor Correction
PT	Parity-Time
PWM	Pulse Width Modulation
RMS	Root Mean Square
SiC	Silicon Carbide
SS	Series-Series
WPT	Wireless Power Transfer
ZVS	Zero Voltage Switching

Contents

List of Figures

List of Tables

1

Introduction to Inductive Power Transfer Technology

1.1 Problem Background

Due to the unsustainable patterns of consumption and production, the global surface temperature was 1.09 °C higher in 2011-2020 than that in 1850-1900. The widespread and rapid climate changes have caused adverse impacts and damage to nature and human. The climate change has become a pivotal issue in the twenty-first century [1].

Research indicates that the surge in global greenhouse gas emission is one of the main reason for the rapid climate change. Thus, reducing the greenhouse gas emissions has become one of the global goals for a sustainable development. Around 14% of global greenhouse gas emissions originate from the transportation sector [2]. The majority of greenhouse gas emissions from transportation are carbon dioxide CO_2 emissions due to the usage of petroleum-based products in road, rail, air and marine transportation [3].

With an growing concern of the threat of greenhouse effect, the transportation sector is shifting from the internal combustion engine towards electric motor and the trend seems positive. For example, the global electric car sales has exceeded 10 million in 2022, which accounted for around 15% of global car market [4]. In Sweden, the marine transport sector is committed to developing a sustainable transportation to reduce the CO_2 and other hazardous gases emissions from the waterborne transport [5]. The electrification of ferries can largely ease the need of reducing the CO_2 emission.

Despite this progress, the widespread adoption of battery-powered electric vehicles (EVs) faces limitations, such as challenges related to the unsatisfying volume and cost of battery, the inconvenient of charging strategy for tight time schedule scenario such as ferry and bus. A solution that can provide a convenient, safe and reliable high-power charging service for the tight time schedule EVs is the inductive power transfer (IPT) technique. Compared with an conductive charing system, an IPT system has several advantages that can be listed as follows:

- **Longer lifetime and smaller size of battery**

Wireless charging introduces the possibilities to employ an opportunity charging strategy, which can be used flexibly to charge the bus fleets and ferries [6]. In situations where the stop time is short, traditional plug-in charging is impractical due to the time it takes to connect the cable. In such scenarios, the IPT system can serve as an efficient alternative to replace plug-in charging. This approach helps keep the state of charge (SOC) window small during each short charging period, contributing to an extended battery lifetime and a reduction in battery size [7, 8].

- **Longer lifetime of the charging system**
  The lifetime of an IPT charging system is prolonged because there is no mechanical wearout on the conductive parts. Additionally, IPT systems are considered safer than conductive charging systems since there are no exposed conductors, leading to less arcing and reduced safety risks [9].
- **Reliable in harsh environment**
  An IPT system works better in the harsh environment such as the quarry and mining industries, where driver-less vehicles are increasingly utilized due to repetitive works and less complex working environments.

Nevertheless, compared with cable charging system, IPT systems are more complex in terms of system structure and control strategy. The ancillary service, such as wireless communication and position alignment [10], might be required to guarantee an efficient and robust power transmission. In this thesis, the modelling and control of IPT system is going to be investigated. The objective is to achieve an IPT system with high robustness and efficiency. This thesis is mainly based on the research on the design of IPT system at Chalmers University of Technology by Daniel Pehrman and Yujing Liu [11].

1.2 State of Art in Inductive Power Transfer

1.2.1 Configuration of IPT System

As shown in Figure 1.1, a typical IPT system consists of a DC power source, inverter, resonant network, magnetic coupler, rectifier, and battery. Due to the additional requirement for controlling the inverter and rectifier, the IPT charging system has a more complex structure than a conductive charging system has. The inverter can be a single phase or multiple phases MOSFET inverter according to the application requirement. The rectifier can be either active bridge or diode bridge. The use of an active rectifier allows for tunable output power on the receiving end and bidirectional power transfer. However, an extra controller on the receiving end increases the cost and complexity of system.

Inductive power transfer is facilitated by a magnetic coupler, where an alternating current (AC) in the transmitting coil generates a time-varying magnetic field in space. This magnetic field induces a time-varying voltage on the receiving coil. To minimize the size of the ferrite core in the coupler, the switching frequency of the inverter is typically in the range of $10^1 \sim 10^2$ kHz to generate high frequency

voltage and current. Resonant networks, consisting of capacitors and inductors, can be added on the transmitting and receiving ends to increase the active power received by the load and reduce reactive power.

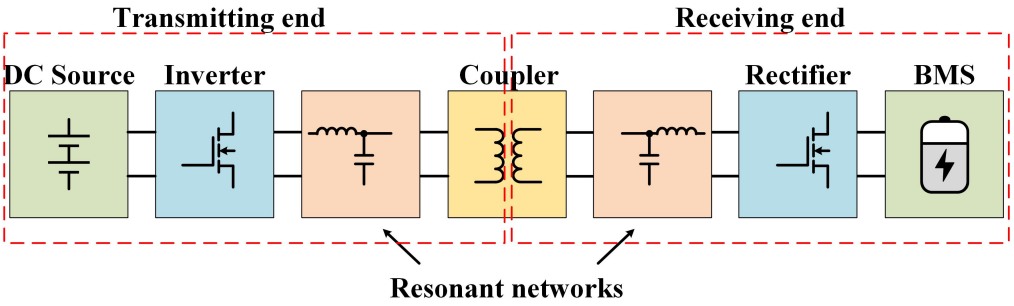

Figure 1.1: The configuration of IPT system

1.2.2 Category of IPT System Based on The Application

The IPT system can be categorized into two groups, each focusing on different applications:

- **Dynamic IPT system**
  This type is designed for applications involving moving vehicles or systems, such as electric buses, trams, or vehicles in motion. Dynamic IPT systems require continuous power transfer while the vehicle is in motion, making them suitable for scenarios like long trip electric transportation.
- **Stationary IPT system**
  This type is designed for stationary or quasi-stationary applications, such as EV charging stations or devices that remain in a fixed position during operation. Stationary IPT systems are commonly used in scenarios where the vehicle or device can pause for power transfer.

Different design considerations are employed for these applications to meet their respective practical requirements.

In a dynamic IPT application, EVs are being changed during the driving as illustrated in Figure 1.2. The charging infrastructure can be integrated into the road. This approach has the potential to offer virtually unlimited driving distance and can lead to a substantial reduction in on-board battery capacity. Consequently, this design results in lighter and smaller EV configurations [12]. Nevertheless, as the EV moves along the road, the coupling between the transmitting and receiving coils becomes time-variant, which may cause charging power variation and low efficiency issues. To mitigate this problem, the transmitting end can be designed with multiple transmitting modules. Each module can include multiple transmitting coils. By monitoring the position of the EV, the aligned transmitting modules can be activated for charging, enhancing efficiency and stability [13]. When the EV moves out of the specific charging range, the transmitting module is turned off and the

next module is turned on. The total mutual inductance between transmitting and receiving end is the sum of mutual inductance of all activated coils, which can be described as follows [14]:

$$M_{total} = \sum_{i=1}^{n} M_{tir} \tag{1.1}$$

where M_{tir} is the mutual inductance between ith transmitting coil and the receiving coil. Besides, to avoid the interaction between different transmitting coils, the coils in the transmitting modules shall be designed to reduce the mutual coupling M_{titj}.

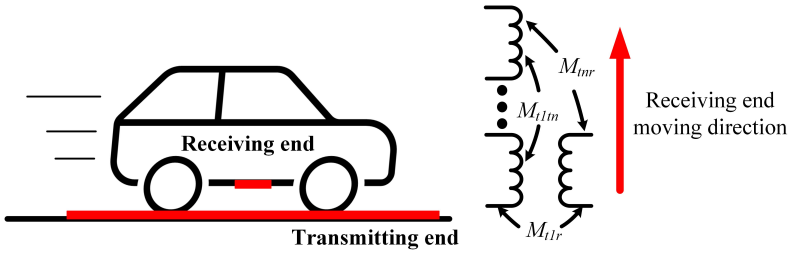

Figure 1.2: An illustration to a typical dynamic IPT system

A dynamic IPT infrastructure was installed and tested in Gotland island, Sweden in 2020 (see Figure 1.3) [15]. In this project, a 40-ton fully electric truck is charged on 1.65km of road. The truck drove at speeds reaching 80km/h and the dynamic IPT infracture provided an average power of 100kW during the charging. The report shows that the system has a high durability in extreme weather and the battery size is much smaller than many proposed battery capacities for electric heavy good vehicles.

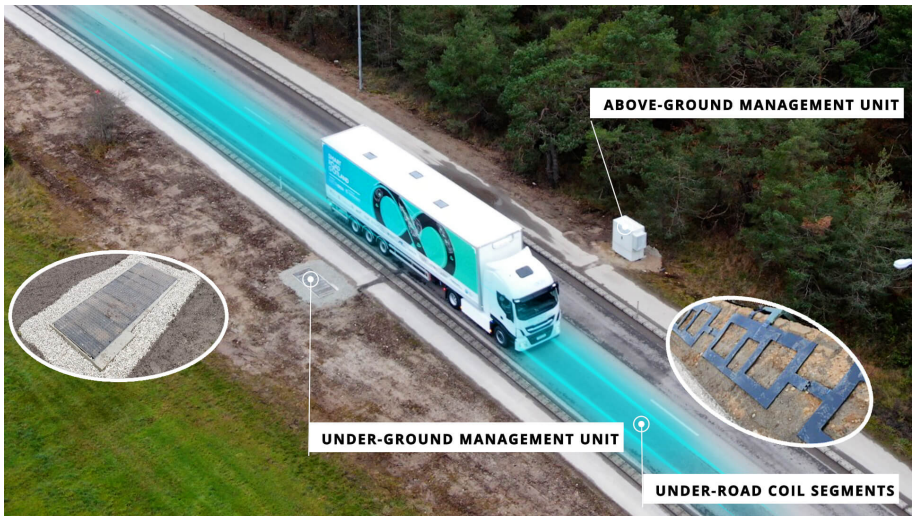

Figure 1.3: An example of dynamic IPT system in Gotland, Sweden

Different from a dynamic IPT system, in a stationary IPT scenario, stationary charging occurs when the vehicle is parked. The coupling between the coils is time-invariant once the vehicle stops. Charging can start and continue as long as the

transmitting and receiving coils are fully or partially aligned. Thus, the design of multiple modules is unnecessary in a stationary IPT system. As a result, the charging system is simpler, and the structure is more cost-efficient compared with a dynamic IPT system, as all the coils are used in charging, and there is no need to switch among coil modules.

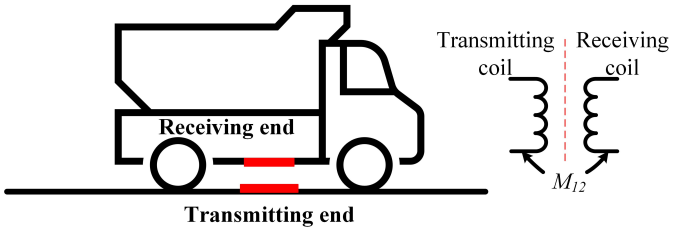

Figure 1.4: An illustration of a typical stationary IPT system

An electrical coastal car ferry "MF Folgefonn", operating with stationary IPT system was built in Norway in 2015 by Wärtsilä [16]. As shown in Figure 1.5, the transmitting end is built on the dock. The charging station is equipped with a machine arm that positions the transmitting pad to align with the receiving pad on the ferry. According to the report, the shore and ferry are connected by Wi-Fi once the ferry is approaching. This system can charge a ferry with a distance of up to 50 cm between transmitting and receiving pads. One standard wireless charger in such system can deliver 2.5 MW with an efficiency of around $95-97\%$. The system is expect to work for at least 15 years.

Figure 1.5: The electrical ferry "MF Folgefonn" with stationary IPT system in Norway

Two IPT charging prototypes, as shown in Figure 1.6, have been designed and built at Chalmers University of Technology in previous works [17–20]. Figure 1.6a is a 500kW stationary IPT prototype for the application of fast charging of ferry. In this prototype, three single-phase charging modules are connected in parallel to gain a higher DC terminal output power. Figure 1.6b is a smaller 50kW stationary IPT system for EVs application [11]. Several tests have been conducted in previous studies to evaluate the performance of these prototypes, including the design of coil, the

stray field, and the thermal properties of the system [19].

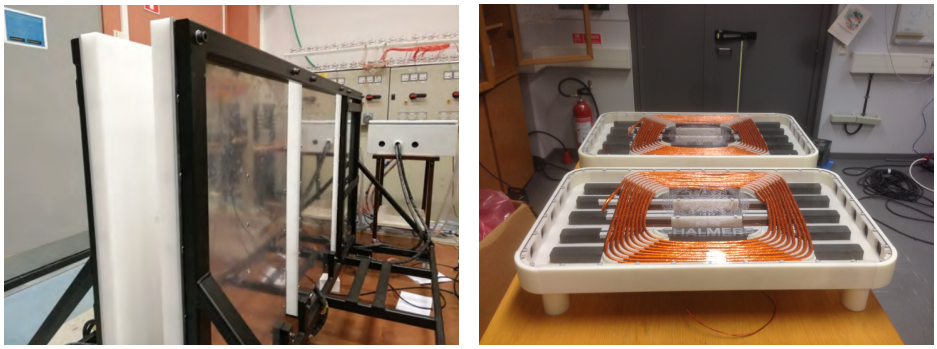

(a) 500kW ferry charging system

(b) 50kW vehicle charging system [11]

Figure 1.6: The stationary IPT prototypes at Chalmers

In this thesis, the focus is on the development of stationary IPT systems, as the principles and research methodology behind stationary IPT and dynamic IPT are identical, and stationary IPT systems can be more easily implemented in practice.

1.3 Review of Previous Work on Stationary IPT

1.3.1 Research on Charging Pad Design

As depicted in Figure 1.7, the key components of an inductive charging pad include a coil, a magnetic core, and a magnetic shield. The coil establishes a conductive path for the high-frequency current, generating a high-frequency magnetic field in the surrounding space. The magnetic core serves to concentrate the magnetic flux, while the magnetic shield is employed to diminish the leakage flux around the pad. The key components and their descriptions are listed as follows:

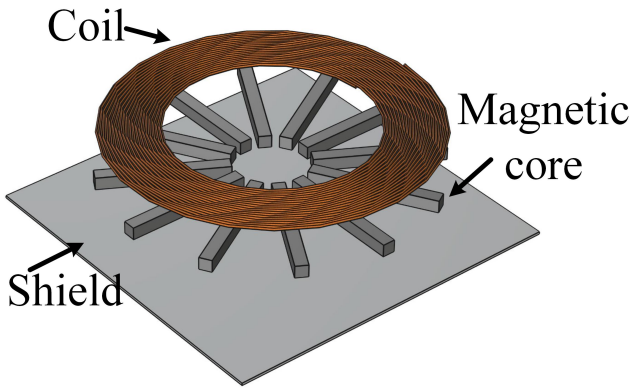

Figure 1.7: The typical components of a magnetic pad used in stationary IPT

- **Coil**
  The coil is constructed using litz wire, which comprises multiple thin and

insulated copper strands. Each copper strand has a small cross-section to minimize the skin effect. These strands are twisted together to decrease the overall equivalent resistance. To mitigate the proximity effect, the thickness of insulation layer of each strand is chosen [9]. The unique structure of the litz wire contributes to a very low total AC resistance.

- **Magnetic core**
  The alternating current generates a magnetic flux. The flux travels in the loop formed by the transmitting and receiving coils. The magnetic core serves a dual purpose: it guides the flux from the transmitting coil towards the receiving coil and diminishes the overall magnetic reluctance in the loop, thereby amplifying the flux density. As a result, the number of turns in the coil can be reduced, leading to reduced size and copper losses. To mitigate core losses, the magnetic core is typically crafted from soft ferrite with high permeability, low electrical conductivity, and low coercivity.
- **Magnetic shield**
  The charging pad must adhere to limitation regarding time-varying electromagnetic fields. To safeguard the electric vehicle's chassis against electromagnetic interference (EMI) emanating from the pad, a magnetic shield is commonly employed. Typically composed of copper or aluminum, this shield serves as a protective barrier. Given the high-frequency electromagnetic fields generated by the coils, eddy currents can be induced in the conductive plate of the shield. These currents, in turn, generate a magnetic field that opposes the original fields, leading to partial cancellation of the original field. This phenomenon reshapes the magnetic flux path, thereby minimizing leakage flux. Moreover, the shield offers robust mechanical protection for the pad [21, 22].

There are various structures for magnetic pad designs. A well-designed pad should take into account factors such as coupling condition when the coils are fully aligned, misalignment tolerance, charging range, cost, and more [21]. Various pad designs can be used according to the application to optimize the performance of coupler. Circular pad, rectangular pad, and double-D (DD) pad are among the most commonly used designs, as illustrated in Figure 1.8 [21]. In addition to these typical designs, numerous novel designs have been proposed in the literature.

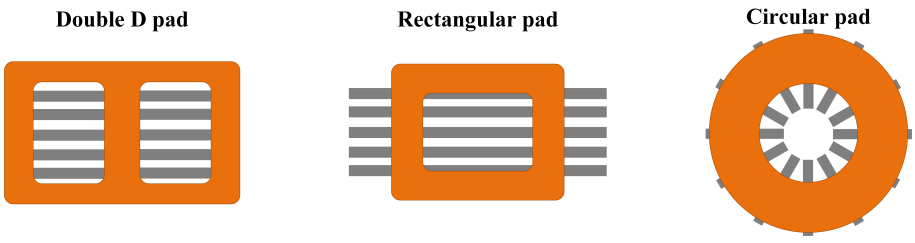

Figure 1.8: Typical pad designs in literature

In [23], a 6.78MHz, 200W IPT system is built with an optimized coupler design. An analytical model-based optimization method is applied to obtain a magnetic coupler with high misalignment tolerance and efficiency. Additionally, Zhi Bie et al. [24]

propose an asymmetric magnetic coupler design utilizing the horizontal magnetic field of the transmitting coil for unmanned aerial vehicle applications. This structure shows advantages of free-rotation and offset tolerance. The stray field around a 3.3kW IPT charger is analyzed in [25], and the result shows that the requirement on leakage flux density can be fulfilled easily for a low-power IPT charger. However, it's worth noting that asymmetrically designed coils may become space and material-consuming in high-power IPT charging scenarios.

1.3.2 Research on Resonant Network

Even when the coils are perfectly coupled, the equivalent input reactance of the system is very large, leading to low input current and high reactive power consumption. Resonant networks are applied to achieve impedance matching and reduce reactive power consumption [26]. The resonant network can be categorized as series, parallel, or LCC based on the different arrangements of capacitors and inductors. Tunable resonant networks are also found in many literatures [27–30]. The selection of the resonant network depends on the desired performance. For instance, the resonant frequency of a series-series (SS) topology (series resonant tank on the transmitting end and series resonant tank on the receiving end) is load and coupling independent, and the efficiency of SS topology is high. However, there is a risk of over-current in SS topology when the system has a low coupling factor.

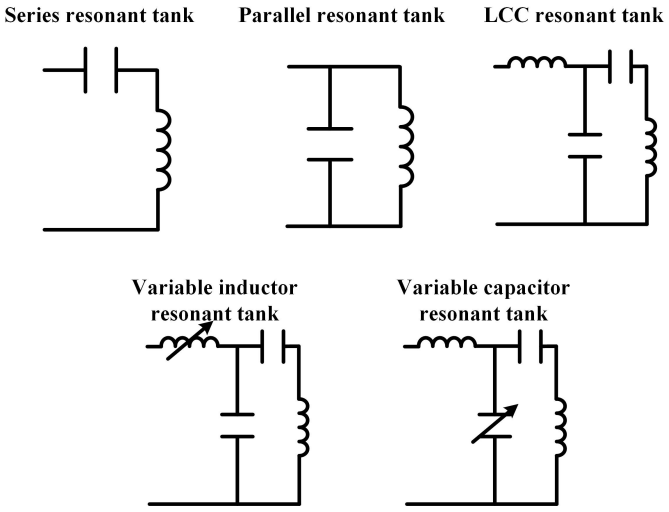

Figure 1.9: Typical resonant networks in literature

The performance of different resonant networks has been studied in previous literatures. In [31], the performance of a topology with series-shunt mixed-resonant coupling is evaluated. The result shows that the mixed-resonant coupling topology performed better in the transfer distance and efficiency. Cody Liu, et al. proposed an active impedance resonant network in [27]. The simulation results of a 7kW system show that by applying the active impedance resonant network, the system achieves constant output power under misalignment variation and load variation.

In [26], the authors provide a comprehensive review to the performance of different resonant network and the primary frequency control scheme.

1.3.3 Research on Control Strategy

A charging control strategy, aiming for battery protection and longer life expectancy, is crucial in EVs charging applications. The IPT system is required to deliver specific power in various working conditions. Many control methods based on different IPT typologies have been studied in previous literature, and they can be categorized into two aspects:

- **Dual-Side Control**
  In this approach, both the transmitting and receiving ends are actively involved in the control process, and they may communicate with each other.
- **One-Side Control**
  In this approach, only one side, either the transmitting or receiving end, is actively involved in the control process.

In a dual-side control system, the inverter and rectifier are controlled separately by two digital signal processors (DSP). Chao Cui et al. investigate the ZVS operating range of a dual-side controlled IPT system [32]. The results show that soft switching can be achieved by adjusting the bilateral load angle. A back-to-back connected prototype is established in [33] with synchronous rectification on the receiver side. This configuration achieves a transmission power of 45.9kW with a system efficiency of 96.6%. However, the efficiency and output power of the system are highly impacted by the coupling condition.

In one-side control methods, the charging process is regulated either on the transmitting end or receiving end. Typically, power control involves adjusting the input voltage, system frequency, and input power factor. Compared with the dual side control system, a one-side control system is simpler and more cost effective. However, variations in load and misalignment can cause a drift in power. The controller relies on information from the receiving end to calculate the coupling and load. Wireless communication can be used to transmit variable values. In [34], the author proposes an IPT system based on magnetic in-band communication. Here, information is sent to the transmitting side via the low-frequency voltage component. This approach offers the advantage of leveraging the main coil for communication purposes, obviating the need for an additional communication coil. Alternatively, in [35], an Infrared (IR) communication system is implemented to fulfill the low communication delay criteria of dynamic charging setups. IR technology boasts minimal power consumption, thereby exerting negligible influence on the efficiency of high-power IPT systems. Nonetheless, IR signals are susceptible to obstruction by solid objects, leading to diminished reliability and constrained transmission distances. These inherent limitations pose challenges for the widespread application of IR communication in certain scenario. Additionally, systems with communication requirements necessitate extra communication circuits, increasing the overall cost

and potentially reducing reliability.

Compared with dual-side control, one-side control is less costly and more robust. But the IPT system with one-side control shall be designed against the variation of misalignment and load. According to [36], a multiple coils design can be used on the transmitting side to build a high misalignment tolerance IPT system. In [13], the authors found that the coupling of a two-transmitter system can be calculated by using only the transmitting side parameters.

To achieve output power independence of coupling variations, an IPT system based on a PT-symmetric circuit is proposed in [37]. In this approach, the power source is treated as a negative resistor, enabling constant output power and efficiency in strong coupling regions, irrespective of the coupling coefficient variation. Moreover, this control scheme relies solely on the transmitting current, eliminating the need for wireless communication. In [38], the stability and steady-state working frequency of a PT-symmetric circuit are discussed. The control strategy fulfilling the negative resistance source is further explored in [39], where a synchronization circuit is employed to control the phase angle between the inverter output voltage and current. The proposed control scheme requires high-speed controllers and amplifiers to mitigate the influence of inherent propagation delay, which exists in the control circuit. Consequently, this increases the complexity and cost of the control system. Besides, the propagation delay causes a hard-switching problem, which reduces the efficiency of the system. However, neither discussion on the effect of propagation delay nor the compensation method has been analyzed.

1.3.4 Purpose of This Thesis

Based on the literature review, it can be concluded that numerous studies have focused on the control strategy, resonant tank design, and coil design of IPT systems. However, a notable gap remains in the field concerning the development of an IPT system capable of achieving high-power transmission with both efficiency and robustness. The performance of existing systems is significantly impacted by variations in load and coupling conditions, presenting challenges particularly in scenarios such as ferry and dynamic charging applications. Thus, further study on the operation and control of the inductive charging system is needed to make it a competitive solution for charging. The IPT system shall deliver power to the battery in a robust, simple, controllable, and efficient way. An IPT system combining:

- High misalignment tolerance, such that the coupling variation does not affect the output power
- Provide controllable output power regardless the variation of the load
- No need of communication to reduce the complexity, and increase the reliability of the system
- Soft switching control scheme to achieve higher efficiency

is missing in the literature. Consequently, the objective of this thesis is to investigate

the modelling of the SS-resonant IPT system and propose a corresponding control scheme that satisfies the aforementioned requirements.

1.4 Thesis Outline

The remainder of this thesis is organized as follows:

In **Chapter 2**, first, the modelling of inductive coupler is introduced. Subsequently, a schematic of the SS-resonant tank IPT system is depicted. Additionally, the power electronic inverter and rectifier are linearized based on the current and voltage waveforms of the terminals, leading to the development of an equivalent circuit for the IPT system. The performance of the system working in fixd-frequency mode is discussed. Simulation and experimental investigations on the inductive coupler and IPT system operating in fixed-frequency mode are conducted, and the results are compared with theoretical calculations.

Chapter 3 introduces the working principle of coupling independent IPT system. The control scheme, which can achieve coupling independent operation, is proposed. Some practical issues, which may affects the implementation of the control scheme, are discussed. Experimental validation of the proposed control strategy is also provided and the result is compared with simulation.

In order to further build a load-independent IPT system, an output power control strategy is proposed in **Chapter 4**. Various methods for controlling the output power are explored with emphasis placed on the utilization of the DC link input voltage for power regulation. Consequently, the rectifier connecting the power grid and the IPT system can be used for power control. This chapter comprehensively addresses the topology, modelling, and control of the rectifier, and simulation studies are conducted to validate the proposed approach.

1.5 List of Publications

This thesis is based on the work contained in the following papers.

Paper 1 L. Lai, J. Huang, J. Tang, Z. Ouyang, Y. Liu, and M. A.E. Andersen - *Digital Control Implementation for Coupling Independent IPT Systems without Communication.* Published in *The International Power Electrnoic and Motion Control Conference (IPEMC 2024-ECCE Asia)*, May, 2024

2

Working Principle of IPT System

2.1 Theorem of IPT system

2.1.1 Modelling of Magnetic Coupler

In an IPT system, power is delivered using magnetic coupler. A demonstration to the working principle of magnetic coupler is shown in Figure 2.1. The induced voltage on the coil terminals u_1 and u_2 can be described as follows (Faraday's law of induction):

$$\begin{cases} u_1 = N_1 \dfrac{d\Phi_1}{dt} = N_1 \dfrac{d(\Phi_{11} + \Phi_{12})}{dt} \\ u_2 = N_2 \dfrac{d\Phi_2}{dt} = N_2 \dfrac{d(\Phi_{21} + \Phi_{22})}{dt} \end{cases} \tag{2.1}$$

where Φ_1 and Φ_2 are the flux passing through the transmitting coil and receiving coil, respectively. Φ_{ij} is the flux in coil i generated by coil j. Then the following equations are derived from the equivalent magnetic circuit:

$$\begin{cases} u_1 = \dfrac{N_1}{R_{11}} \dfrac{dF_1}{dt} + \dfrac{N_1}{R_{12m}} \dfrac{dF_2}{dt} = \dfrac{N_1^2}{R_{11}} \dfrac{di_1}{dt} + \dfrac{N_1 N_2}{R_{12m}} \dfrac{di_2}{dt} = L_1 \dfrac{di_1}{dt} + M_{12} \dfrac{di_2}{dt} \\ u_2 = \dfrac{N_2}{R_{21m}} \dfrac{dF_1}{dt} + \dfrac{N_2}{R_{22}} \dfrac{dF_2}{dt} = \dfrac{N_1 N_2}{R_{21m}} \dfrac{di_1}{dt} + \dfrac{N_2^2}{R_{22}} \dfrac{di_2}{dt} = M_{21} \dfrac{di_1}{dt} + L_2 \dfrac{di_2}{dt} \end{cases} \tag{2.2}$$

where N_1 and N_2 are the number of turns of the coils. F_1 and F_2 are the magnetic motive force of transmitting coil and receiving coil, respectively. $L_1 = N_1^2/R_{11}$ and $L_2 = N_2^2/R_{22}$ are the self inductance of the coils. If we further assume that the flux path is symmetric (i.e. $\Phi_{21} = \Phi_{12}$), then $M = M_{12} = M_{21} = N_1 N_2 / R_{mm}$ is the mutual inductance, $R_{mm} = R_{12m} = R_{21m}$ is the mutual magnetic reluctance. The magnetic reluctance terms are highly dependent on the geometry of coupler and can be described as follows:

$$R_{mm} = \frac{l_{core}}{\mu_r \mu_0 A_{core}} + \frac{l_{air}}{\mu_0 A_{air}} \tag{2.3}$$

where l_{core} is the effective length of ferrit core, A_{core} is the effective area of ferrit core, l_{gap} is the effective length of air gap, A_{gap} is the effective area of air gap, μ_r is the relative permeability of the ferrit core, and μ_0 is the magnetic permeability of free space. It can be concluded that the mutual inductance M and self inductance L_1, L_2 depend on the effective length and cross-section area of the flux paths. When the

misalignment changes, the effective length and cross-section area of the flux paths vary differently. The coupling factor of the coupler is defined as

$$k \triangleq \frac{M}{\sqrt{L_1 L_2}} = \frac{\sqrt{R_{11} R_{22}}}{R_{mm}} \tag{2.4}$$

which is the ratio of mutual inductance and self inductance. When the misalignment between pad increases, the leakage flux increase, the coupling between pads is weaker, and the coupling factor reduces.

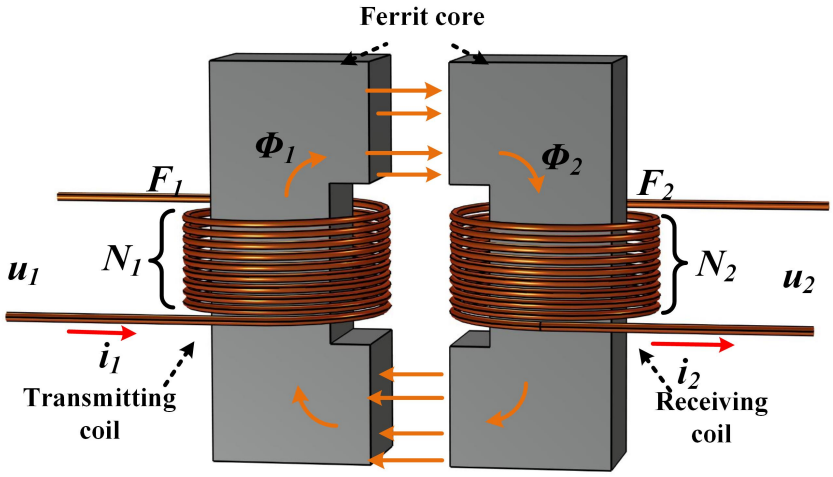

Figure 2.1: An example of magnetic coupler

2.1.2 Modelling of Power Source

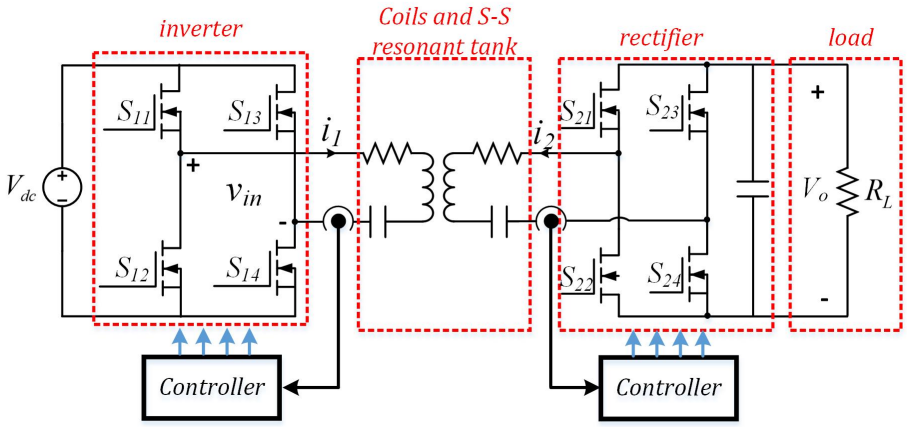

Figure 2.2: System configuration of series-series resonant (SS) IPT system

A schematic to the IPT system can be obtained in Figure 2.2. The system comprises a DC voltage source, a full-bridge inverter, a controller, coupled transmitting and

receiving coils, series-series(SS) resonant tanks, a rectifier, and a load. The inverter transforms DC voltage V_{dc} to pulsating voltage v_{in}. i_1 and i_2 are currents in the transmitting and receiving coils, respectively. V_o is the output voltage and R_L is the load.

To investigate the performance of the system, an linear equivalent circuit model can be built. This involves replacing the inverter and rectifier with the equivalent source and load, respectively. The switching scheme of the inverter is depicted in Figure 2.3. By applying Fourier analysis on v_{in}, the fundamental component (with switching angular frequency $\omega_{sw} = 2\pi f_{sw}$, f_{sw} is the switching frequency of inverter) $v_{in.1}$ is obtained:

$$\begin{aligned} v_{in.1} &= 2f_{sw}\int_0^{1/f_{sw}} v_{in}cos(\omega_{sw}t)dt \\ \Rightarrow v_{in.1} &= \sqrt{2}V_{in}sin(\omega_{sw}t) \\ V_{in} &= 2\sqrt{2}V_{dc}sin(D_1\pi)/\pi \end{aligned} \tag{2.5}$$

where D_1 is the duty ratio, which indicates the ratio of the positive voltage time to the switching period (see Figure 2.3), V_{in} is the root mean square (RMS) value of the fundamental component. Since the fundamental component voltage component plays a major role in power transmission, the fundamental harmonic approximation is used and the effect of harmonic with other orders is ignored. Thus, in the equivalent circuit, the inverter output terminal can be regarded as a sinusoidal voltage source with angular frequency ω_{sw}.

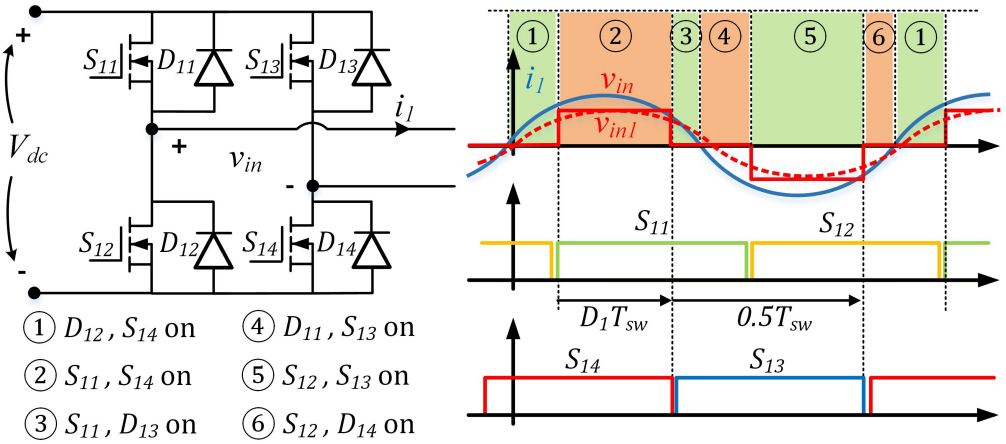

Figure 2.3: Inverter voltage and drive signals, $v_{in.1}$ is the fundamental component of v_{in} with switching angular frequency ω_{sw}

2.1.3 Modelling of Load

On the load side, the control scheme of rectifier is shown in Figure 2.4, and the voltage and current waveform of the rectifier are illustrated in Figure 2.5.

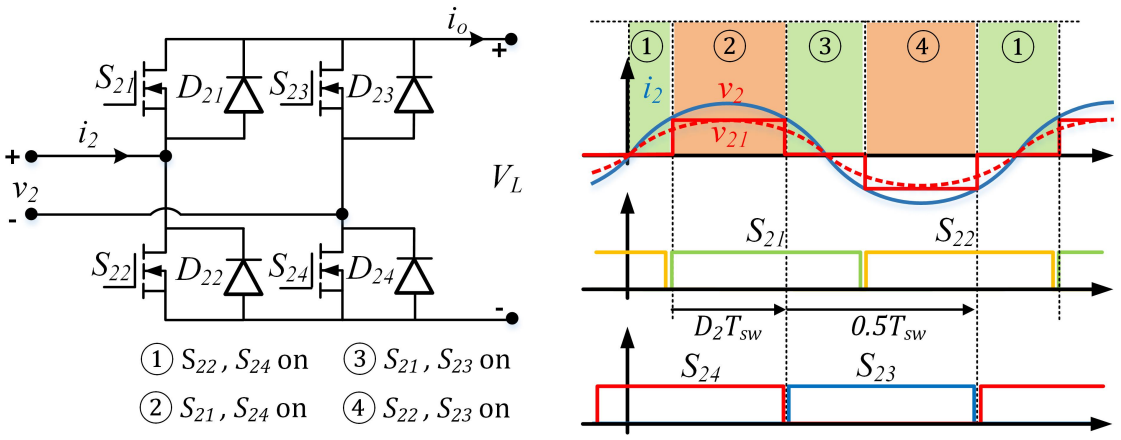

Figure 2.4: Rectifier voltage and drive signal, $v_{2.1}$ is the fundamental component of v_2 with angular frequency ω_{sw}

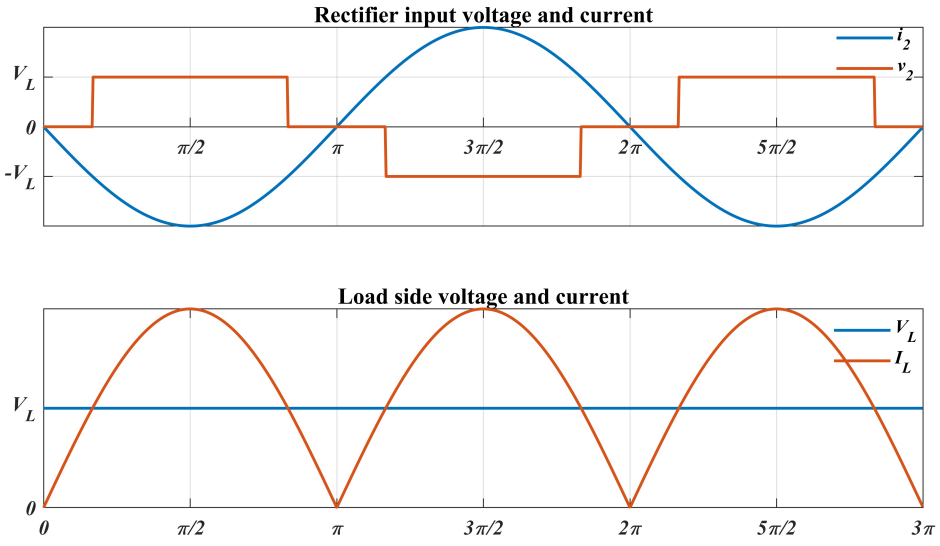

Figure 2.5: Rectifier input and output waveform

In Figure 2.5, v_2 is the rectifier input voltage, i_2 is the receiving coil current, v_L and i_o are the load voltage and rectifier output current, respectively. According to Fourier analysis, the fundamental component of rectifier input voltage can be obtained as follows:

$$\begin{cases} v_{2.1}(t) = \dfrac{4}{\pi} V_L sin(D_2\pi) sin(\omega t + \phi_{v2}) \\ V_2 = \dfrac{2\sqrt{2}}{\pi} V_L sin(D_2\pi) \end{cases} \tag{2.6}$$

where V_2 is the RMS value of $v_{2.1}$. Taking $v_{in.1}$ as the reference, ϕ_{v2} is the phase difference between $v_{2.1}$ and $v_{in.1}$. In steady state, the load is treated as a voltage stiff component. The energy consumption and voltage variation of capacitor are zero. Thus, assuming that the rectifier is lossless, by energy conservation and combining (2.6), the following equations can be obtained for the equivalent load:

$$\begin{aligned} & P_2 = V_2 I_2 = V_L I_o = P_L \\ \Rightarrow & I_2 = \frac{\sqrt{2}\pi I_o}{4\sin(D_2\pi)} \\ \Rightarrow & R_{Leq}(D_2) = \frac{V_2}{I_2} = \frac{8}{\pi^2}\sin(D_2\pi)^2 R_L \end{aligned} \tag{2.7}$$

It can be found that the equivalent load becomes smaller when D_2 decreases ($D_2 \in [0, 0.5]$). When the voltage duty cycle $D_2 = 0$, the rectifier input terminal is short circuited.

After modelling the source and the load, the equivalent circuit of IPT system in frequency domain can be obtained as shown in Figure 2.6.

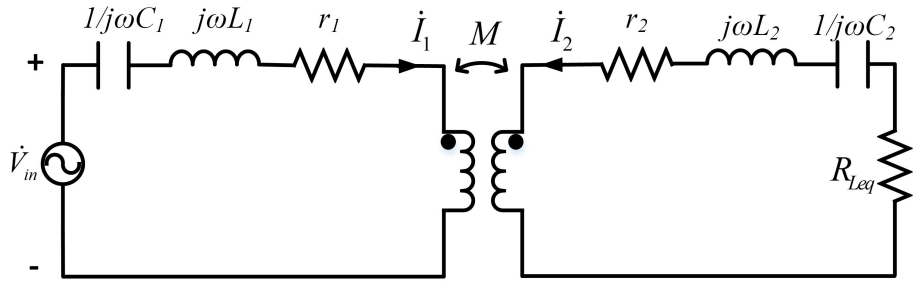

Figure 2.6: The equivalent circuit of SS resonant tank IPT system based on the fundamental component approximation analysis

2.1.4 Fixed-frequency Working Model

According to the equivalent circuit, the following equations can be derived according to Kirchhoff Voltage Laws (KVL):

$$\begin{cases} \dot{V}_{in} = j(\omega L_1 - \dfrac{1}{\omega C_1})\dot{I}_1 + j\omega M\dot{I}_2 + r_1\dot{I}_1 \\ 0 = j(\omega L_2 - \dfrac{1}{\omega C_2})\dot{I}_2 + j\omega M\dot{I}_1 + (r_2 + R_{Leq})\dot{I}_2 \end{cases} \tag{2.8}$$

where L_1 and L_2 are the self-inductance of the transmitting and receiving coils, respectively. C_1 and C_2 are resonant capacitances. $i_{1.1}$ and $i_{2.1}$ are the fundamental component of currents. r_1 and r_2 are the equivalent series resistances. $M = k\sqrt{L_1 L_2}$ is the mutual inductance and k is the coupling factor.

The matched resonant frequency $\omega_0 = 1/\sqrt{L_1 C_1} = 1/\sqrt{L_2 C_2}$ is an option as the working frequency of the system. In this case, the transmitting pad and receiving pad are resonant separately. Consequently, the following relationship holds:

$$\begin{aligned} \dot{I}_2 &= \frac{-j\omega_0 M\dot{I}_1}{R_{Leq} + r_2} \\ \dot{V}_{in} &= (\frac{(\omega_0 M)^2}{R_{Leq} + r_2} + r_1)\dot{I}_1 \\ \Rightarrow P_{in} &= \mathbf{Re}\{\dot{V}_{in}\dot{I}_1^*\} = \frac{V_{in}^2(R_{Leq} + r_2)}{(\omega_0 M)^2 + r_1(R_{Leq} + r_2)} \\ P_{out} &= \mathbf{Re}\{\dot{V}_2\dot{I}_2^*\} = \frac{(\omega_0 M)^2 R_{Leq} V_{in}^2}{[(\omega_0 M)^2 + r_1(R_{Leq} + r_2)]^2} \end{aligned} \tag{2.9}$$

and the efficiency can be calculated as

$$\eta = \frac{P_{out}}{P_{in}} = \frac{(\omega_0 M)^2 R_{Leq}}{(R_{Leq} + r_2)[(\omega_0 M)^2 + r_1(R_{Leq} + r_2)]} \tag{2.10}$$

Equation (2.9) and (2.10) show that the output power and efficiency of the system are susceptible to variations in the coupling condition. Figure 2.7 illustrates the changes in output power and efficiency with respect to the coupling factor. The key parameters utilized in the calculations are enumerated in Table 2.2(with rectifier duty cycle $D_2 = 0.5$). From the figure, it is evident that there is a risk of overpowering in a no-load condition. The system has a high efficiency but low output power in high coupling condition. The efficiency decreases when the coupling factor decreases.

2.2 Experiment and Simulation of IPT System Working in Fixed-frequency Condition

In this section, the IPT system developed at Chalmers University is introduced. The objective is to gather essential parameters necessary for conducting circuit simulations. Initially, the self-inductance and coupling factor of the charging pads are

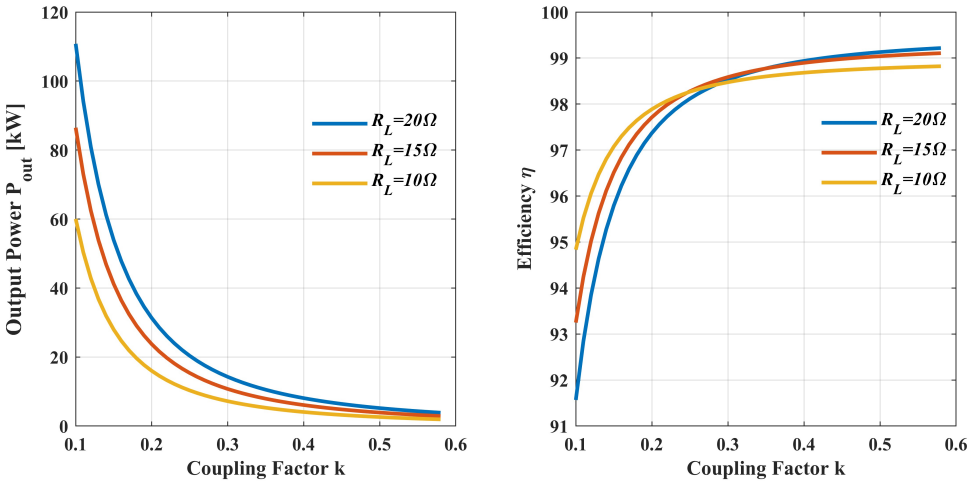

Figure 2.7: The change of output power and efficiency with coupling($V_{in} = 400$V, $R_L = 10\Omega$, $\omega = \omega_0$)

measured. Subsequently, a simulation model in Ansys Maxwell is studied to investigate how misalignment affects the pad parameters.

2.2.1 Simulation and Experiment on Magnetic Coupler

2.2.1.1 Introduction to the setup

A Finite Element Method (FEM) simulation model is developed in Ansys Maxwell to investigate the variation of coupling with changes in misalignment, as depicted in Figure 2.8. This simulation model is based on the work conducted by Daniel in [11]. Given the low electrical conductivity of the ferrite bars and the thinness of the copper shield, the induced eddy currents in these materials can be neglected. Consequently, the model is constructed using the magnetostatic solver in Maxwell, where the magnetic field is generated by DC currents in the coils. The plastic cover is neglected in this simulation, as it has no influence on the magnetic field. The governing equations are the Gauss's law and Ampere's law for magnetic field, which can be described as follows:

$$\begin{cases} \nabla \times \vec{H} = \vec{J} & \text{Gauss's Law in static magnetic field} \\ \nabla \cdot \vec{B} = 0 & \text{Ampere's Law in static magnetic field} \end{cases} \tag{2.11}$$

where $\vec{B}$ is the magnetic flux density, $\vec{H}$ is the magnetic intensity, $\vec{J}$ is the current density. For a system without permanent magnet, the following relationship holds in the material

$$\vec{B} = \mu_0 \mu_r \vec{H} \tag{2.12}$$

where $\mu_0 = 4 \cdot \pi \cdot 10^{-7}$H/m is the permeability of vacuum, μ_r is the relative permeability.

In this simulation, the misalignment between pads is changed and the result is compared with measurement result. The dimensions of the inductive pads are listed in

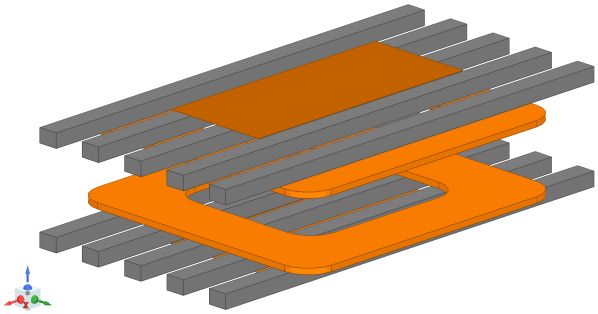

Figure 2.8: FEM model of charging pads

Table 2.1.

Description	Name	Value	Description	Name	Value
Coil length	$coil_l$	430mm	Coil width	$coil_w$	400 mm
Coil thickness	$coil_{th}$	8.34mm	Coil inner length	$coil_{il}$	259mm
Coil inner width	$coil_{iw}$	238mm	Coil fillet	$coil_r$	4mm
Transmitting coil turns	N_1	9.5	Receiving coil turns	N_2	9.5
Ferrite bar length	Fe_l	630mm	Ferrite bar width	Fe_w	28mm
Ferrite bar height	Fe_h	20mm	Bar distance	d_{Fe}	44.5mm
Shield length	l_{Shield}	350mm	Shield width	w_{Shield}	150mm
Ferrite permeability	$\mu_r\mu_0$	$1200\mu_0$	Ferrite permittivity	$\epsilon_r\epsilon_0$	ϵ_0

Table 2.1: The parameters used in the FEM model

To verify the simulation result, an experiment is performed as shown in Figure 2.9. An impedance meter is used to measure the parameters that are necessary to calculate the coupling factor. The connections are drawn in Figure 2.10. The receiving side is short circuited and the short circuit inductance L_k is measured from the primary side. Then, the mutual inductance and coupling factor can be calculated as follows:

$$\begin{aligned} \dot{V}_{in} &= j\omega L_1\dot{I}_1 + j\omega M\dot{I}_2 \\ 0 &= j\omega L_2\dot{I}_2 + j\omega M\dot{I}_1 \\ \Rightarrow \dot{V}_{in} &= j\omega M\dot{I}_1 - j\omega\frac{M^2}{L_2}\dot{I}_1 \\ \Rightarrow j\omega L_k &= j\omega L_1 - j\omega\frac{M^2}{L_2} \\ \Rightarrow M &= \sqrt{L_1L_2 - L_2L_k} = k\sqrt{L_1L_2} \end{aligned} \tag{2.13}$$

Therefore, the experiment process can be described as follows:

- Measure the short circuit inductance L_k;

- Disconnect the receiving end, measure L_1;
- Disconnect the transmitting end, measure L_2;
- Change the misalignment of pads, redo the measurement.

From equation (2.13), we know that the coupling can be obtained through the value of self inductance L_1, L_2, and L_k.

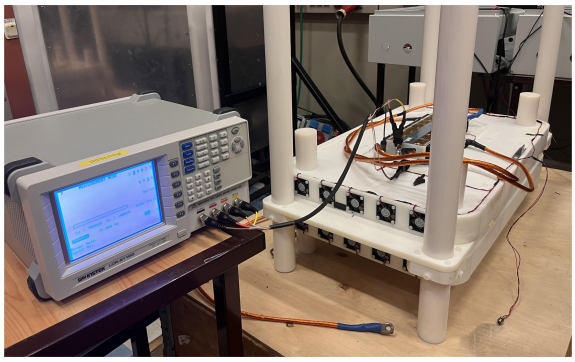

Figure 2.9: The measurement of self inductance and mutual inductance

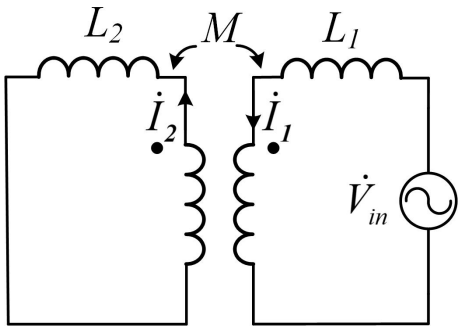

Figure 2.10: Coupling measurement circuit

2.2.1.2 Result and analysis

The flux distribution between the pads is illustrated in Figure 2.11. In Figure 2.11a, it is evident that, at a current of 50A and a frequency of 85.5kHz, the flux predominantly concentrates in the middle of the ferrite bar where overlaps with the coil. Figure 2.11b provides a cross-sectional view of the flux distribution. The leakage flux can be observed to circulate around the ferrite core and air, contributing to a lower coupling factor between the pads.

The measurement and simulation result of coupling factor are shown and compared in Figure 2.12a. It can be observed that the simulation result is lower than the measurement. This difference may be explained by the fact that the magnetic shield is ignored in the simulation, resulting in lager leakage magnetic flux and lower coupling factor. In general, the simulation result shows good agreement with the measurement. The result also shows that the coupling factor reduces when the

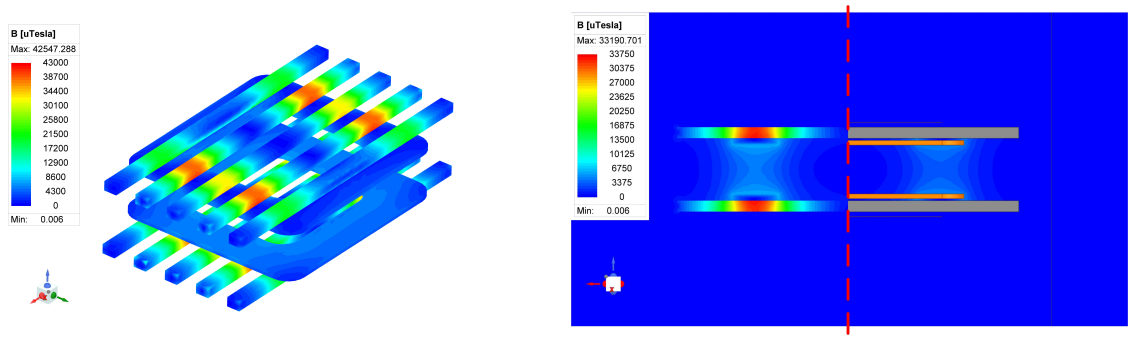

(a) Flux Distribution (3D view) **(b)** Flux distribution (cut view)

Figure 2.11: The FEM simulation result of flux distribution between pads

misalignment increases. This result can be explained by the fact that there is more leakage flux when the misalignment increases, and the flux coupled with the other coil reduces, which results in the reduction of coupling factor. The variation of self

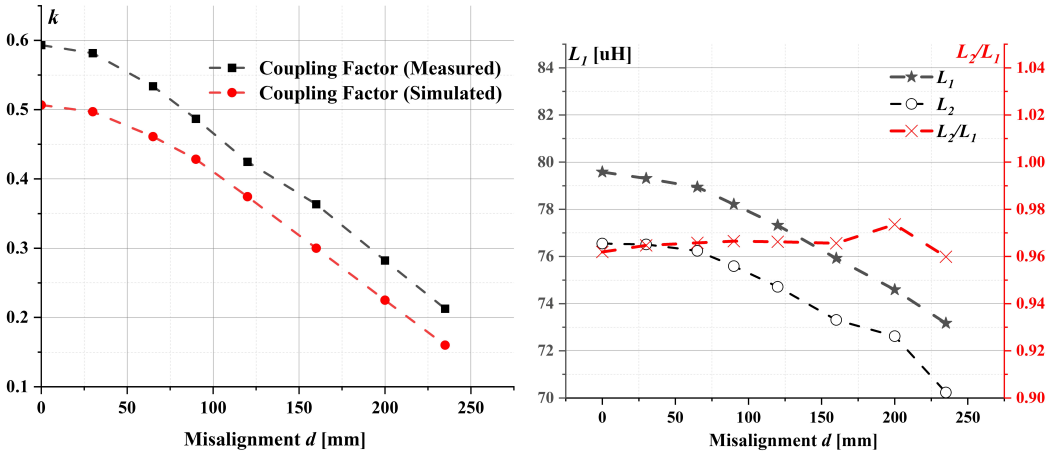

(a) The variation of coupling factor with misalignment **(b)** The variation of self inductance L_1 and L_2 with misalignment

Figure 2.12: Magnetic coupler measurement experiment results

inductance L_1 and L_2 with misalignment are shown in Figure 2.12b. It can be found that the self inductance will reduce when the misalignment increases. Besides, the ratio of self inductance L_1/L_2 is shown in the figure. The ratio is constant regardless of the variation of misalignment. According to the relationship in (2.2), the ratio between L_1 and L_2 can be described as follows:

$$\begin{aligned} L_1 = &\frac{N_1^2}{R_{11m}}, \; L_2 = \frac{N_2^2}{R_{22m}} \\ \Rightarrow &\frac{L_1}{L_2} = \frac{N_1^2 R_{22m}}{N_2^2 R_{11m}} \end{aligned} \tag{2.14}$$

Thus, when the geometry structure is symmetric with $R_{11m} = R_{22m}$, the ratio L_1/L_2 will remain constant when the misalignment changes. From the experiment result,

one can conclude that L_1 and L_2 vary by approximately 10% when the misalignment change from 0 to 250mm. To simplify the analysis, the average value of measurement results is used in the simulations for self inductance.

2.2.2 Simulation and Experiment on Fixed-frequency IPT System

2.2.2.1 Introduction to the setup

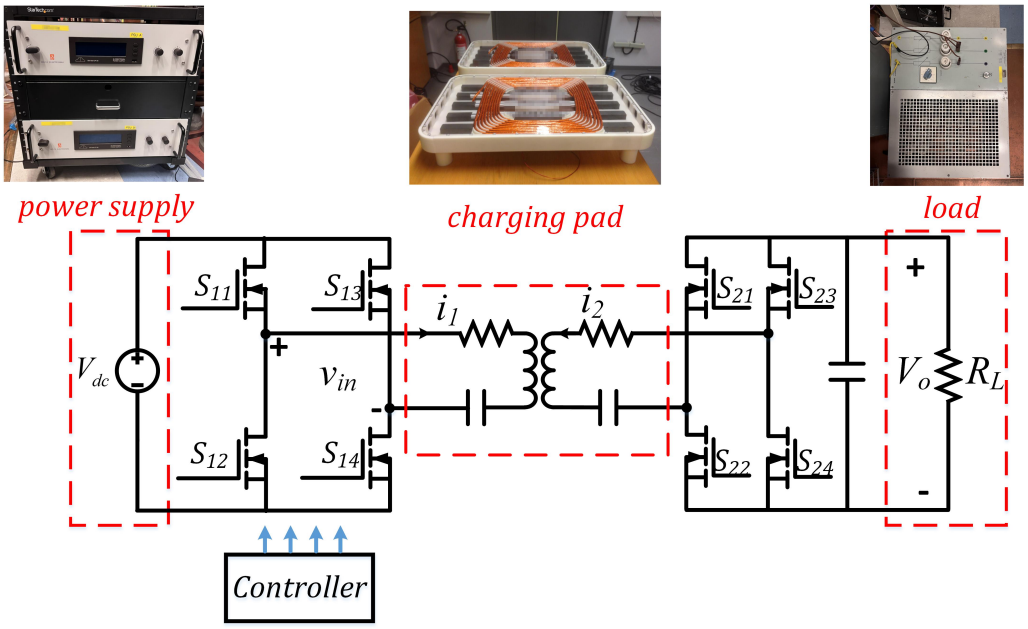

Figure 2.13: Experimental set up

An IPT prototype with fixed switching frequency digital control is built to verify the theoretical analysis. The experimental setup is illustrated in Figure 2.13. A constant voltage source is connected to the input of the full bridge inverter, with the gate voltage provided by the CGD12HBXMP gate driver(see Figure 3.15b). The coils are designed as rectangular pads to fully utilize the available place (see Figure 2.14). A constant resistance load is connected to the full bridge rectifier. To simplify the analysis, the rectifier is passive. Thus, the current will conduct through the body diode of MOSFET and the rectifier duty cycle $D_2 = D_{2\cdot max} = 0.5$ in (2.7). Further analysis regarding dual active bridge control strategy is shown in **Chapter3**.

In the experiment, the working frequency is selected to be $f_{sw} = 85.5$kHz. The active bridge control of rectifier will be introduced in next chapter. The parameters and the dimension of coil are detailed in Table 2.2.

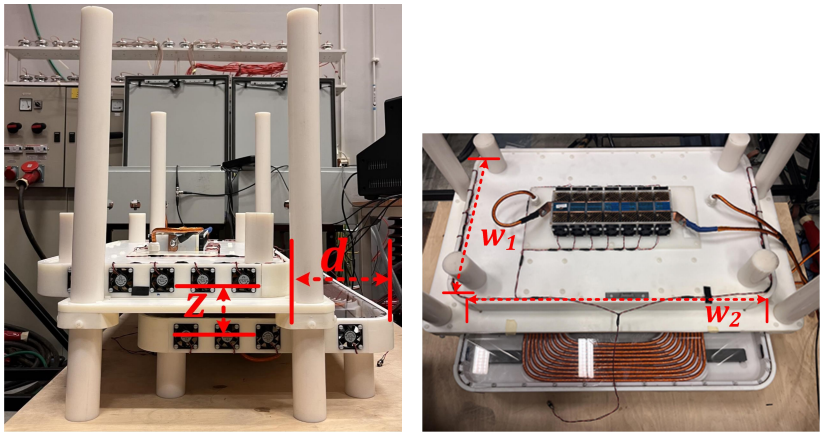

(a) Front view (b) Top view

Figure 2.14: Coils for the experimental system

Description	Symbol	Value
Transmitting end self inductance	L_1	77.21μH
Receiving end self inductance	L_2	74.86μH
Transmitting end capacitance	C_1	45.80nF
Receiving end capacitance	C_2	45.204nF
Transmitting end ESR	r_1	147.10mΩ
Receiving end ESR	r_2	133.62mΩ
Diode forward voltage drop	V_f	1.6V
MOSFET turn on resistance	R_{on}	4.67mΩ
Coupling factor	k	$[0.2, 0.6]$
Pad width	w_1	450mm
Pad length	w_2	740mm
Horizontal misalignment	d	$[0, 250]$mm
Vertical distance	z	150mm

Table 2.2: The parameters of the experiment setup and simulation

2.2.2.2 Result and analysis

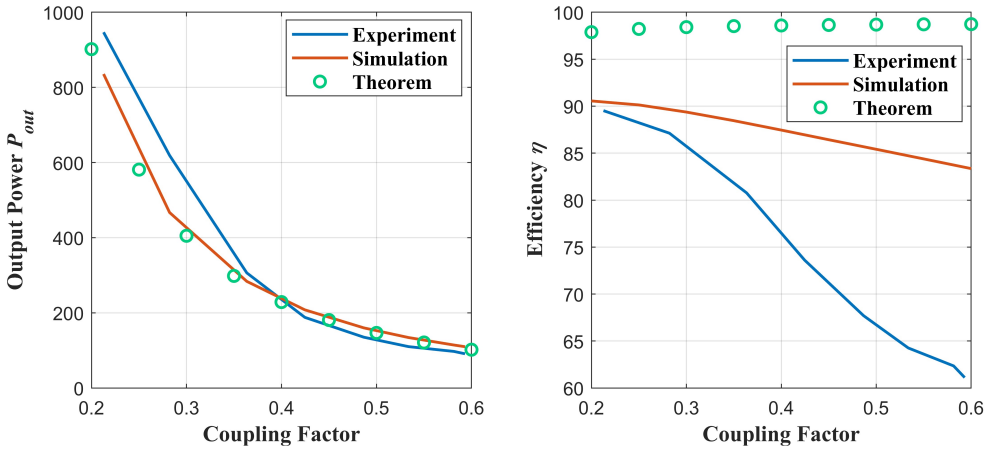

Figure 2.15: System output power and DC-DC efficiency under fixed-frequency working scheme ($R_L = 9\Omega$, $V_{dc} = 100$V, and $D_1 = D_2 = 0.5$)

The experiment and simulation result on the output power and efficiency of the system for different misalignment conditions are compared in Figure 2.15. To compare the results obtained from simulation and experiment, the misalignment d in experiment is mapped into coupling factor k based on the result obtained from Figure 2.12a.

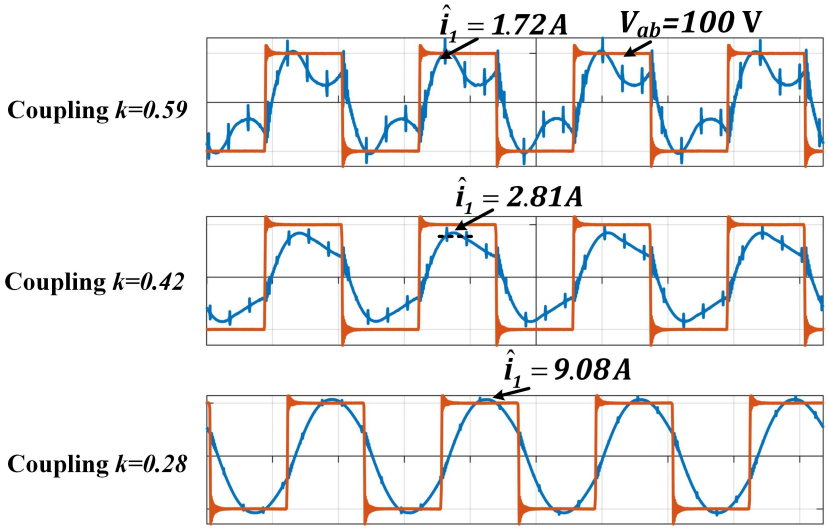

Figure 2.16: Transmitting coil terminal voltage (v_1) and current (i_1) waveform under fixed-frequency working scheme ($R_L = 9\Omega$, $V_{dc} = 100$V, and $D_1 = D_2 = 0.5$)

It can be observed that the system has very low output power in high coupling condition. The simulation and experiment power show a good agreement with the

theoretical calculation result. However, in high coupling condition, the system efficiency is much lower than the theoretical calculation. As Equation (2.10) considers only the transmitting losses generated by the fundamental component. The waveform of line voltage v_{in} and current i_1 under different misalignment conditions are shown in Figure 2.16. A unity power factor is not achieved in this experiment as the system is not completely symmetric(i.e. $L_1 \neq L_2$, $C_1 \neq C_2$). The resonant point is varying with the change of misalignment, this may be attributed to the variation of self inductance, leading to a drift in resonant frequency. Under a high coupling condition, the transmitting current contains a large amount of harmonic, resulting in higher losses and lower efficiency.

3

Coupling Independent IPT System

3.1 Theorem of Coupling Independent IPT System

In **Chapter 2**, we highlight that the output power and efficiency of the IPT system are influenced by the coupling condition. This can be attributed to the fixed working frequency, where $\omega = \omega_0 = 1/\sqrt{LC}$ (ω_0 denotes the natural resonance angular frequency of the system), and the mutual inductance is not included in the resonant tank. To further elaborate, assuming that the self inductance of coils are independent of misalignment, the equivalent input impedance can be derived from (2.8), This yields the following expression for the system's input impedance, denoted as $Z_{in} = \dot{V}_1/\dot{I}_1 = R_n + jX_n$:

$$\begin{cases} R_n = r_1 + \dfrac{(\omega M)^2(R_{Leq} + r_2)}{(R_{Leq} + r_2)^2 + (\omega L_2 - \frac{1}{\omega C_2})^2} \\ X_n = \omega L_1 - \dfrac{1}{\omega C_1} - \dfrac{(\omega M)^2(\omega L_2 - \frac{1}{\omega C_2})}{(R_{Leq} + r_2)^2 + (\omega L_2 - \frac{1}{\omega C_2})^2} \end{cases} \tag{3.1}$$

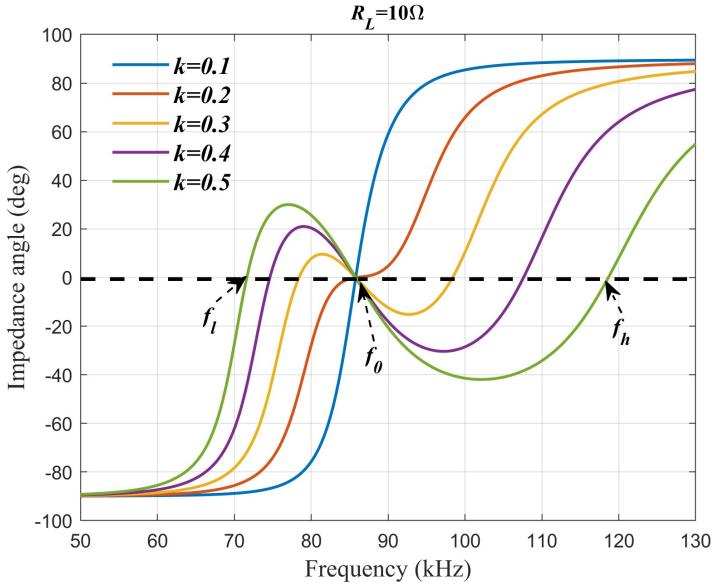

Figure 3.1: Relationship between equivalent impedance angle and frequency

From equation (3.1), it is evident that Z_{in} is related to the coupling condition M, the switching angular frequency ω and system parameters. In a scenario of static charging, where the misalignment between coils remains fixed once the vehicle comes to a stop, the circuit parameters remain constant throughout the charging process. As a result, and Z_{in} depends solely on switching frequency.

An intuitive approach to determining the equivalent impedance is to achieve a unity power factor(i.e. $X_n = 0$), as this minimizes the reactive power. Figure 3.1 illustrates the relationship between the angular switching frequency ω and the input impedance angle $\phi = tan(X_n/R_n)$. The parameters utilized in the calculations are listed in Table 3.1.

It can be observed that in weak coupling condition ($k = 0.1$ and $k = 0.2$), the system has only one working frequency ω_0 that can achieve the unity power factor. However, in strong coupling condition ($k > 0.2$), the working frequency splits into three solutions ω_l, ω_0, and ω_h. This phenomenon is commonly referred to as bifurcation in previous literature [40, 41].

Parameter	Value	Parameter	Value
R_{Leq}	8.1Ω	R_1	70μΩ
R_2	70μΩ	C_1	47.14nF
C_2	47.14nF	L_1	73mH
L_2	73mH	f_{sw}	[50, 130]kHz

Table 3.1: The parameters used in impedance angle calculation

The inverter output voltage is controlled by the driver circuit control scheme. Thus, a unity power factor can be achieved by synchronizing the inverter output voltage $v_{in.1}$ with transmitting current $i_{1.1}$(see Figure 2.6). In this case, the input power source can be regarded as a negative resistance R_n [39,42]. In other words, the input reactance $X_n = 0$. Considering the case that the system has matched resonance frequency (i.e., $\sqrt{L_1C_1} = \sqrt{L_2C_2} = 1/\omega_0$), then the following relationship can be deduced from (3.1):

$$\frac{L_1}{L_2} = \frac{(\omega M)^2}{(R_{Leq} + r_2)^2 + (\omega L_2 - \frac{1}{\omega C_2})^2} \tag{3.2}$$

By solving (3.2), the working frequency ω can be obtained as follows:

$$\begin{cases} \omega = \omega_0 & k \leq k_c \\ \omega = \omega_{l,h,0} & k > k_c \end{cases} \tag{3.3}$$

where

$$\begin{cases} \omega_{l,h} = \sqrt{\dfrac{-(\Gamma_2^2 - 2\omega_0^2) \pm \sqrt{\Delta}}{2(1-k^2)}} \\ \Delta = -4\omega_0^2\Gamma_2^2 + \Gamma_2^4 + 4k^2\omega_0^4 \\ \Gamma_2 = \dfrac{R_{Leq} + r_2}{L_2}, k_c = \dfrac{\Gamma_2}{\omega_0^2}\sqrt{\omega_0^2 - \dfrac{\Gamma_2^2}{4}} \end{cases} \tag{3.4}$$

Therefore, the working conditions can be separated into two regions based on the coupling factor.

When $k > k_c$, the system works in strong coupling region. When the system is operating with working frequency ω_l or ω_h, the output power can be calculated as follows:

$$\begin{aligned} P_{out} &= |\dot{I}_2|^2 R_{Leq} \\ |\dot{I}_2|^2 &= \frac{(\omega M)^2 |\dot{I}_1|^2}{\sqrt{(R_{Leq} + r_2)^2 + (\omega L_2 - \frac{1}{\omega C_2})^2}} \\ \Rightarrow |\dot{I}_2|^2 &= \frac{L_1}{L_2}|\dot{I}_1|^2 \\ \Rightarrow P_{out} &= \frac{L_1}{L_2}|\dot{I}_1|^2 R_{Leq} \\ \Rightarrow P_{out} &= \frac{L_1}{L_2}\frac{V_{in}^2}{R_n^2} R_{Leq} \end{aligned} \tag{3.5}$$

Substitute (3.1) into (3.5), the output power can be obtained as follows:

$$P_{out} = \frac{R_{Leq} V_{in}}{\frac{L_1}{L_2}(R_{Leq} + r_2)^2 + 2r_1(R_{Leq} + r_2) + \frac{L_2}{L_1} r_1^2} \tag{3.6}$$

The efficiency can be calculated as:

$$\begin{aligned} \eta &= \frac{P_{out}}{P_{out} + |\dot{I}_1|^2 r_1 + |\dot{I}_2|^2 r_2} \\ \Rightarrow \eta &= \frac{R_{Leq}}{\frac{L_2}{L_1} r_1 + r_2 + R_{Leq}} \end{aligned} \tag{3.7}$$

This system can be described with a parity-time-symmetric (PT-symmetric) model. The strong coupling region is also known as PT-symmetric region. It has been demonstrated that in the PT-symmetric region, the transfer efficiency and transfer power are independent of the coupling factor (as it is described in (3.5)). The working frequency converges to either ω_h or ω_l when the negative resistance is achieved [38].

In the case when $k \leq k_c$, which is known as broken PT-symmetric region, system has the only working frequency $\omega = \omega_0$. The output power and efficiency can be calculated using (2.9) and (2.10). It indicates that in the broken PT-symmetric region, the output power is subject to the coupling factor.

3.2 Practical Issues in Implementation

In this section, the issues appearing in the implementation of coupling independent IPT control strategy are discussed. It is desirable to reduce losses and electromagnetic noise, increase the lifespan of power electronic component by applying soft switching operation. In this section, the boundary for soft switching operation of inverter and rectifier are proposed. The practical issues related to the synchronization of inverter output voltage $v_{in.1}$ and transmitting current $i_{1.1}$ are discussed. It can be shown that by applying a new gate signal generation strategy to control the power factor angle, soft switching operation of coupling independent IPT system can be achieved.

3.2.1 Compensation of Propagation Delay

The PT-symmetric mode introduced in Section 3.1 provide a unity input power factor and high misalignment tolerance. To achieve PT-symmetric mode with unity input power factor, a phase synchronization method is necessary. Using a current sensor and zero-crossing comparator, the controller can sample the transmitter current and generate a gate signal that synchronizes with the current. However, the propagation delay in components of the control circuit can result in a lagging inverter output voltage, leading to synchronization failure and increasing the switching loss. This delay can significantly impact the performance of a digital control system. Considering a control system with propagation delay Δt_d, the phase difference between inverter output voltage $\dot{V}_{in}$ and transmitter current $\dot{I}_1$ is given by $\alpha = -\Delta t_d \omega$. The equivalent input reactance X_n in Equation (3.1) becomes:

$$X_n = R_n tan(-\Delta t_d \omega) \tag{3.8}$$

By submitting (3.8) into (3.1), the working frequency ω and output power can be obtained as:

$$\begin{cases} \omega = f(\Delta t_d, k) \\ P_{out} = g(\Delta t_d, k) \end{cases} \tag{3.9}$$

This indicates that propagation delay leads to working frequency and output power drift. Therefore, to keep a constant output power independence of coupling factor, a compensation is necessary to achieve PT-symmetric conditions. Considering a system with compensation Δt_c, the equivalent reactance becomes:

$$X_n = R_n tan(-\Delta t \omega) \tag{3.10}$$

where $\Delta t = \Delta t_d - \Delta t_c$.

Based on the phase difference between $\dot{V}_{in}$ and $\dot{I}_1$, there are three types of compensation shown in Figure 3.2. In the fully-compensated case, where $\Delta t_d = \Delta t_c$, the voltage is synchronized with the current, resulting in the highest input power factor. In the under-compensated case, $\Delta t_d > \Delta t_c$, the propagation delay is not

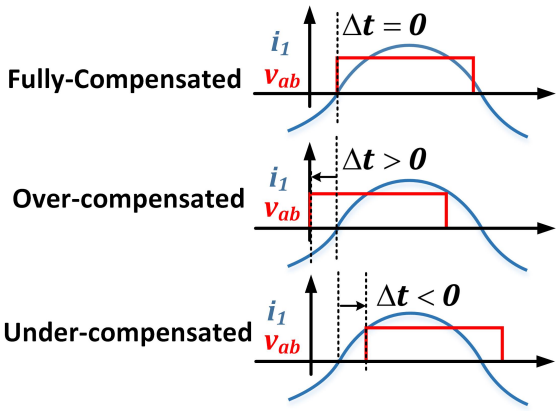

Figure 3.2: Three types of compensation method

fully compensated, causing the voltage to lag behind the current. The power factor is lower than 1 and, as mentioned in Section 3.2.2, there exists a risk of hard switching. To achieve soft switching, an over-compensate method can be applied with $\Delta t_d < \Delta t_c$. The voltage leads current by an over-compensated angle. However, the over-compensated method reduces the input power factor.

Figure 3.3 illustrates the influence of under-compensation and over-compensation on frequency drift. The circuit parameters selected for calculation are summarized in Tabel 3.1. It can be found that when the voltage lags current for 300ns, the working frequency is lower than that of the ideal PT-symmetric condition. Conversely, when the voltage leads the current by 300ns, the working frequency is higher than that of the ideal condition. This result indicates that propagation delay influences the working frequency of the circuit, emphasizing the necessity for compensation to achieve a PT-symmetric circuit.

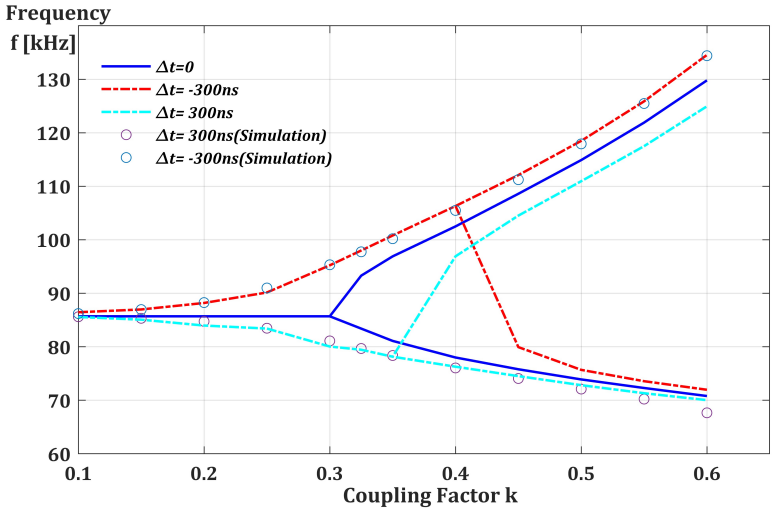

Figure 3.3: The working frequency drift due to delay and over-compensation based on the theoretical calculation and experiment results

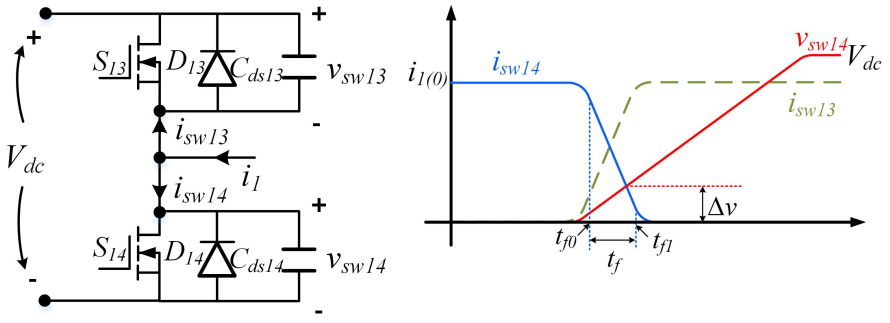

Figure 3.4: Inverter switching off transient waveform

3.2.2 Soft Switching of the H-Bridge Inverter

3.2.2.1 Soft switching off

Considering the case when inverter changes from working interval ② to ③ in Figure 2.3, the waveform of the current and voltage in the MOSFET of inverter are shown in Figure 3.4. At the end of working interval ②, $i_1 > 0$ and S_{14} is turning off with $i_{sw14} > 0$, the drain to source capacitor C_{ds14} is charged by i_{sw14} to increase the voltage drop v_{sw14} on S_{14}. The current i_{sw14} will decrease to 0 within a current fallen time of t_f, which can be found in the data sheet. Therefore the voltage rising Δv within $t \in [t_{f0}, t_{f1}]$ can be calculated as follows:

$$\begin{aligned} \Delta v &= \frac{1}{C_{ds14}} \int_{t_{f0}}^{t_{f1}} i_{sw14}(t)\, dt \\ \Rightarrow \Delta v &\approx \frac{i_{1(0)} t_f}{2C_{ds14}} \end{aligned} \tag{3.11}$$

and the turn off loss can be calculated as:

$$\begin{aligned} \Delta E_{off} &= \int_{t_{f0}}^{t_{f1}} i_{sw14}(t) v_{sw14}(t)\, dt \\ \Rightarrow \Delta E_{off} &\approx \int_{t_{f0}}^{t_{f1}} [\frac{-i_{1(0)}}{t_f}(t - t_{f1}) \cdot \frac{\Delta v}{t_f}(t - t_{f0})]\, dt \\ \Rightarrow \Delta E_{off} &\approx \frac{i_{1(0)} \Delta v}{6} t_f = \frac{i_{1(0)} t_f^2}{12 C_{ds14}} \end{aligned} \tag{3.12}$$

From (3.11), it can be observed that the voltage rise on the switch during turn off depends on the current fallen speed, initial current and the D-S capacitance. For the MOSFET module used in this thesis, it can be found in the data sheet that the fallen time $t_f \approx 50$ns and $C_{ds14} \approx 5$nF. Assuming that the switching off current $i_{sw14} = 5$A and the working frequency $f_{sw} = 85$kHz, the voltage rise can be calculated using (3.11) as $\Delta v = 25$V, and the turn off loss in inverter can be calculated using (3.12) as $\Delta P_{off} = 4\Delta E_{off} f_{sw} = 0.35$W. It shows that the turn off loss in inverter is much smaller than the rate power of the system. Thus, it has very insignificant influence on the system efficiency.

When the switch is turned off, the D-S capacitance of the switch prevents the rapid voltage rising [43]. Thus, the switches of inverter are regarded as soft switching off in this thesis.

3.2.2.2 Soft switching on

Soft switching on can be achieved using reactive current as the reverse current [44]. Let's consider a scenario with inverter duty cycle D_1 (with $D_1 \in (0, 0.5)$), Figure 3.5 shows the waveform of inverter output voltage, output current, gate signal. The switching process happens during the blanking time (highlighted with red region) in the figure. For the case shown in the figure, when S_{12} turns off and S_{11} turns on in ②, the positive current can not discharge the D-S capacitor C_{ds11}. As a result, S_{11} works in a hard switching on condition. Similar analysis can be applied in ④ when S_{14} turns off and S_{13} turns on. The positive current i_1 can charge the capacitor C_{ds14} and discharge C_{ds13}. Therefore, S_{13} works in soft switching on condition provided that C_{ds13} is fully discharged during the blanking time.

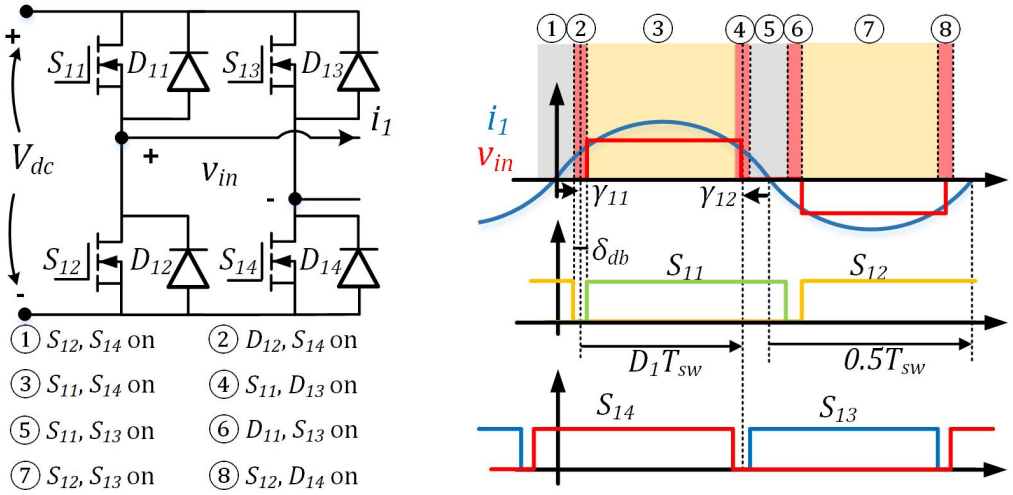

Figure 3.5: The gate signals, inverter output voltage and transmitting coil current in inverter.

It can be concluded that in the hard operation case, S_{11} has turn-on loss because the inverter output voltage lags the current. As the positive i_1 is not able to discharge the D-S capacitor D_{ds11}. On the other hand, in soft switching case, S_1 works in ZVS mode when turned on as the inverter output voltage leads the current. As the reverse current helps to discharge the D-S capacitor C_{ds11} during the blanking time. Similar analyses can be applied to other switches. To achieve an operation with soft switching on, the following conditions must be fulfilled:

$$\begin{cases} \gamma_{11} = (\Delta t_d - \Delta t_c)\dfrac{2\pi}{T_{sw}} + \dfrac{\delta_{db}}{2} + (\dfrac{1}{2} - D_1)\pi < 0 \\ \gamma_{12} = \pi - (\gamma_{11} + 2D_1\pi) > 0 \end{cases} \tag{3.13}$$

Where γ_{11} is the phase difference between the positive zero crossing of transmitting current and the gate signal S_{11}. γ_{12} is the phase difference between the negative

zero crossing of transmitting current and the gate signal S_{13}. The direction of the phase difference is defined in Figure 3.6.

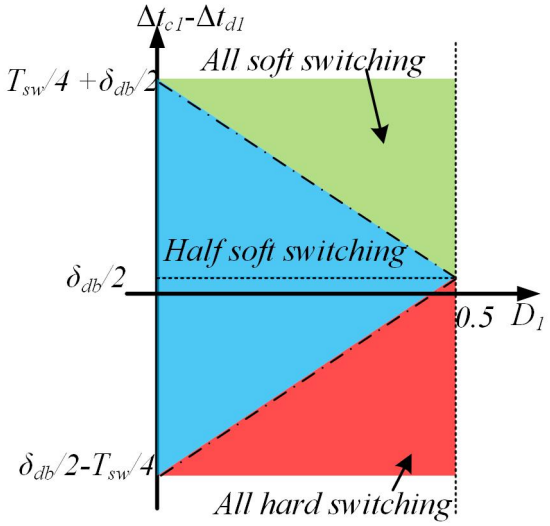

Figure 3.6: Soft switching boundary of inverter

According to (3.13), the boundary of soft switching operation for the inverter can be visualized as shown in Figure 3.6. Soft switching operation can be achieved easily in over-compensated condition ($\Delta t_{c1} > \Delta t_{d1}$). As the duty cycle D_1 decrease, a larger compensation is required to maintain the soft switching condition. However, this can result in a reduction in power factor, and the excessive reactive current will increase the transmitting loss in the coil.

3.2.3 Soft Switching of the Rectifier

The waveform of receiving coil current i_2, voltage v_2, and the drive signal for rectifier are shown in Figure 3.7. Once again, the blanking time ②, ④, ⑥, and ⑧ are investigated. From interval ① to ②, i_2 can be used to charge C_{ds22} and discharge C_{ds21}. After the D-S capacitor C_{ds21} is fully discharged, i_2 will conduct through D_{21} during the blanking time. Therefore, S_{21} is in soft switching on condition. From interval ③ to ④, the positive current i_2 can not discharge the capacitor C_{ds23}, and thus, at the end of the blanking time, S_{23} works in a hard switching condition. Similar analysis can be applied to the other intervals. It can be concluded that soft switching boundary depends on the compensation Δt_{c2}, duty cycle D_2 and control system propagation delay Δt_{d2} of rectifier. To achieve soft switching operation, the following conditions shall be satisfied:

$$\begin{cases} \gamma_{21} = \Delta t_{d2} - \Delta t_{c2} + (\frac{1}{2} - D_2)\frac{T_{sw}}{2} - \frac{\delta_{db}}{2} > 0 \\ \gamma_{22} = \gamma_{21} - \frac{\delta_{db}}{2} + 2D_2\pi + \frac{\delta_{db}}{2} > \pi \end{cases} \tag{3.14}$$

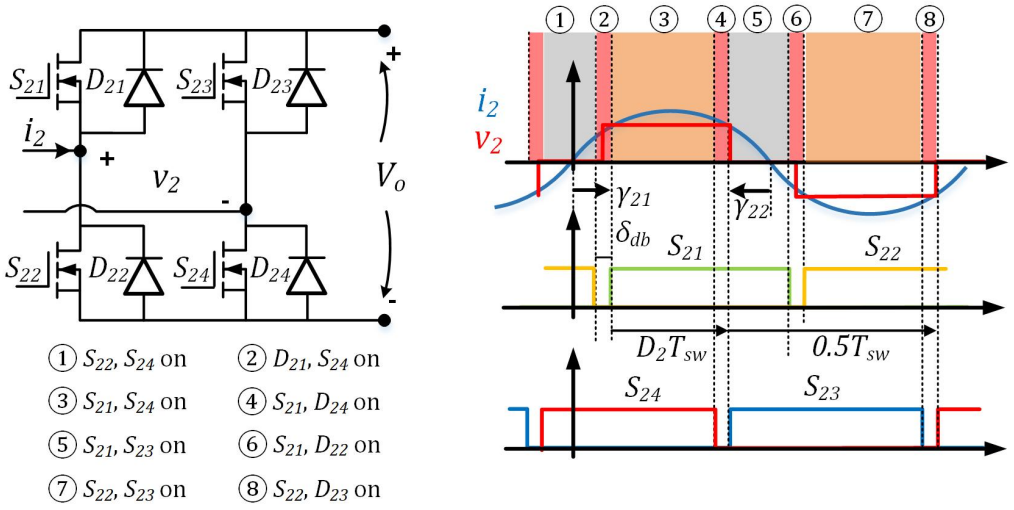

Figure 3.7: The gate signals, rectifier input voltage, and receiving end current

Where γ_{21} is the phase shift from positive zero crossing of current i_2 to the rising up of line voltage v_2, and γ_{22} is the phase shift from negative zero crossing of i_2 to the falling down of line voltage v_2. To achieve soft switching on, the shunt diode shall be conducting during the blanking time before the MOSFET is turned on. S_{21} and S_{22} work in soft switching on condition when the switching signals lag the positive zero crossing of i_2. S_{23} and S_{24} can work in soft switching condition when the turn-on signals lead the negative zero crossing of i_2. Figure 3.8 shows the soft switching boundary of the rectifier.

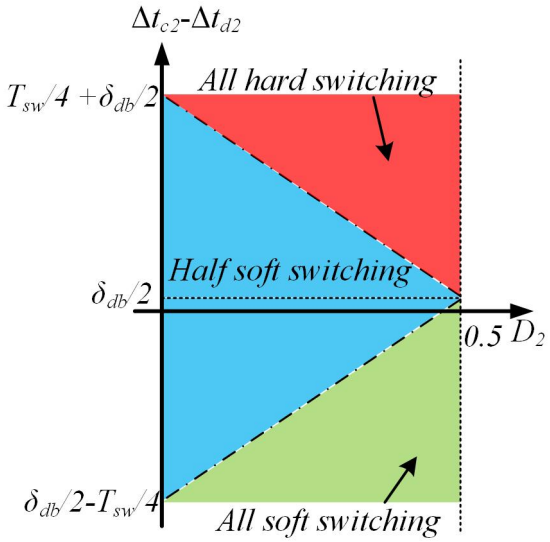

Figure 3.8: Soft switching boundary of rectifier

3.2.4 Digital Control Scheme Considering Compensation

In this thesis, compensation is achieved through the digital control method illustrated in Figure 3.9. The duty cycle of voltage (v_{ab}) is controlled by introducing a phase shift β between gate signal $v_{s1}(\bar{v}_{s2})$ and $v_{s4}(\bar{v}_{s3})$. To produce a symmetric three-level line voltage waveform with duty cycle D_1, the phase shift can be calculated as:

$$\beta = (\frac{T_{sw}}{2} - D_1 T_{sw})/2 \tag{3.15}$$

The control process can be described as follows: First, the current is measured by the Rogowski coil as i_{1m}. The CTR is reset to 0 when DSP receives the rising zero crossing of i_{1m}. The current frequency can be calculated by measuring the time between two rising zero crossings. According to the latest measured current frequency, the switching frequency $1/T_{sw}$ and the compare values CMPA (CMPC) and CMPB (CMPD) are updated. As shown in Figure 3.9, v_{s1} is set when CTR reaches CMPA (CMPC) and cleared when CTR reaches CMPB (CMPD). For an inverter with duty cycle D_1, the comparable value CMPA (CMPC) and CMPB (CMPD) can be determined as follows:

When the phase shift β is less than the compensation α_c ($\alpha_c = 2\pi\Delta t_c/T_{sw}$), we have

$$\begin{cases} \text{CMPA} = \dfrac{T_{sw}}{T_{clk}}(1 - \dfrac{\alpha_c}{2\pi} + \dfrac{\beta}{2\pi}) \\ \text{CMPB} = \text{CMPA} - \dfrac{T_{sw}}{2T_{clk}} \\ \text{CMPC} = \text{CMPB} - \dfrac{\beta}{\pi}\dfrac{T_{sw}}{T_{clk}} \\ \text{CMPD} = \text{CMPC} + \dfrac{T_{sw}}{2T_{clk}} \end{cases} \tag{3.16}$$

when the phase shift β is larger than the compensation α_c, we have

$$\begin{cases} \text{CMPA} = \dfrac{T_{sw}}{T_{clk}}(\dfrac{\beta}{2\pi} - \dfrac{\alpha_c}{2\pi}) \\ \text{CMPB} = \text{CMPA} + \dfrac{T_{sw}}{2T_{clk}} \\ \text{CMPC} = \text{CMPB} - \dfrac{\beta}{\pi}\dfrac{T_{sw}}{T_{clk}} \\ \text{CMPD} = \text{CMPC} + \dfrac{T_{sw}}{2T_{clk}} \end{cases} \tag{3.17}$$

Similarly, the control scheme of rectifier can be obtained. The program flow chart of inverter is shown in Figure 3.10. In this system, the working frequency is kept at low working frequency $f_l (2\pi f_l = \omega_l$ in Equation (3.4)) to reduce switching losses. The initial switching frequency $f_{init} = 60$kHz. The maximum switching frequency is set to be $f_{sw\cdot max} = f_0 = 85$kHz. As when the measured current frequency $f_{sw} > f_0$, the system is working in the broken PT-symmetric region and the only solution satisfying $X_n = 0$ is $f_{sw} = f_0$. According to the result in Figure 3.3, the working

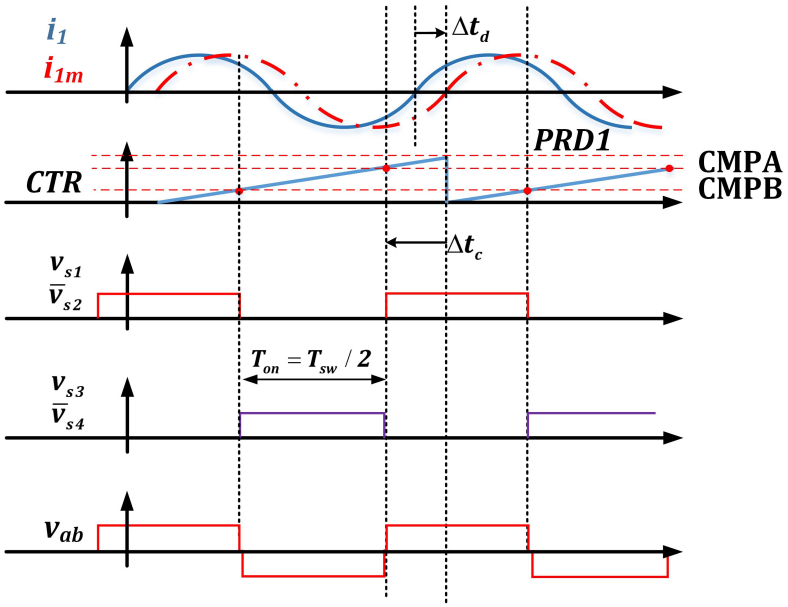

Figure 3.9: Drive signal generation method based on compensation (the current i_1 and i_{1m} are regarded as pure sinusoidal wave in the analysis)

frequency is in the range of $f_{sw} \in [65, 85.5]$kHz when the coupling factor changes from 0.6 to 0.1. Therefore, the minimum frequency can be set as $f_{sw \cdot min} = 60$kHz to avoid runaway.

Similar control scheme is applied to rectifier. It is worth noting that the propagation delay in rectifier does not cause hard switching issue, but it reduce the output power factor. The control scheme flow chart for rectifier is shown in Figure 3.11. The rectifier works in diode model during the start up of system. The rising zero crossing of current is captured and counted. For any time interval, the switching frequency f_2 is calculated as the average frequency of the latest five measurement results. Once the number of captured zero crossing $k > k_{stab}$, the driver signal is active, and the rectifier works in DAB condition.

The compensation is accomplished through the digital control method, offering several advantages. The delay in the sample and control circuit can be effectively compensated through digital control to achieve a negative resistive source. This eliminates the need for additional compensation circuits and provides tunable compensation.

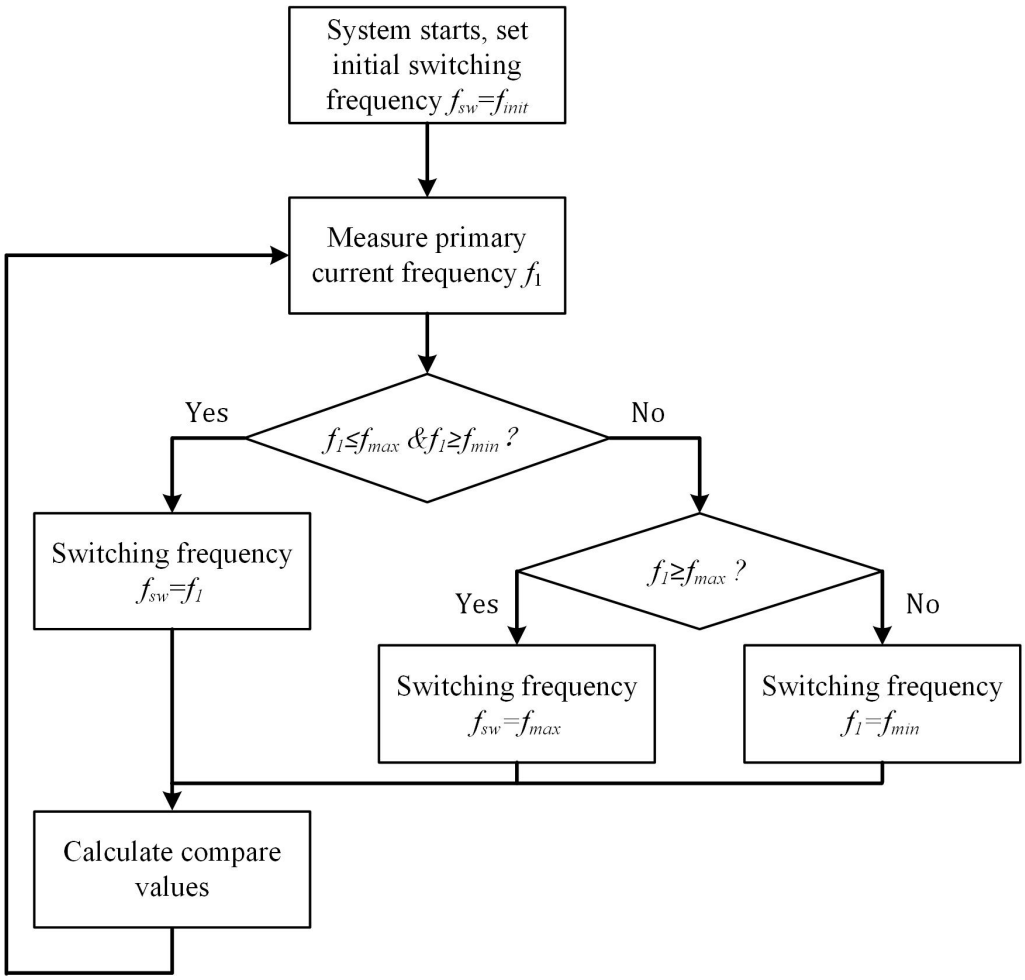

Figure 3.10: Controller flow chart for inverter

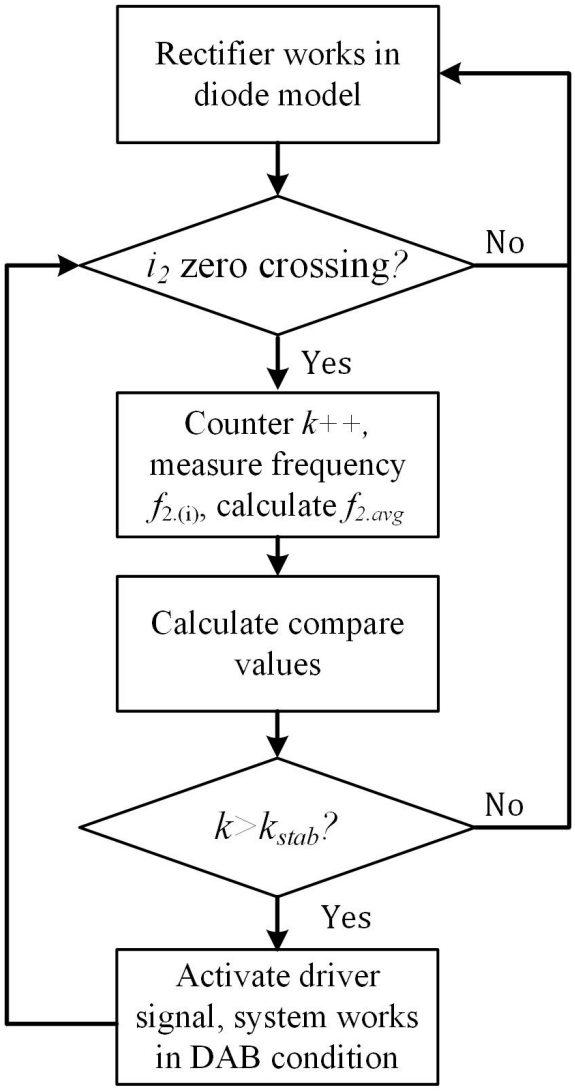

Figure 3.11: Controller flow chart for rectifier

3.3 Diode Rectifier Simulation and Experiment

3.3.1 Introduction to the setup

An IPT system with diode rectifier, as shown in Figure 2.13, is modeled and simulated in SIMULINK (see Figure 3.12). To simplify the problem, the receiving end drive signal is inactive so the current will conduct through the body diode of MOSFETs. In principal, if the rectifier is lossless, the equivalent rectifier duty cycle $D_2 = 0.5$. The parameters used in the simulation are the same as fixed-frequency simulation set up in Table 2.2. The control scheme of inverter follows the description in Figure 3.10.

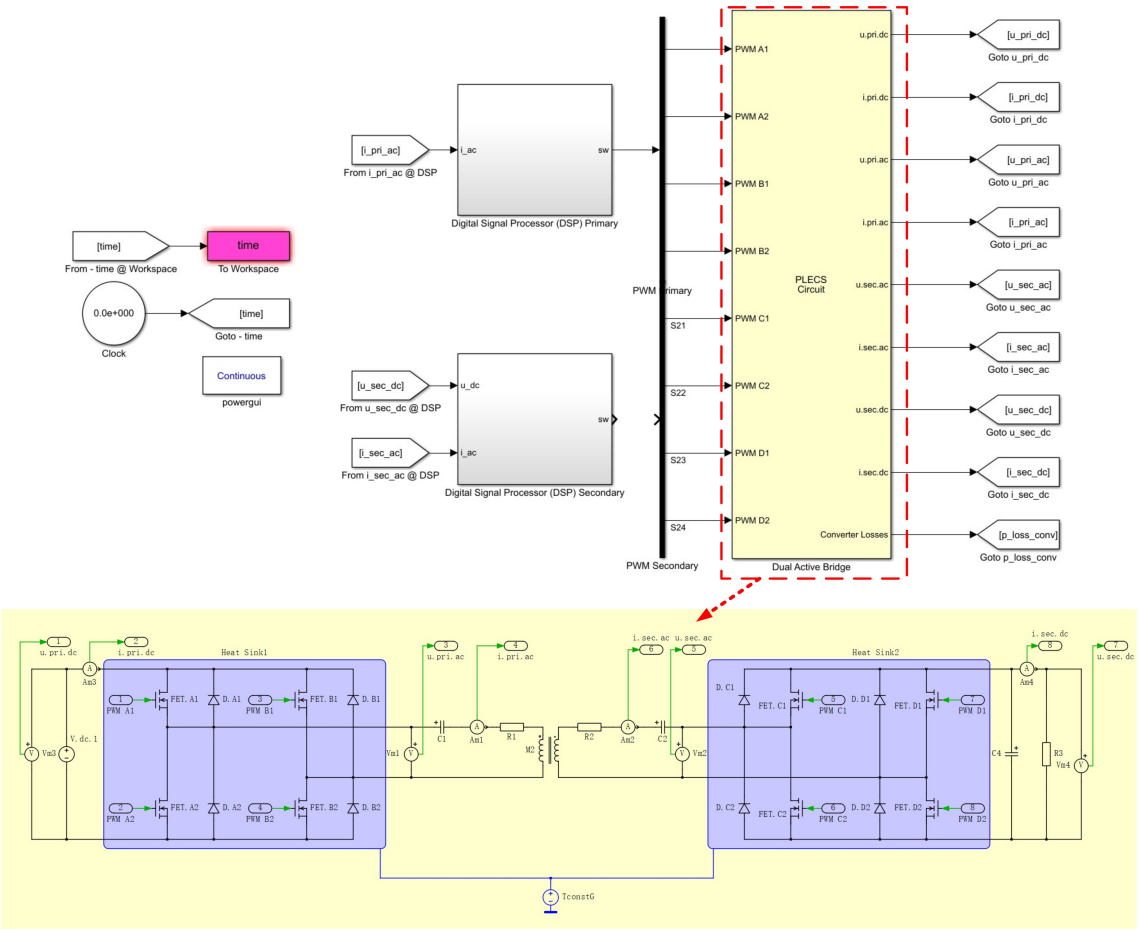

Figure 3.12: The simulation setup of diode IPT system, the receiving end bridge is inactive with $D_2 = 0.5$

The delay in control circuit can be modeled in SIMULINK by putting a transport delay block in CTR counter. The configuration of CTR counter is shown in Figure 3.13. There are two situations to reset the CTR: (1). when CTR=PRD, (2). rising zero crossing of current is detected. We can assume that the propagation delay in control circuit affects only the second situation. Since the delay in capturing zero crossing is much larger than the internal reset of CTR register.

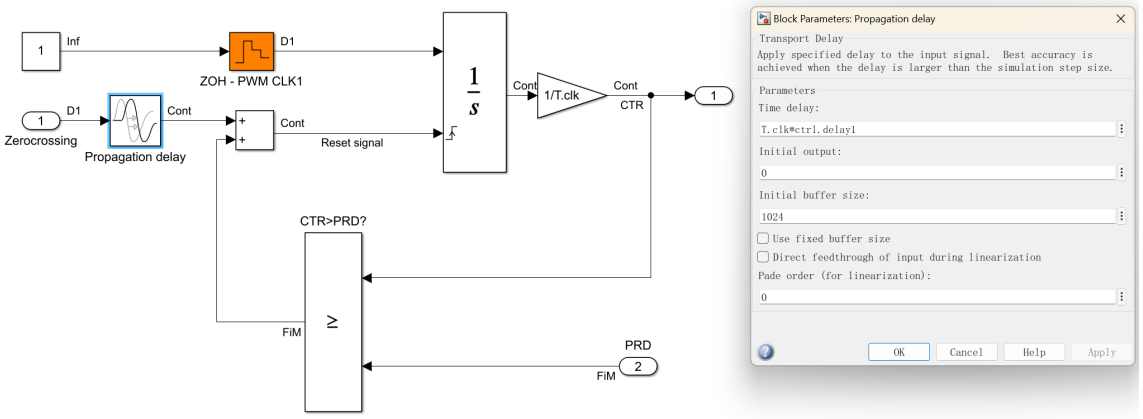

Figure 3.13: The configuration of the CTR counter, the propagation delay is modeled with a transport delay block, and the delay time is measured from experiment ($\Delta t_d = 1800$ns)

An equivalent experiment is performed to validate the simulation result. The experiment setup is illustrated in Figure 2.13 and 2.14. In this experiment, first, the effect of compensation and delay on system working frequency and efficiency is investigated. Subsequently, the horizontal misalignment d between coils is changed to study the performance of the PT-symmetric circuit in different compensation conditions. A synchronization circuit (see Figure 3.14) is employed to synchronize the inverter output voltage with the current. A Rogowski coil is applied to measure the transmitter current. The rising zero crossing of current is captured by the amplifier and comparator. The comparator and amplifier are selected to have a bandwidth that can cover 100kHz. The rising time is small to provide fast respond and high resolution. The zero crossing signal is then acquired by the DSP (see Figure 3.15a), which generates signals (see Figure 3.9) to control the gate driver. The total propagation delay in the synchronization circuit consists of current sensor delay, amplifier delay, DSP delay, and driver delay, measuring a total of $\Delta t_d = 1800ns$. This system has high misalignment tolerance when it operates in the PT-symmetric phase. Besides, soft switching can be achieved when the system works in the over-compensated mode.

In this subsection, we compare the output power of coupling independent IPT system and fixed-frequency IPT system under various coupling condition. The effect of compensation on the waveform and efficiency of the system are discussed.

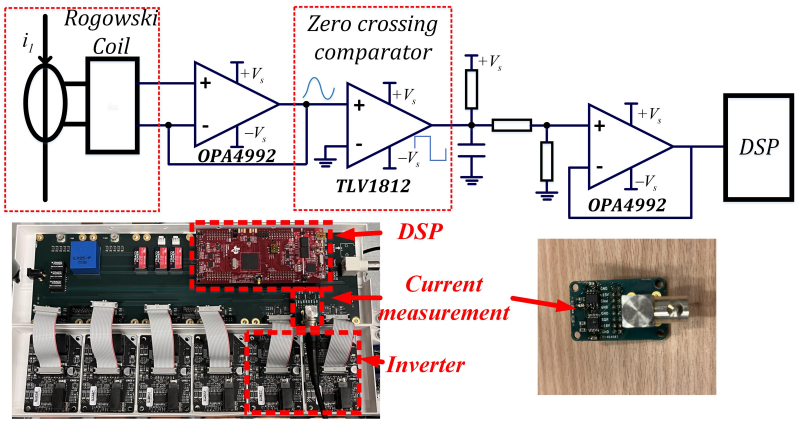

Figure 3.14: Current sampling and synchronization circuit

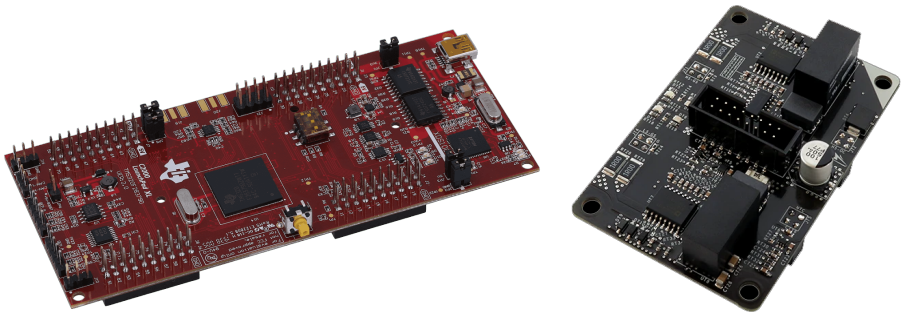

(a) F28379D launch pad (b) CGD12HBXMP

Figure 3.15: The DSP launch pad and the MOSFET gate driver

3.3.2 Result and analysis

Figure 3.16a compares the output power of the fixed-frequency and PT-symmetric systems. Analytical results, calculated based on (3.5) and (2.9), show good agreement with simulation results. According to (3.4), the critical coupling factor of the PT-symmetric system is $k_{crit} = 0.206$. For $k > k_{crit}$, the PT-symmetric system exhibits strong misalignment tolerance, maintaining a constant output power of 0.91kW. In the fixed-frequency system, output power is sensitive to changes in the coupling factor and the power decreases significantly when $k > k_{crit}$ and remaining lower than that of the PT-symmetric system. When $k \leq k_{crit}$, the system operates in the PT-broken phase, and the only working frequency to achieve unity power factor is $f_{sw} = f_0$. Consequently, both systems exhibit the same output power, and this output power increases as the coupling factor decreases.

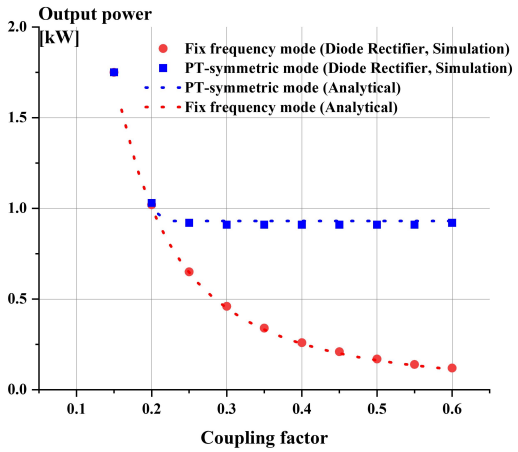

(a) A comparison of the output power of fixed-frequency system and PT-symmetric system ($R_L = 10\Omega$,$V_{dc} = 100$V).

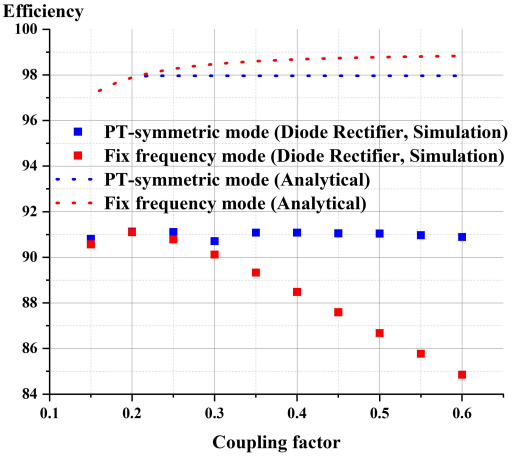

(b) A comparison of the efficiency of fixed-frequency system and PT-symmetric system ($R_L = 10\Omega$,$V_{dc} = 100$V)

Figure 3.16: A comparison of the power and efficiency of fixed-frequency system and PT-symmetric system

Figure 3.16b presents a comparison of the efficiency between the fixed frequency and PT-symmetric systems. The simulation results show significantly lower efficiency than the analytically calculated efficiency obtained from (3.7) and (2.10), as the analytical method calculates only the AC-AC transmission losses of fundamental component. In the fixed-frequency system, the DC-DC efficiency increases with a reduction in coupling. As the coupling factor decreases, the output power of the fixed-frequency system increases, leading to a rise in the load voltage for a constant resistance load. Therefore, the weight of forward voltage drop in power electronic devices reduces and the DC-DC efficiency increases.

The losses in the power electronic circuit, and the losses generated by harmonic can lead to a notable reduction in efficiency. The diode, with a forward voltage drop of 1.6V according to the datasheet, incurs substantial losses during conduction. These losses generate heat in the power electronic circuit, increasing thermal stress on the inverter and rectifier, potentially shortening the lifespan for power electronic devices.

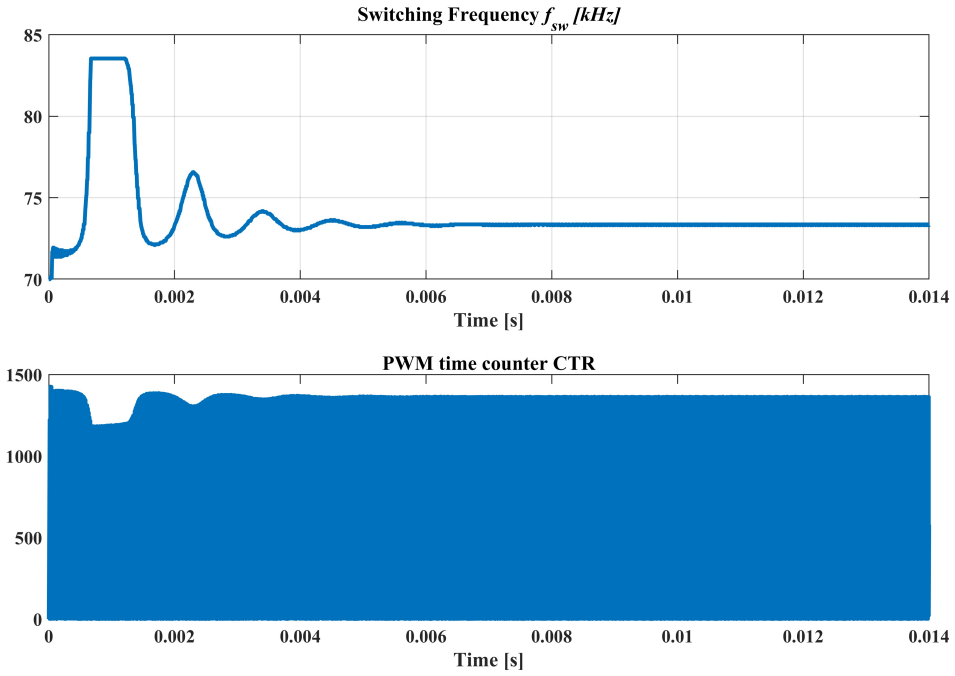

Figure 3.17: The variation of working frequency f_{sw} and counter register CTR in simulation(diode rectifier).($R_L = 10\Omega, V_{dc} = 100\text{V}, k = 0.4$)

The simulation shows the variation of working frequency f_{sw} and clock counter in DSP (see Figure 3.17). It can be observed that after applying the synchronization strategy, the working frequency converges to a specific value f_l when the system reaches steady state.

The compensation Δt_c is varied to examine the effect of different compensations on the system's operation. The input DC voltage is set to $V_{dc} = 200\text{V}$, and the load resistance is $R_L = 16\Omega$. The effect of compensation on frequency drift is shown in Figure 3.18. It is clear that the working frequency increases with higher compensation when the system works around f_l. The system operates in a PT-symmetric state when the propagation delay is fully compensated ($\Delta t_d = \Delta t_c = 1800\text{ns}$) and the working frequency in this PT-symmetric state is $f \approx 71\text{kHz}$, which agrees with the theoretical analysis. Figure 3.19a shows the output power of the system. It can be observed that the output power reduces when the system works in either an under-compensated state or a highly over-compensated state. In the under-compensated system, the propagation delay results in high switching loss (see Figure 3.20). A significant presence of harmonic components is evident in the current waveform.

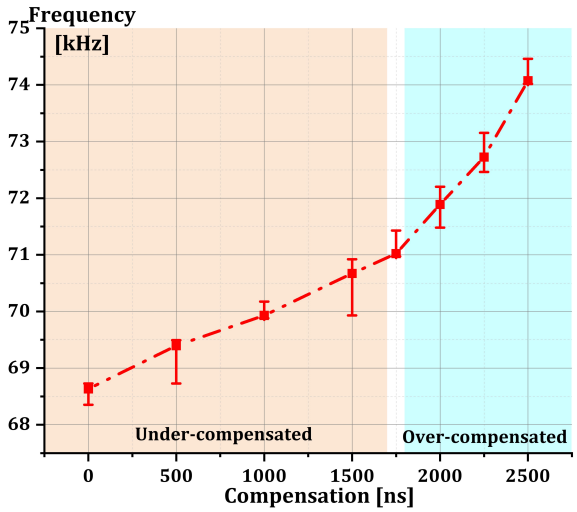

Figure 3.18: Experimental result of the system working frequency under different compensation conditions

As a result, in the highly under-compensated region, the efficiency of the system is low (see Figure 3.19b). Soft switching can be achieved in the over-compensated system, when the compensation further increases, the efficiency first increases and then decreases (see Figure 3.19b). This result is attributed to the fact that over-compensation increases the reactive current of the system, leading to increased conduction loss of the switch and transmission loss of the coils. The maximum efficiency can be achieved when the system is slightly over-compensated.

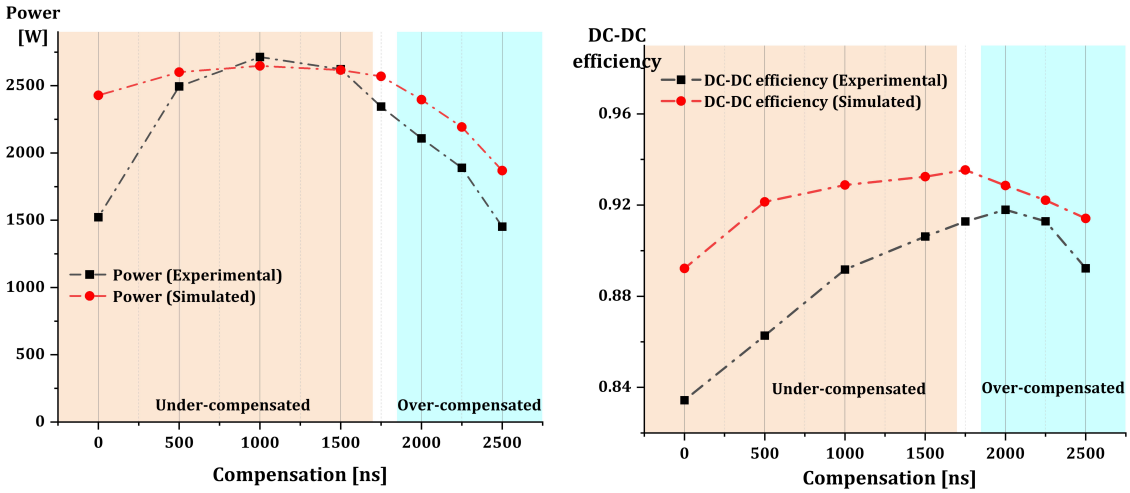

(a) Output power **(b)** DC-DC efficiency

Figure 3.19: Effect of compensation on system efficiency and output power ($V_{dc} = 200\text{V}, R_L = 16\Omega, k = 0.58$)

The performance of the system under various misalignment conditions d is investigated with a load resistance $R_L = 10\Omega$ and an input voltage of $V_{dc} = 100\text{V}$. The

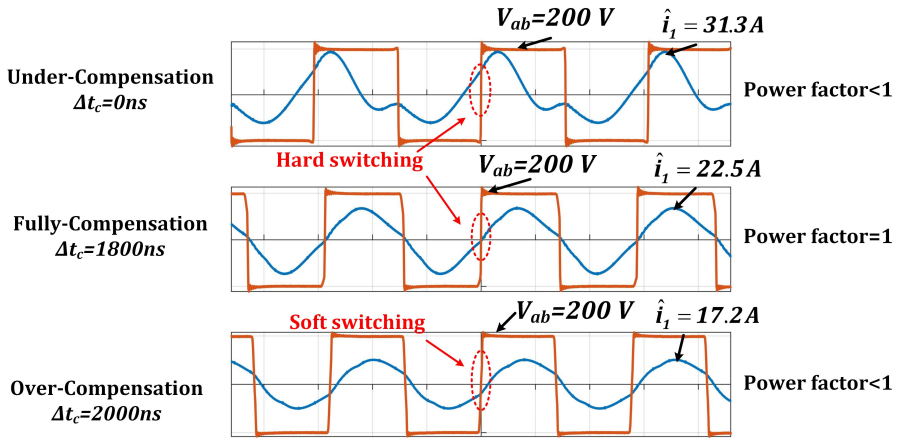

Figure 3.20: Experiment waveform with different compensations

result is shown in Figure 3.21. It can be observed in Figure 3.21a that in the fully-compensated condition ($\Delta t_c = 1800$ns), the system achieves constant output power in the PT-symmetric phase (with misalignment $d \in [0, 160]$mm), which agrees with the analysis. In the uncompensated case ($\Delta t_c = 0$ns), variations in output power are observed due to the frequency-dependent characteristic of output power. In both fully-compensated and uncompensated cases, the output power increases with the rise in misalignment in the PT broken phase. As the working frequency is kept at $f_0 = 85.5$kHz. The DC-DC efficiency is shown in Figure 3.21b. In the PT-symmetric phase, the fully-compensated system has higher efficiency than the uncompensated system. This is attributed to the fact that the uncompensated system has high switching loss due to hard switching and high transmission loss due to reactive current. Therefore, compensation is necessary to achieve high efficiency and constant power output in the PT-symmetric phase.

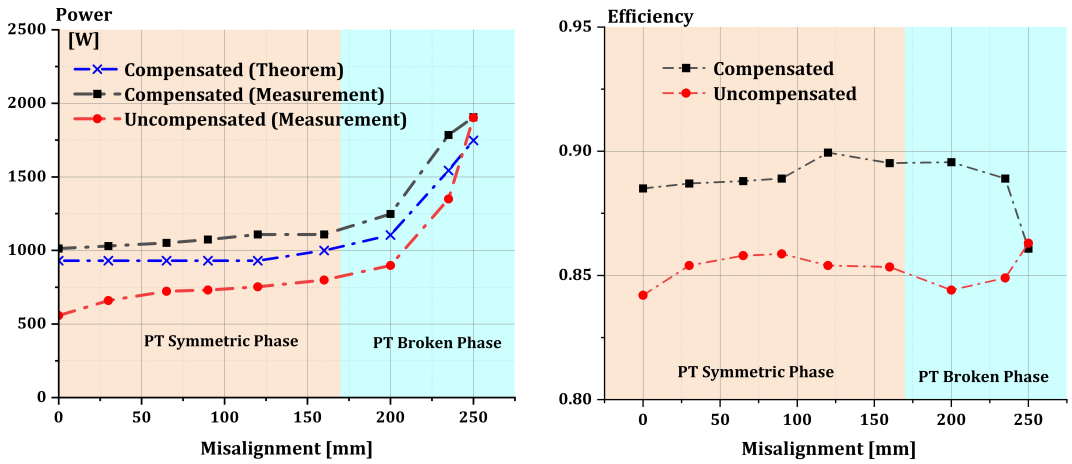

(a) Output power (b) DC-DC efficiency

Figure 3.21: Power and efficiency under different misalignment conditions ($V_{dc} = 100$V, $R_L = 10\Omega$)

3.4 Active Rectifier Simulation

3.4.1 Introduction to the setup

In this simulation, the rectifier is operating in active mode. The conducting losses in the MOSFET are much less than the losses in the body diode. Thus, one can expect a higher efficiency of the DAB topology. Furthermore, there exists the possibility to control the output power using secondary duty cycle D_2, which increases the flexibility of the system. The control flow chart of the active rectifier has been shown in Figure 3.11 and the calculation of compare values is shown in (3.16) and (3.17). The duty cycle of active rectifier varies from $D_2 = 0.5$ to $D_2 = 0.2$. The propagation delay is $\Delta t_d = 1800$ns in rectifier controller. This delay is the same as the delay in inverter controller, as the control circuit is the same. The compensation in rectifier controller is $\Delta t_c = 1800$ns to achieve a resistive load.

3.4.2 Result and analysis

Figure 3.22a shows a comparison of output power of diode and active rectifier system. When $k > k_{crit}$, the active rectifier system has higher output power. In strong coupling region, both of the systems have constant output power regardless the change of coupling. The result also indicates that the implementation of active rectifier has no influence on the performance of the PT-symmetric circuit.

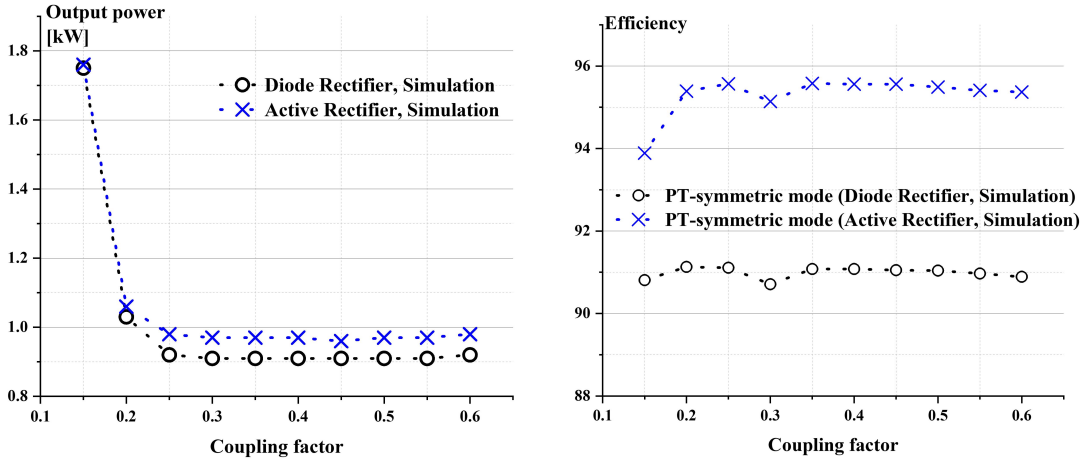

(a) A comparison of the output power of diode rectifier and active rectifier PT-symmetric system

(b) A comparison of DC-DC efficiency of the diode and active rectifier system ($R_L = 10\Omega, V_{dc} = 100$V)

Figure 3.22: Power and efficiency under different misalignment conditions (Active rectifier with $D_2 = 0.5$)

A comparison of the efficiency of the systems is illustrated in Figure 3.22b. The active rectifier system has higher efficiency as the MOSFET has lower conducting

and switching losses compared to the diodes in the rectifier. The efficiency in both systems is not constant. This is because the parameters in Table 2.2, measured from the experimental setup, are not exactly resonance matching (i.e., $\sqrt{C_1 L_1} \neq \sqrt{C_2 L_2}$).

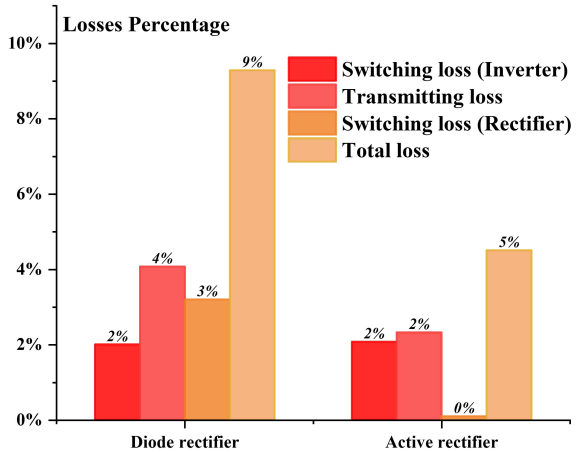

Figure 3.23: Weight percentage of losses in diode rectifier and active rectifier system($R_L = 10\Omega, V_{dc} = 100\text{V}, k = 0.35$)

The weight percentage of losses is shown in Figure 3.23. In both systems, the transmitting losses in the coil only account for 2% of the total losses. The remaining losses are distributed among power electronic components. In the diode bridge system, rectifier losses account for 3% of the total losses. By employing active control in the rectifier, the rectifier loss can be minimized. This is because the conduction loss in the SiC MOSFET is much smaller than that of the diodes.

Simulation result of working frequency f_{sw} and clock counter in DSP are shown in Figure 3.24. It can be observed that with $R_L = 10$, $D_2 = 0.5$, and $k = 0.4$, the working frequency converges to $f_{sw} = 73.2\text{kHz}$ when the system reaches steady state.

Figure 3.25 shows the output power of system under different duty cycle D_2 conditions. The equivlanet load seen from the input terminal of rectifier changes when the duty cycle D_2 changes. With a smaller R_{Leq}, the PT-symmetric region becomes larger. When the duty cycle D_2 changes from 0.2 to 0.5, the output power in PT-symmetric region increases. The output power in PT-broken region is lower.

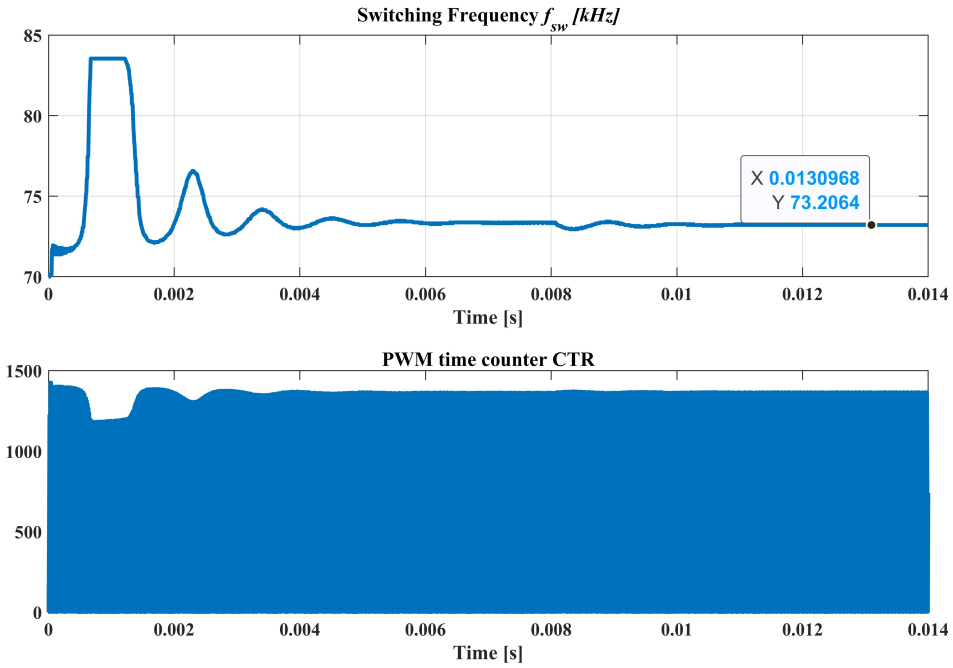

Figure 3.24: Simulation results of frequency f_{sw} and counter register CTR during the transient state and steady state(active rectifier).($R_L = 10\Omega, V_{dc} = 100\text{V}, k = 0.4$)

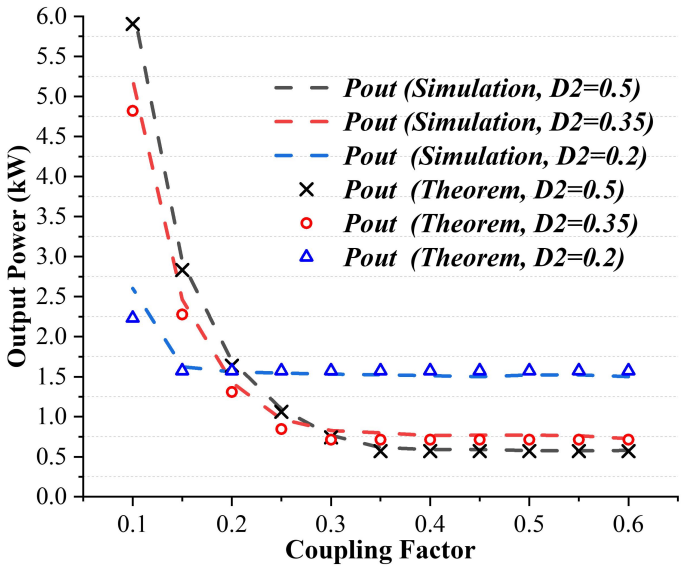

Figure 3.25: The output power of the system under different duty cycle D_2 ($R_L = 16.6\Omega, V_{dc} = 100\text{V}$)

4

Load Independent IPT System

4.1 Output Power Control Scheme of IPT System

By implementing the PT-symmetric control scheme, we have successfully developed a high misalignment tolerance IPT system. However, it has been observed that the output power and efficiency of the IPT system are notably sensitive to load variations, as discussed in Chapter 3. To mitigate this issue, several methods for controlling the output power of the IPT system are proposed in this chapter.

4.1.1 Active Rectifier Control Scheme

Substituting the equivalent load R_{Leq} in (2.7) into (3.5), we obtain the relationship between the rectifier duty cycle d_2 and the output power under PT symmetric conditions as follows:

$$P_{out} = \frac{\frac{8\sqrt{2}}{\pi^2}\sin(d_2\pi)^2 R_L V_{in}}{\frac{L_1}{L_2}(R_{Leq}+r_2)^2 + 2r_1(R_{Leq}+r_2) + \frac{L_2}{L_1}r_1^2} \tag{4.1}$$

Figure 4.1 illustrates the effect of duty cycle d_2 on the system's output power and efficiency. It can be observed that reducing d_2 increases the output power in the PT-symmetric phase. Furthermore, as the equivalent load R_{Leq} decreases, the critical coupling factor k_c of the PT-symmetric region also decreases, resulting in a larger PT-symmetric region. This system exhibits higher reliability as power control is managed from the receiving end, eliminating the need for communication. Additionally, the rectifier operates in a soft switching condition, as analyzed in Section 3.2.3. However, it is important to note that the system's working frequency will change with variations in the equivalent load, potentially affecting the stability of the system.

4.1.2 Input Voltage Control Scheme

Substituting the input voltage from equation (2.5) into the output power in equation (3.5), the relationship between DC link voltage V_{dc}, we derive the relationship between the DC link voltage V_{dc}, the inverter duty cycle d_1, and the output power P_{out} as follows:

$$P_{out} = \frac{2\sqrt{2}R_{Leq}V_{dc}sin(d_1\pi)/\pi}{\frac{L_1}{L_2}(R_{Leq}+r_2)^2 + 2r_1(R_{Leq}+r_2) + \frac{L_2}{L_1}r_1^2} \tag{4.2}$$

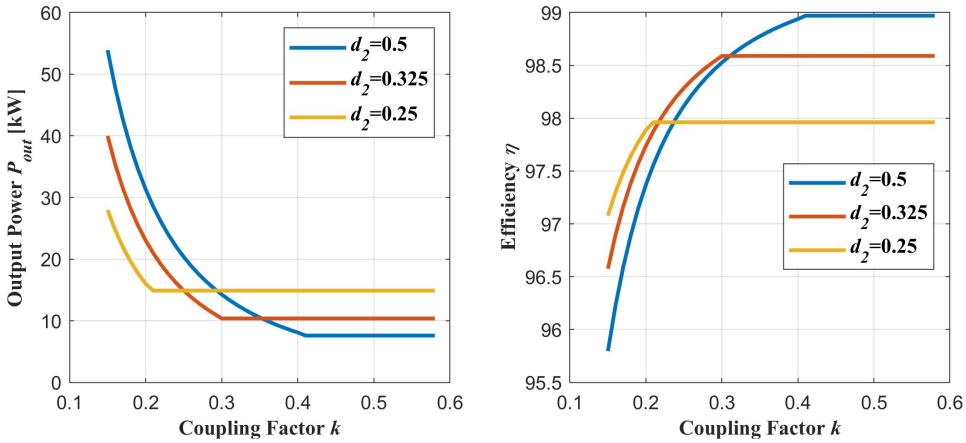

Figure 4.1: The change of output power and transmission efficiency with rectifier duty cycled$_2$ ($R_L = 20\Omega$, $V_{dc} = 400$V)

Hence, in the PT-symmetric region, the output power can be controlled by adjusting either the inverter duty cycle d_1 or V_{dc}. This control scheme is advantageous as it does not affect the working frequency of the system since it does not alter the equivalent load R_{Leq} or the coupling factor k. However, as discussed previously, achieving soft switching of the inverter requires that the rising edge of the input voltage v_{in} leads the transmitting coil current (see Figure 3.5). Therefore, severe hard switching operation may occur when the inverter duty cycle d_1 is low. To avoid severe hard switching operation, the inverter duty cycle is kept at $D_1 = 0.5$ in this thesis. The power control strategy adjusting the DC link voltage V_{dc} is investigated.

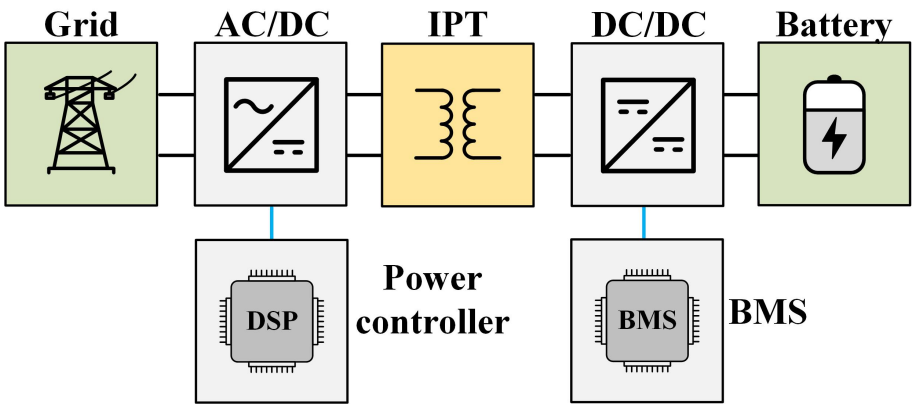

Figure 4.2: The configuration of the entire system

As shown in Figure 4.2, the rectifier connecting the grid and the IPT system can be utilized to regulate the DC link voltage. With an increasing number of power electronic systems connected to the grid, the harmonic pollution to the grid has become intolerable. Hence, the grid-connected rectifier is required not only to perform power factor control (PFC) but also to minimize harmonic current injection [45]. Various topologies and control methods have been proposed in the literature for the

design and control of grid-connected rectifiers [46–48]. The Vienna-type rectifier is commonly employed as the three-level boost rectifier in AC/DC transformation. In this chapter, the working principle, modelling, and control of single-phase PFC and three-phase Vienna rectifiers are proposed.

4.2 Modelling and Control of PFC

4.2.1 Modelling of Single Phase PFC

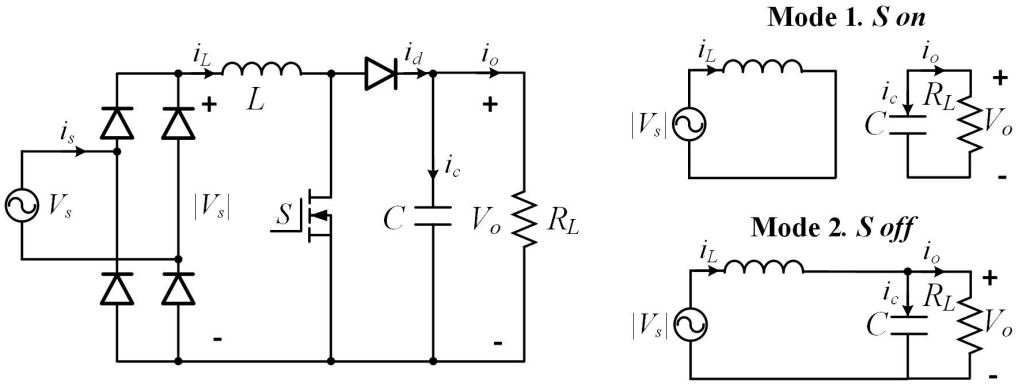

Figure 4.3: Schematic of single phase PFC

The schematic of a single-phase PFC circuit is depicted in Figure 4.3. In this configuration, the switching frequency f_{sw} is significantly higher than the grid frequency f_g. Throughout each switching period, the input voltage V_s and its absolute value $|V_s|$ can be considered constant. The circuit operates in two distinct phases, determined by the state of the switch, which can be described as follows:

In the first phase ($t \in [0, dT_{sw}]$, where d is the duty cycle of the switch), the switch S is turned on, and the diode is turned off. The properties of the circuit during this phase can be described by the following equations:

$$\begin{cases} L\dfrac{di_L}{dt} = |v_s| \\ C\dfrac{dv_o}{dt} = -\dfrac{v_o}{R_L} \end{cases} \tag{4.3}$$

In the second phase ($t \in (dT_{sw}, T_{sw}]$), the circuit exhibits the following properties:

$$\begin{cases} L\dfrac{di_L}{dt} = |v_s| - v_o \\ C\dfrac{dv_o}{dt} = i_L - \dfrac{v_o}{R_L} \end{cases} \tag{4.4}$$

We are interested in the average value in a single switching period. Therefore, by integrating equations (4.3) and (4.4) over a single switching period T_{sw}, we obtain

the following equations:

For the derivative of inductor current:

$$\begin{aligned} &\int_0^{T_{sw}} L\frac{di_L}{dt}dt = \int_0^{dT_{sw}} |v_s|dt + \int_{dT_{sw}}^{T_{sw}} (|v_s| - v_o)dt \\ \Rightarrow &L\frac{di_L}{dt} \approx L\frac{\Delta i_L}{\Delta t} = |v_s| - (1-d)v_o \end{aligned} \tag{4.5}$$

For the derivative of capacitor voltage:

$$\begin{aligned} &\int_0^{T_{sw}} C\frac{dv_o}{dt}dt = \int_0^{dT_{sw}} -\frac{v_o}{R_L}dt + \int_{dT_{sw}}^{T_{sw}} (i_L - \frac{v_o}{R_L})dt \\ \Rightarrow &C\frac{dv_o}{dt} \approx C\frac{\Delta v_o}{\Delta t} = -\frac{v_o}{R_L} + (1-d)i_L \end{aligned} \tag{4.6}$$

Rewrite the variables in (4.5) and (4.6) in the form of an operating point plus a small signal variation. As described in [48], The variables are expressed as follows:

$$\begin{cases} v_o = V_o + \tilde{v}_o \\ d = D + \tilde{d} \\ i_L = I_L + \tilde{i}_L \end{cases} \tag{4.7}$$

Here, V_o, D, and I_L represent the output voltage, the duty cycle, and the inductor current at the operating point, respectively. The terms $\tilde{v}_o$, $\tilde{d}$, and $\tilde{i}_L$ represent the small signal variations. Furthermore, for the operating point quantities, the following equations hold:

$$\begin{cases} I_L = \dfrac{V_o^2}{|V_s|R_L} \\ V_o = \dfrac{1}{1-D}|V_s| \end{cases} \tag{4.8}$$

By substituting (4.7) and (4.8) into (4.5) and (4.6), and ignoring second-order infinitesimals, we obtain the following equations:

$$\begin{cases} L\dfrac{d\tilde{i}_L}{dt} = -(1-D)\tilde{v}_o + V_o\tilde{d} \\ C\dfrac{d\tilde{v}_o}{dt} = -\dfrac{\tilde{v}_o}{R_L} + (1-D)\tilde{i}_L - \dfrac{V_o}{(1-D)R_L}\tilde{d} \end{cases} \tag{4.9}$$

By applying Laplace transform, the equations in frequency domain can be reached:

$$\begin{cases} sL\tilde{i}_L = -(1-D)\tilde{v}_o + V_o\tilde{d} \\ sC\tilde{v}_o = -\dfrac{\tilde{v}_o}{R_L} + (1-D)\tilde{i}_L - \dfrac{V_o}{(1-D)R_L}\tilde{d} \end{cases} \tag{4.10}$$

Based on (4.10), the controller can be built for the single-phase PFC.

To better understand the idea of small signal analysis, here comes a further explanation to the process above. To build the controller for the power electronic circuit, one needs to first described the system with a linear process model, such that $\frac{y}{x} = H(s)$, where x is the input, and y is the output, and $H(s)$ is the process model of the system. Here, by introducing zero-order Taylor expansion to the input and output quantities (i.e. $y = Y + \tilde{y}$, and $x = X + \tilde{x}$), one can obtain:

$$\begin{aligned} \frac{y}{x} &= \frac{Y + \tilde{y}}{X + \tilde{x}} = H(s) \\ \Rightarrow Y + \tilde{y} &= H(s)|_{\omega=0} X + H(s)\tilde{x} \end{aligned} \tag{4.11}$$

For the operating point quantities Y and X, we have $Y = H(s)|_{\omega=0} X$. Therefore, one can obtain the process model $H(s)$ as

$$\frac{\tilde{y}}{\tilde{x}} = H(s) \tag{4.12}$$

4.2.2 Control of Single Phase PFC

The block diagram of the controller of single phase PFC is shown in Figure 4.4. The controller consists of two loops. The current loop controls the inductor current i_L to follow the reference current i_{Lref}. The voltage loop controls the output voltage v_o to follow the reference output voltage V_{oref}. The structure of PI controller in current

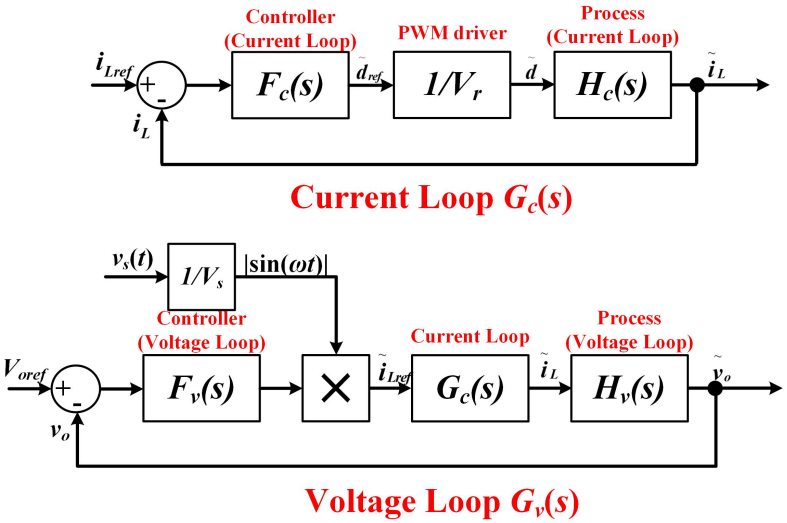

Figure 4.4: Block diagrams of the control loops in a single phase PFC

and voltage loop ($F_c(s)$ and $F_v(s)$) are shown in Figure 4.5. The value of duty cycle is controlled within the range of $d \in [0, 1]$. Thus an anti-windup loop is applied to let the controller return faster when saturation happens.

4.2.2.1 Current controller design

First, we start by describing the process block $H_c(s)$ in Figure 4.4. $H_c(s)$ describes the relationship between duty cycle $\tilde{d}$ and inductor current $\tilde{i}_L$. From (4.10), we

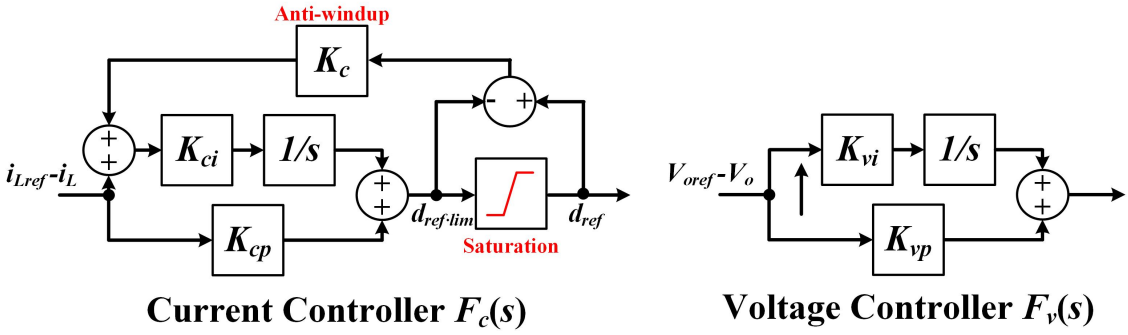

Figure 4.5: Block diagrams of the voltage and current controller ($F_v(s)$ and $F_c(s)$)

obtain the transfer gain $H_c(s)$ as

$$H_c(s) = \frac{\tilde{i}_L}{\tilde{d}} = \frac{V_o(R_L C s + 2)}{R_L C L s^2 + sL + R_L(1-D)^2} \tag{4.13}$$

It can be observed from (4.13) that the gain is related to duty cycle D and output voltage. To simplify the model, we assume $V_o = V_{oref}$. The bode plots of $H_c(s)$ under different duty cycle conditions are shown in Figure 4.6. The circuit parameters used in calculation are listed in Table 4.1. It can be found that the transfer functions have similar gain $|H_c|$ when the frequency $f \geq 1$kHz. For the single-phase PFC, the switching frequency is selected as $f_{sw} = 100$kHz. Thus, the transfer gain can be simplified as $H_c(s) \approx \frac{V_o}{Ls}$ as we focus on the rather high frequency band. The simplified result is plot in Figure 4.6 as well. It can be found that in the high frequency region, the simplified model shows a good agreement with the model obtained from equation (4.13).

Parameter	Value	Parameter	Value	Parameter	Value
R_L	64Ω	L	500μH	C	500μF
D	$[0.2, 0.5]$	V_{oref}	800V	f_{sw}	100kHz
V_s	230V	V_r	1	f_{grid}	50Hz

Table 4.1: The parameters of single-phase PFC

The PWM driver can be modeled as a gain $1/V_r$. In this thesis, we assume that the PWM driver can follow the reference instantly (i.e. $V_r = 1$). Now we design the current loop controller $F_c(s)$. A PI controller can be used to tune the bandwidth of the system. Let's set the bandwidth of the current loop as $f_c = 3$kHz, then the gain of PI controller at crossing frequency can be calculated as follows:

$$\begin{aligned} &20\log_{10}(|G_c(s)|_{f=f_c}) = 20\log_{10}(|F_c(s)H_c(s)|_{f=f_C}) = 0 \\ \Rightarrow &20\log_{10}(|F_c(s)|_{f=f_C}) = -20\log_{10}(|H_c(s)|_{f=f_c}) = -38.5 \\ \Rightarrow &20\log_{10}(\sqrt{k_{cp}^2 + \frac{k_{ci}^2}{(2\pi f_c)^2}}) = -38.5 \end{aligned} \tag{4.14}$$

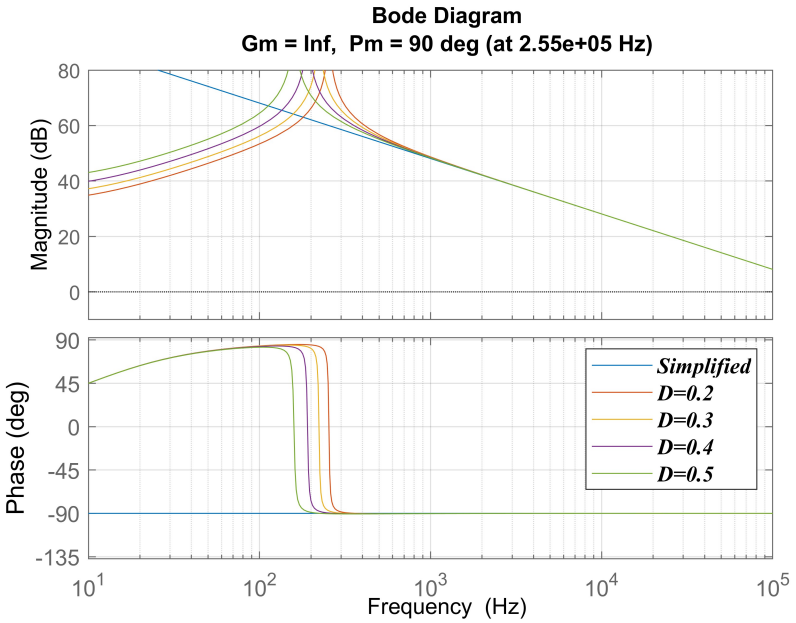

Figure 4.6: Bode plot of the process $H_c(s)$ for the current loop of the single phase PFC

As shown in Figure 4.6, the process of the current loop as a phase margin of 90°, which gives certain freedom on the selection of phase margin of the PI controller. In principal, the system shall have certain phase margin (ideally $\phi_m \geq 45°$) at crossing frequency

$$\begin{aligned} &\angle(G_c(s)|_{f=f_C}) = \angle(F_c(s)H_c(s)|_{f=f_C}) = -180° + \phi_m \\ \Rightarrow &\angle(F_c(s)|_{f=f_C}) + \angle(H_c(s)|_{f=f_C}) = -180° + \phi_m \\ \Rightarrow &\angle(F_c(s)|_{f=f_C}) = -90 + \phi_m \\ \Rightarrow &\frac{-k_{ci}}{2\pi f_c k_{cp}} = \tan(-90° + \phi_m) \end{aligned} \tag{4.15}$$

Select a phase margin of $\phi_m = 80°$ and solve equations (4.14) and (4.15), the parameters can be obtained as follows:

$$\begin{cases} k_{cp} = 0.012 \\ k_{ci} = 38.31 \end{cases} \tag{4.16}$$

The bode plot of current loop $G_c(s)$ is shown in Figure 4.7.

Finally, let's design the gain K_c in the anti-windup. The transfer gain from $d_{ref\cdot lim}$ to d_{ref} can be obtained as

$$\frac{d_{ref}}{d_{ref\cdot lim}} = \frac{s + k_{ci}k_c}{K_{ci}k_c} \tag{4.17}$$

The anti-windup can be designed to have a high bandwidth, which provides a faster response to let the saturation returns quicker. The bandwidth is selected as $f_c = 2f_{sw} = 200$kHz. According to (4.17), the gain k_c can be calculated as $k_c = 2\pi f_c/k_{ci} = 32802$.

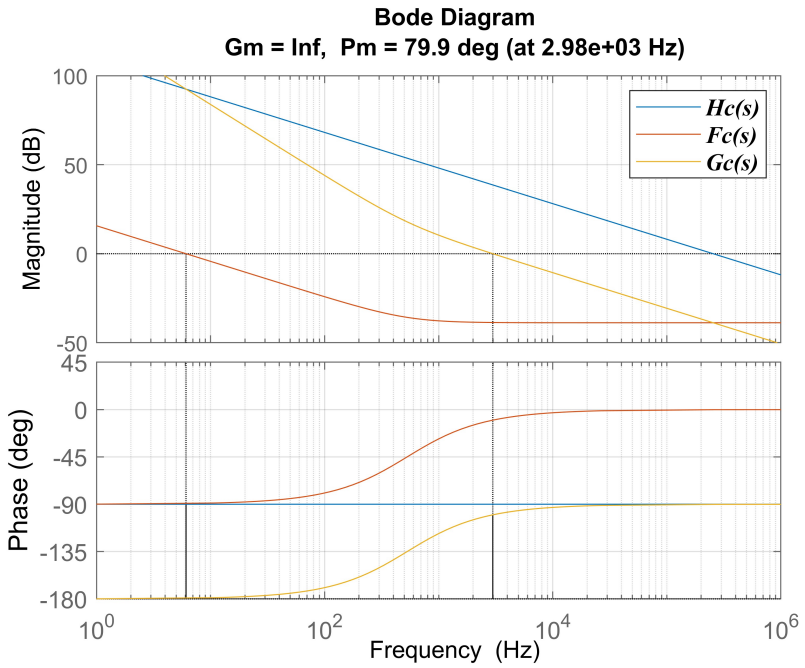

Figure 4.7: Bode plot of the current loop $G_c(s)$ of the single phase PFC

4.2.2.2 Voltage controller design

Similarly, one can determine the parameters of the PI controller for the voltage loop. From (4.8), we obtain the transfer gain of process $H_v(s)$ as

$$H_v(s) = \frac{\tilde{v}_o}{\tilde{i}_L} = \frac{[R_L(1-D)^2 - Ls]}{(1-D)(R_L Cs + 2)} \tag{4.18}$$

According to (4.18), the bode plots of voltage process $H_v(s)$ under different duty cycle conditions are shown in Figure 4.8. The duty cycle has insignificant influence on the gain of voltage process. Thus, without loss of generality, the controller is calculated using the case with $D = 0.5$.

It can be observed in Figure 4.8 that the open-loop bandwidth of voltage process ($H_v(s)$) is $f_c = 255$Hz, which is 10 times smaller than that of current loop. Thus, to simplify the analysis, the current loop is regarded as unity gain during the design of voltage controller. Similar to the calculation in (4.14) and (4.15), let's set the open-loop bandwidth of the voltage loop ($G_v(s)$) to be $f_c = 25$Hz, and the PI parameters for the voltage controller ($F_v(s)$) can be obtained as follows:

$$\begin{aligned} 20\log_{10}(|F_v(s)|_{f=f_c}) &= 20\log_{10}(\sqrt{k_{vp}^2 + \frac{k_{vi}^2}{(2\pi f_c)^2}}) = -18 \\ \angle(F_v(s)|_{f=f_c}) &= \frac{-k_{vi}}{2\pi f_c k_{vp}} = \tan(270^\circ + \phi_m) = \tan(270^\circ + 70^\circ) \end{aligned} \tag{4.19}$$

Then the parameters can be calculated as $k_{vp} = 0.1$ and $k_{vi} = 8.56$. Finally, the open-loop bode diagram of the voltage control loop $G_v(s)$ is shown in Figure 4.9.

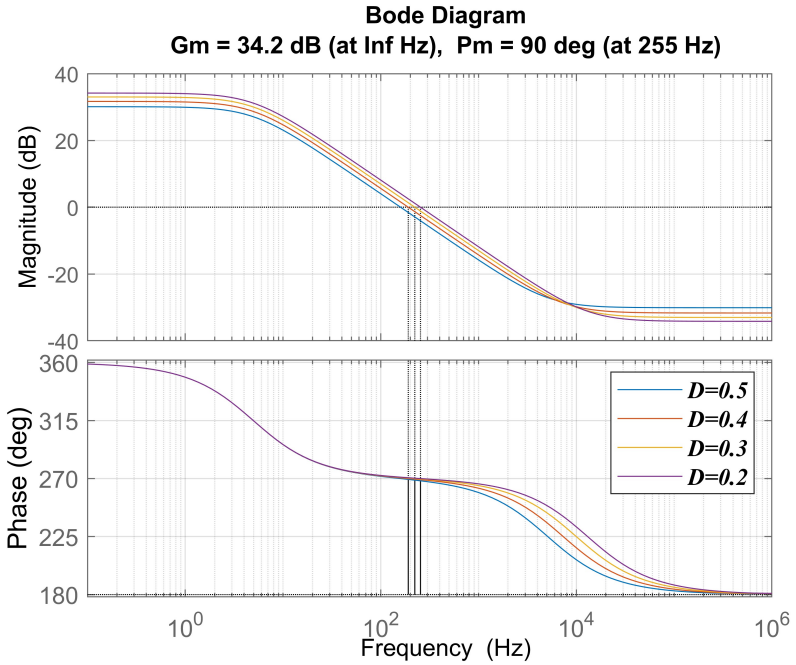

Figure 4.8: Bode plot of the process $H_v(s)$ for the voltage loop of the single phase PFC

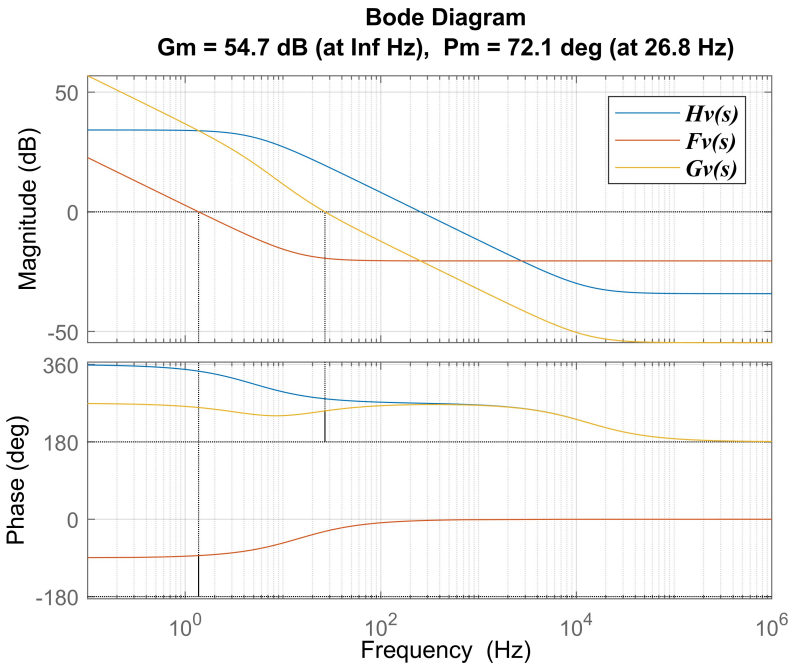

Figure 4.9: Bode plot of the voltage loop $G_v(s)$ of the single phase PFC

4.2.3 Simulation on Single Phase PFC

4.2.3.1 Introduction to the simulation setup

The parameters used in this simulation are listed in Table 4.1. The load is fixed as $R_L = 64\Omega$, and the output voltage reference V_{oref} is changed from $V_{oref} = 800$V to $V_{oref} = 640$V at time $t = 0.2$s.

4.2.3.2 Result and analysis

The output voltage of the single phase PFC is shown in Figure 4.10. The output voltage is a composition of DC voltage and a ripple voltage with frequency $f_{ripple} =$ 100Hz. The DC component follows the reference voltage. The exist of voltage ripple

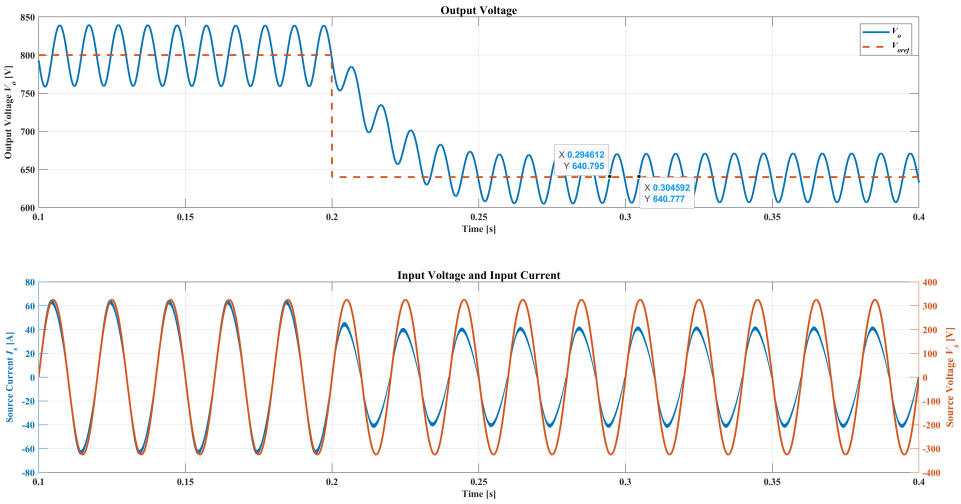

Figure 4.10: The simulation result of the input and output of the single-phase PFC

can be explained by power conservation. If we assume the diode bridge in Figure 4.3 is lossless, then the following equation can be obtained in a grid period

$$\begin{aligned} & v_s i_s = v_o i_d \\ & v_s = (1-d) v_o \\ \Rightarrow & i_d = (1-d) is \approx \frac{2V_s}{V_o} I_s \sin^2(\omega t) \\ \Rightarrow & i_d \approx \frac{V_s I_s}{V_o} - \frac{V_s I_s}{V_o} \cos(2\omega t) \end{aligned} \tag{4.20}$$

Where V_s and I_s are the RMS values of source voltage and source current, ω is the grid angular frequency. It can be found in (4.20) that the average diode current contains a DC component and a 100Hz current ripple, leading to a 100Hz ripple in the output voltage.

Figure 4.11 shows the change of duty cycle in the simulation. To evaluate the

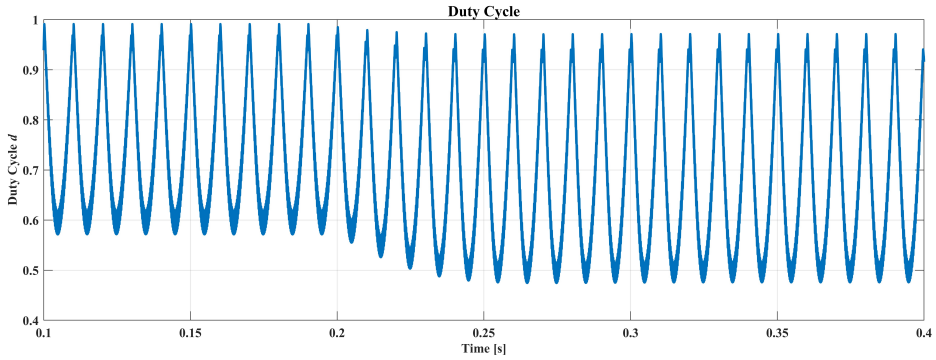

Figure 4.11: The simulation result of the duty cycle of the single-phase PFC

performace of PFC, FFT analysis is carried out on the source current. It can be found in Figure 4.10 that the source current contains certain amount of high order harmonics. The FFT result is shown in Figure 4.12. The total harmonic distortion in the source current is THD = 5.24%, which is defined as

$$\text{THD} = \frac{\sqrt{\sum_{i=2}^{\infty} I_{si}^2}}{I_{s1}} \tag{4.21}$$

Where I_{si} is the RMS value of the ith source current harmonic. The result in Figure 4.12 shows that the total harmonic mainly consists of third order and fifth order harmonic. A muti-phases PFC can be used to further reduce the harmonic component, reduce the output voltage ripple, and boost the output power.

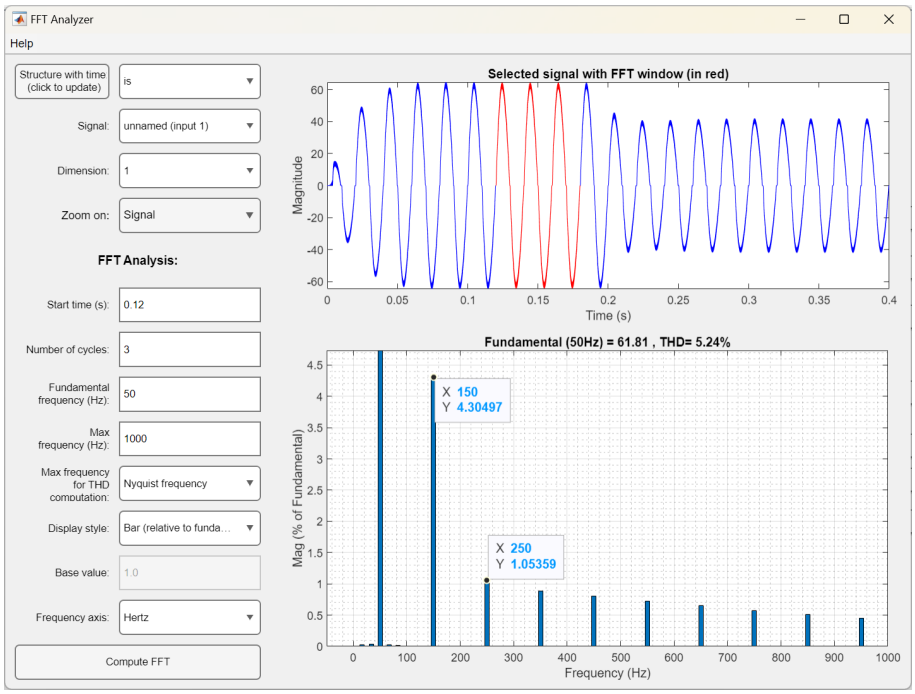

Figure 4.12: The FFT analysis on the input current of the single-phase PFC

4.2.4 Modelling of Vienna Rectifier

The working principle of a three-phase Vienna rectifier is similar to that of a single-phase PFC. A schematic of the three-phase Vienna circuit is shown in Figure 4.13. The active switches connect the neutral point N and the rectifier input ports x, y, and z. Consequently, based on the switch state and the direction of the source current, the circuit operates in four distinct modes for each phase. For clarity, let's examine the operating modes of phase A (see Figure 4.14).

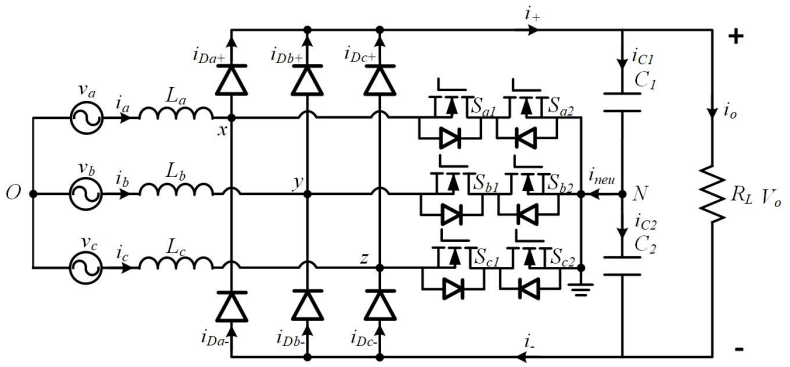

Figure 4.13: Schematic of three-phase Vienna PFC

Let's first consider the scenario where the phase current $i_a > 0$. When S_{a2} works in the on state (**Mode 1**), the point x is connected to the neutral. Diode D_{a+} and D_{a-} are off and the current i_+ and i_- conduct through y or z. When S_{a2} works in off state (**Mode 2**), the positive current i_a conducts through diode D_{a+}. When the phase current $i_a < 0$, the switch S_{a1} is controlled to connect the neutral with point x. following similar principles for **Mode 3** and **Mode 4** when the source current is negative. Based on the circuit and control strategy, we derive the following equation:

$$v_{a,b,c} = L\frac{di_{a,b,c}}{dt} + v_{(x,y,z)N} + v_{NO} \tag{4.22}$$

Where $v_{a,b,c} = [v_a, v_b, v_c]^T$, $i_{a,b,c} = [i_a, i_b, i_c]^T$ and $v_{(x,y,z)N} = [v_{xN}, v_{yN}, v_{zN}]^T$. Based on the mode analysis in Figure 4.14, the following equation holds:

$$v_{(x,y,z)N} = \text{sign}(i_{a,b,c})\frac{V_o}{2}(1 - d_{a,b,c}) \tag{4.23}$$

If we further define $v_{(x,y,z)N} + v_{NO} = \frac{V_o}{2}d'_{a,b,c}$, then we obtain:

$$\begin{aligned} v_{(x,y,z)N} &= \frac{V_o}{2}d'_{a,b,c} - v_{NO} \\ \Rightarrow v_{(x,y,z)N} &= \frac{V_o}{2}(d'_{a,b,c} + d_0) \end{aligned} \tag{4.24}$$

where $\frac{V_o}{2}d_0 \triangleq -v_{NO}$. By substituting (4.24) into (4.22), we have

$$v_{a,b,c} = L\frac{di_{a,b,c}}{dt} + \frac{V_o}{2}d'_{a,b,c} \tag{4.25}$$

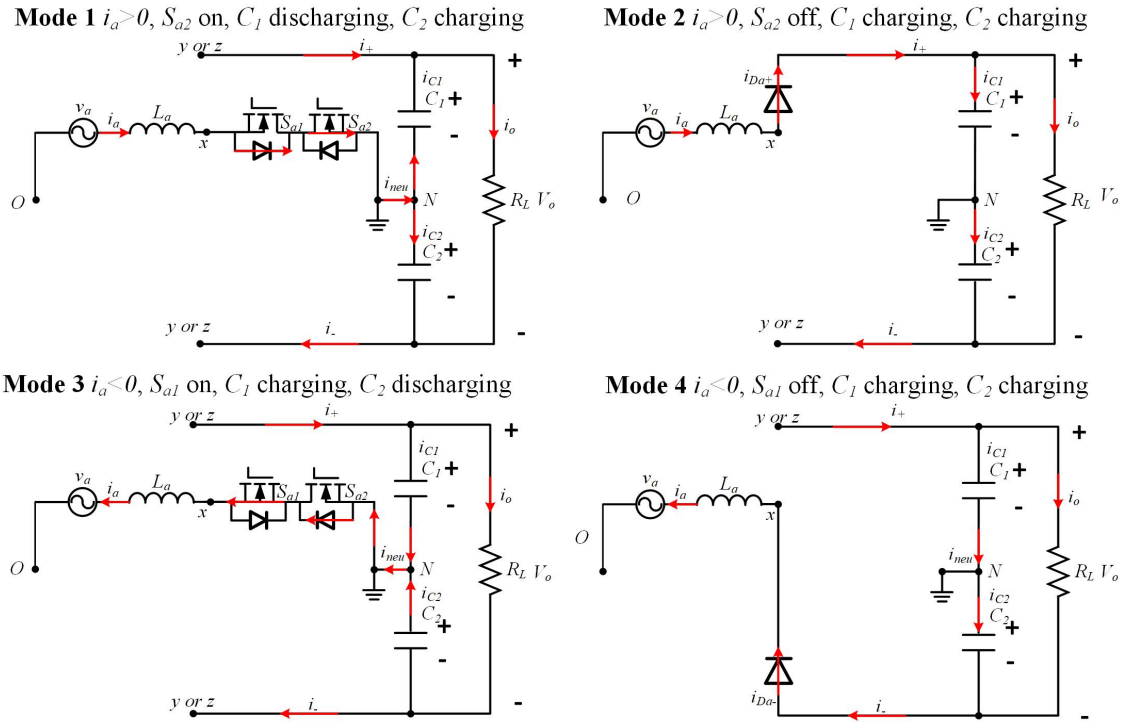

Figure 4.14: The working modes of three-phase Vienna circuit (take phase A as an example)

We hope to control the quantities in a DC frame, so a dq transformation matrix T_{dq0} can be applied to equation (4.25), from which we have

$$\begin{aligned} T_{dq0}v_{a,b,c} &= LT_{dq0}\frac{di_{a,b,c}}{dt} + \frac{V_o}{2}T_{dq0}d'_{a,b,c} \\ \Rightarrow v_{dq0} &= LT_{dq0}\frac{d[T_{dq0}^{-1}(T_{dq0}i_{a,b,c})]}{dt} + \frac{V_o}{2}d'_{dq0} \\ \Rightarrow v_{dq0} &= LT_{dq0}T_{dq0}^{-1}\frac{di_{dq0}}{dt} + LT_{dq0}\frac{dT_{dq0}^{-1}}{dt}i_{dq0} + \frac{V_o}{2}d'_{dq0} \end{aligned} \tag{4.26}$$

Then we have the equations in the dq-frame

$$\begin{cases} v_d = L\dfrac{di_d}{dt} - \omega L i_q + \dfrac{V_o}{2}d'_d \\ v_q = L\dfrac{di_q}{dt} + \omega L i_d + \dfrac{V_o}{2}d'_q \end{cases} \tag{4.27}$$

in the following section, we are going to design current loop in dq-frame based on (4.27). Consider the voltage on capacitors C_1 and C_2, one can obtain

$$\begin{cases} C_1\dfrac{v_{c1}}{dt} = i_+ - \dfrac{V_o}{R_L} \\ C_2\dfrac{v_{c2}}{dt} = i_- - \dfrac{V_o}{R_L} \end{cases} \tag{4.28}$$

If we assume $C_1 = C_2 = C$, further we have

$$\begin{cases} C\dfrac{dv_o}{dt} = i_+ + i_- - \dfrac{V_o}{R_L} \\ C\dfrac{d\Delta v}{dt} = i_+ - i_- \end{cases} \tag{4.29}$$

where $\Delta v = v_{c1} - v_{C2}$, $v_o = v_{C1} + v_{C2}$, $i_+ = i_{Da+} + i_{Db+} + i_{Dc+}$, and $i_- = i_{Da-} + i_{Db-} + i_{Dc-}$. Thus, we need further information about i_+ and i_- to describe the output voltage. Take phase A as an example, in a single switching period, based on energy conservation of diode rectifier, $v_{xN} i_a = \frac{V_o}{2} i_{Da+}$. By substituting it into equation (4.24), the average current of i_{Da+} in a switching period can be obtained as follows:

$$i_{Da+} = \frac{2v_{xN}}{V_o} i_a = (d'_a + d_0) i_a \tag{4.30}$$

Then the diode current can be described as follows:

$$i_{Da+} = \begin{cases} (d'_a + d_0) i_a & (i_a > 0) \\ 0 & (i_a < 0) \end{cases} \tag{4.31}$$

$$i_{Da-} = \begin{cases} 0 & (i_a > 0) \\ (d'_a + d_0) i_a & (i_a < 0) \end{cases} \tag{4.32}$$

Substitute (4.31) and (4.32) into i_+ and i_-, we have

$$\begin{aligned} i_+ + i_- &= (d'_a + d_0) i_a + (d'_b + d_0) i_b + (d'_c + d_0) i_c \\ i_+ - i_- &= -i_{neu} = (d'_a + d_0)|i_a| + (d'_b + d_0)|i_b| + (d'_c + d_0)|i_c| \end{aligned} \tag{4.33}$$

Take equation (4.33) into (4.29), applying the fact that the power in abc-frame equals to that in dq-frame ($d'^T_{a,b,c} i_{a,b,c} = d'^T_{dq0} i_{dq0}$). we have

$$\begin{cases} C\dfrac{dv_o}{dt} = d'^T_{a,b,c} i_{a,b,c} - 2\dfrac{V_o}{R_L} = d'^T_{dq0} i_{dq0} - 2\dfrac{V_o}{R_L} \\ C\dfrac{d\Delta v}{dt} = d'^T_{a,b,c} |i_{a,b,c}| + d_0(|i_a| + |i_b| + |i_c|) \end{cases} \tag{4.34}$$

A proof of (4.34) can be stated as follows. Due to the power conservation in abc-frame and dq-frame, we yield

$$u^T_{abc} i_{abc} = u^T_{dq0} i_{dq0} \tag{4.35}$$

Substitute (4.25) into (4.35), we have

$$\begin{aligned} & u^T_{dq0} i_{dq0} = L(\frac{di_{abc}}{dt})^T i_{abc} + \frac{V_o}{2} d'^T_{abc} i_{abc} \\ \Rightarrow & u^T_{abc} T^T_{dq0} i_{dq0} = L(\frac{di_{abc}}{dt})^T i_{abc} + \frac{V_o}{2} d'^T_{abc} i_{abc} \\ \Rightarrow & [L\frac{di_{abc}}{dt} + \frac{V_o}{2} d'_{abc}]^T T^T_{dq0} i_{dq0} = L(\frac{di_{abc}}{dt})^T i_{abc} + \frac{V_o}{2} d'^T_{abc} i_{abc} \\ \Rightarrow & L(\frac{di_{abc}}{dt})^T T^T_{dq0} i_{dq0} + \frac{V_o}{2} d'^T_{dq0} i_{dq0} = L(\frac{di_{abc}}{dt})^T i_{abc} + \frac{V_o}{2} d'^T_{abc} i_{abc} \\ \Rightarrow & \frac{V_o}{2} d'^T_{dq0} i_{dq0} = \frac{V_o}{2} d'^T_{abc} i_{abc} \\ \Rightarrow & d'^T_{dq0} i_{dq0} = d'^T_{abc} i_{abc} \end{aligned} \tag{4.36}$$

In the following section, we are going to design the voltage controller of three-phase Vienna rectifier based on (4.34).

4.2.5 Control of Three-Phase Vienna Circuit

The current control loop of the three-phase PFC can be obtained as shown in Figure 4.15. Feed-forward blocks are incorporated to compensate for the cross-coupling turns observed in (4.27). Since the parameters in the process of d and q axis are identical, same controller can be used to control d and q axis. The three-phase PFC circuit parameters are shown in Table 4.2. To compare the performance of single-phase and three-phase PFC, the inductor and capacitor values are identical. Three-phase PFC has a higher load R_L but a lower switching frequency, which can lead to higher THD and output voltage ripple.

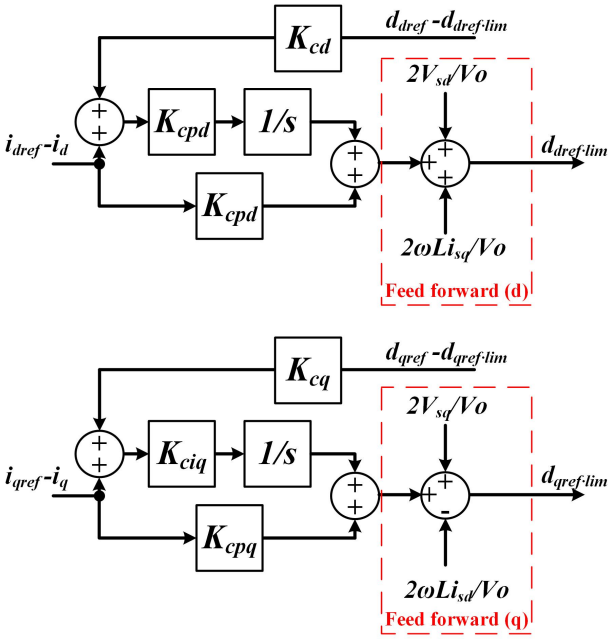

Figure 4.15: The block diagrams of current control loop in Three-phase PFC

Parameter	Value	Parameter	Value	Parameter	Value
R_L	13Ω	L	500μH	C	500μF
D	$[0.2, 0.5]$	V_{oref}	800V	f_{sw}	50kHz
V_s	230V	V_r	1	f_{grid}	50Hz

Table 4.2: The parameters of three-phase PFC

4.2.5.1 Current controller design

The bode diagram of the process of the current controller is shown in Figure 4.16. To make the current loop faster, the open-loop bandwidth of current loop is selected as f_c = 5kHz, which is still 1/10 of switching frequency. Apply (4.14) and

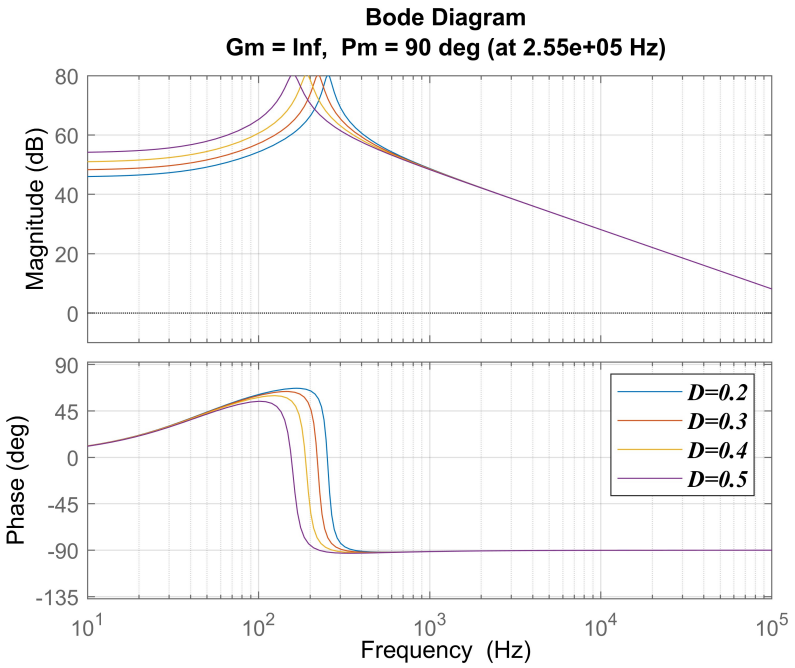

Figure 4.16: Bode plot of the process $H_c(s)$ for the current loop of the three-phase PFC

(4.15) again and one can yield $k_{icd} = k_{icq} = -541.6$ and $k_{pcd} = k_{pcq} = -0.03$. The gain in the anti-windup can be calculated using (4.17), with the anti-windup bandwidth set to twice the switching frequency $f_c = 2f_{sw} = 100$kHz. Then we have $k_{cd} = k_{cq} = -1160$.

Finally, the bode diagram of the current loop of dq controller is shown in Figure 4.17. The current loop exhibits a bandwidth of $f_c = 4.51$kHz with a phase margin $\phi_m = 57.4°$.

4.2.5.2 Voltage controller design

The voltage controller is required not only to track the output voltage reference V_{oref}, but also to minimize the voltage unbalance between capacitor voltage v_{C1} and v_{C2}. In this thesis, a PI controller is designed to let the output voltage follow the reference. The zero sequence duty cycle is utilized to reduce the voltage unbalance. According to (4.18), the bode plots of voltage process $H_v(s)$ under different duty cycle conditions can be obtained. The parameters used in three-phase PFC are identical to that of single-phase PFC, the bode diagrams for the voltage process $H_v(s)$ are the same, as shown in Figure 4.8.

The PI parameters are calculated based on (4.19). The bandwidth is selected as $f_c = 25Hz$ with a phase margin $\phi_m = 70\circ$. Then the proportion and integration gain can be obtained as $k_{vp} = 0.1$ and $k_{vi} = 8.56$. The voltage loop gain $G_v(s)$ is shown in Figure 4.18.

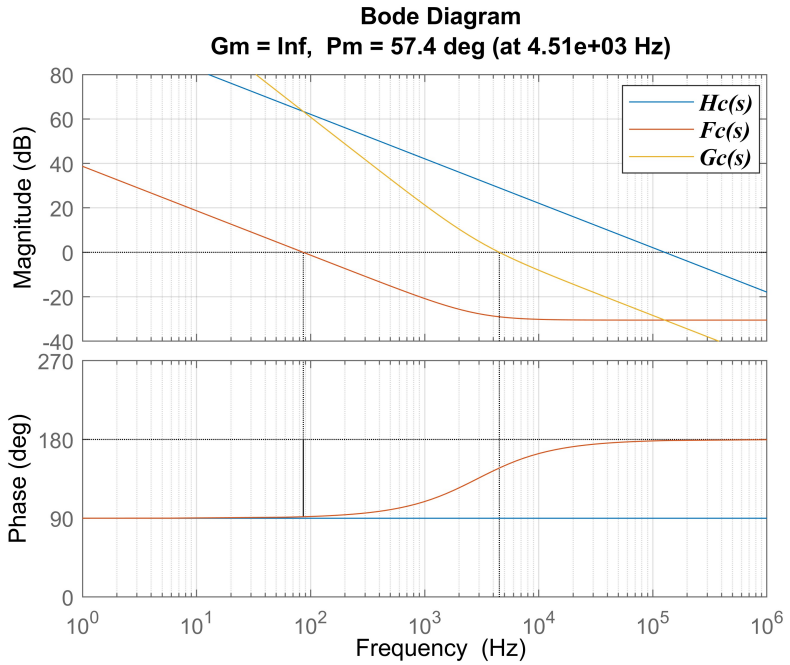

Figure 4.17: Bode plot of the current loop $G_c(s)$ of the three-phase PFC

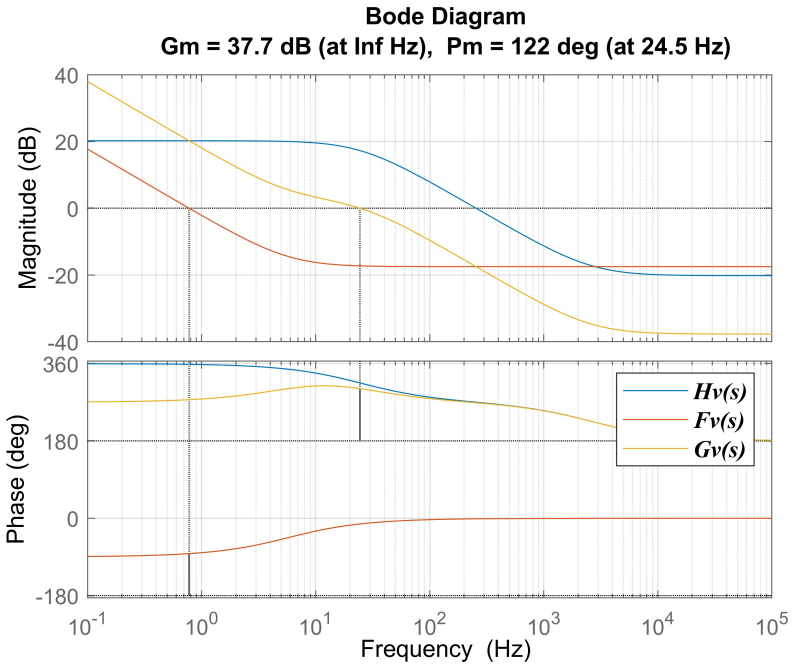

Figure 4.18: Bode plot of the voltage loop $G_v(s)$ of the three-phase PFC

To reduce the voltage unbalance on the output capacitor, an extra unbalance voltage controller is designed as shown in Figure 4.19. It can be found from equation (4.34) that the unbalance voltage Δv is related to the zero-sequence duty cycle d_0. Further define $d_0 = D_0 + \Delta d_0$, where

$$\begin{aligned} 0 &= d'_a|i_a| + d'_b|i_b| + d'_c|i_c| + D_0(|i_a| + |i_b| + |i_c|) \\ \Rightarrow D_0 &= -\frac{d'_a|i_a| + d'_b|i_b| + d'_c|i_c|}{|i_a| + |i_b| + |i_c|} \\ \Rightarrow C\frac{d\Delta v}{dt} &= \Delta d_0(|i_a| + |i_b| + |i_c|) \end{aligned} \tag{4.37}$$

with source current i_a, i_b, and i_c

$$\begin{cases} i_a = \sqrt{2}I_s\cos(\omega t) \\ i_b = \sqrt{2}I_s\cos(\omega t - \frac{2\pi}{3}) \\ i_c = \sqrt{2}I_s\cos(\omega t + \frac{2\pi}{3}) \end{cases} \tag{4.38}$$

On the one hand, take the average value on $C\frac{d\Delta v}{dt}$, we yield

$$\begin{aligned} C\frac{d\Delta v}{dt} &= \Delta d_0 \frac{24}{T}\int_0^{\frac{T}{12}}(|i_a| + |i_b| + |i_c|)dt \\ \Rightarrow C\frac{d\Delta v}{dt} &= \Delta d_0 \frac{6\sqrt{2}}{\pi} I_s \end{aligned} \tag{4.39}$$

Thus, the transfer gain $H_0(s)$ can be obtained as

$$H_0(s) = \frac{\Delta v}{\Delta d_0} = \frac{6\sqrt{2}I_s}{\pi C s} \tag{4.40}$$

On the other hand, the zero-sequence component D_0 in (4.37) can be rearranged as

$$\begin{aligned} D_0 = K\frac{\cos(\omega t)|\cos(\omega t)| + \cos(\omega t - \frac{2\pi}{3})|\cos(\omega t - \frac{2\pi}{3})| + \cos(\omega t + \frac{2\pi}{3})|\cos(\omega t + \frac{2\pi}{3})|}{|\cos(\omega t)| + |\cos(\omega t - \frac{2\pi}{3})| + |\cos(\omega t + \frac{2\pi}{3})|} \\ \Rightarrow D_0 \approx -\frac{K}{4}cos(3\omega t) \end{aligned} \tag{4.41}$$

where $K = \frac{\sqrt{2}V_s}{V_o}$. The unbalance voltage controller can be obtained as shown in Figure 4.19. The proportional gain $k_{p0} = 0.8$.

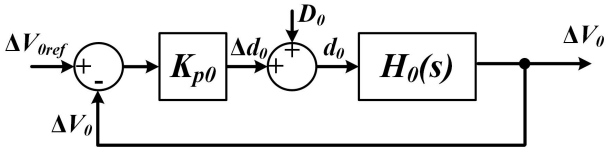

Figure 4.19: Block diagram for the unbalance voltage controller

4.2.6 Simulation on Three Phasse Vienna Rectifier

4.2.6.1 Introduction to the simulation setup

To sum up, the controller setup of three-phase PFC is shown in Figure 4.20. The voltage reference V_{oref} is changed from 800V to 640V at time $t = 0.7$s.

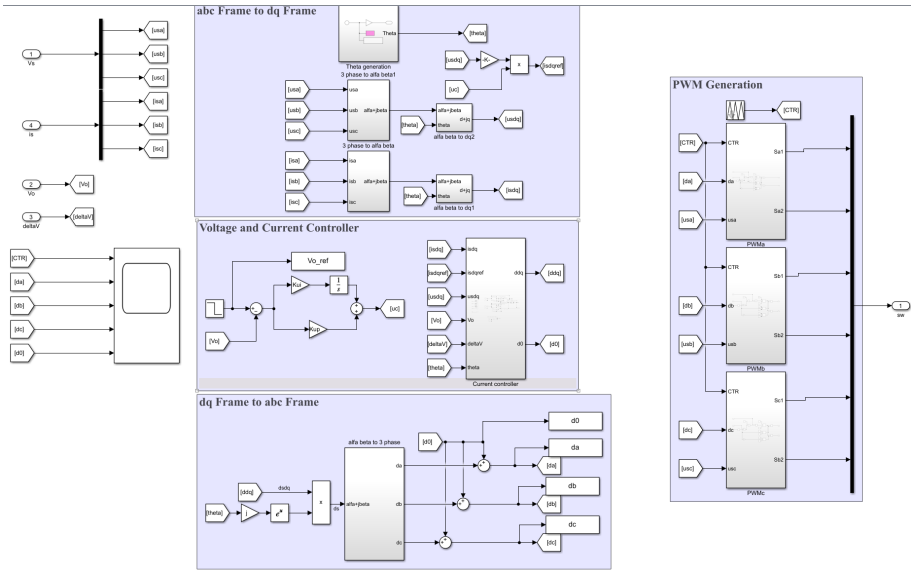

Figure 4.20: The controller setup of three-phase PFC simulation

4.2.6.2 Result and analysis

The output voltage V_o and the reference voltage V_{oref} are shown in Figure 4.21. It's evident that the output voltage quickly drops at $t = 0.7$s due to the proportion gain set for the voltage controller k_{vp}. The system reaches steady state with $V_o = V_{oref}$ at $t = 1.2$s due to the integral gain set for the voltage controller k_{vi}. Compared with the output voltage of single-phase PFC in Figure 4.10, it's notable that the three-phase PFC exhibits much lower output voltage ripple.

The capacitor voltage and the unbalance voltage are illustrated in Figure 4.22. Due to the working mode of three-phase PFC shown in Figure 4.14, there is a small unbalance voltage ripple between the output capacitors. Upon closer inspection, it can be found that the unbalance voltage ripple has a frequency of approximately 200Hz. Additionally, the magnitude of unbalance voltage is related to the output voltage. As the output voltage decrease from $V_o = 800$V to $V_o = 640$V, the unbalance voltage magnitude decreases from $\Delta V_{peak} = 1$V to $\Delta V_{peak} = 0.6$V.

The input source voltage and source current are depicted in Figure 4.23. The duty cycle d_a, d_b, d_c and d_0 are shown in Figure 4.24 (Note that $d'_\sigma = 1 - d_\sigma$). The FFT analysis result on i_a is shwon in Figure 4.25. The three-phase PFC not only has a lower total harmonic THD = 2.47%, but also demonstrates lower third and fifth order harmonic components, which are the major concerns in the requirements.

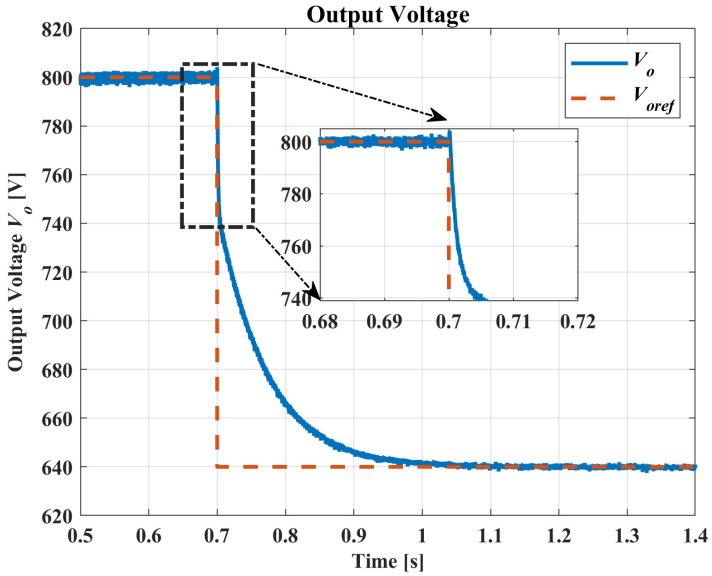

Figure 4.21: The output voltage and reference output voltage of the three-phase PFC

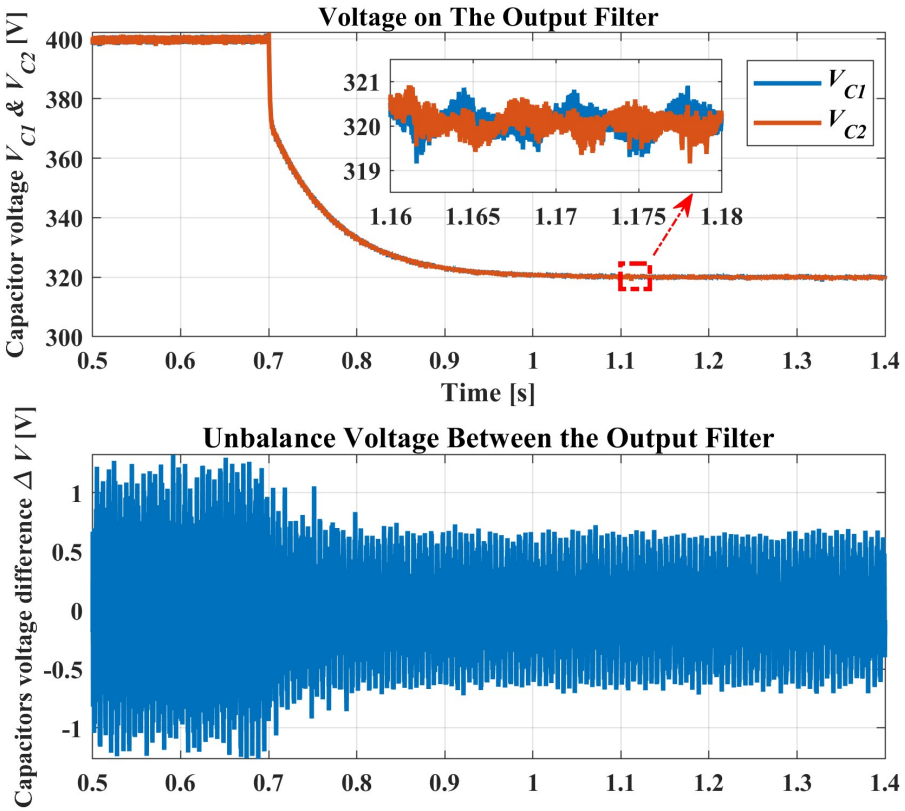

Figure 4.22: The voltage on the capacitors of the three-phase PFC

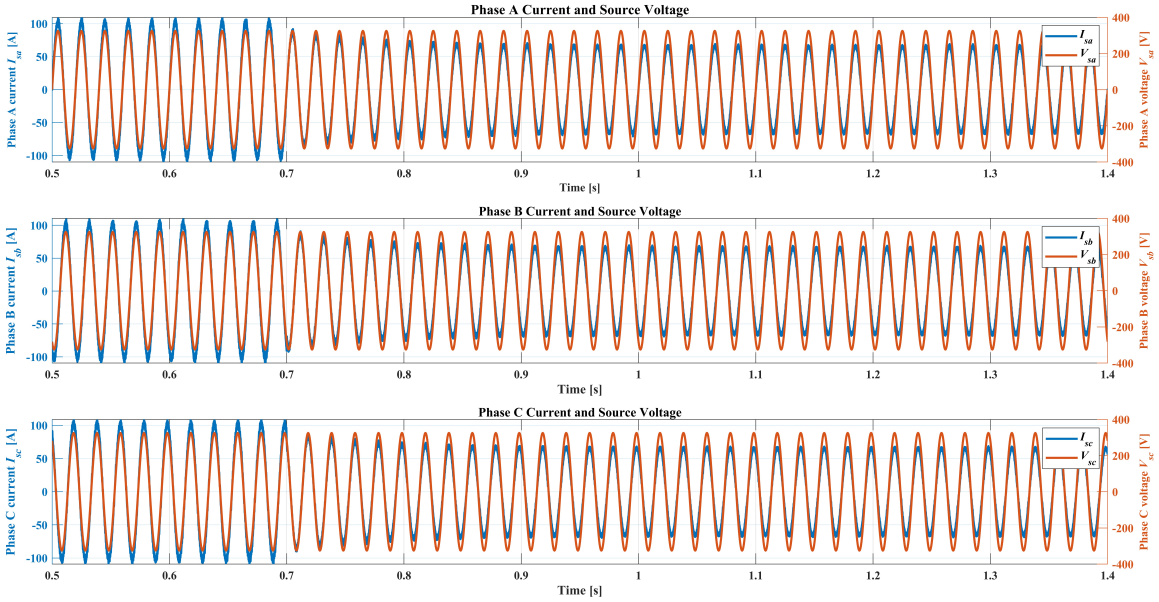

Figure 4.23: The input voltage and source current of three-phase PFC

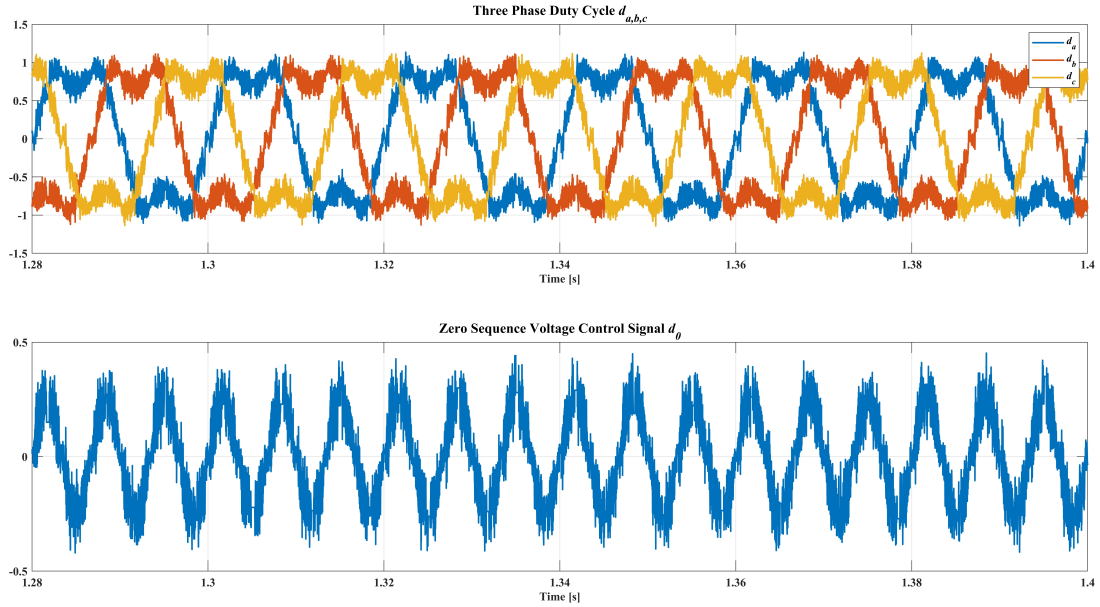

Figure 4.24: The duty cycle of the three-phase PFC

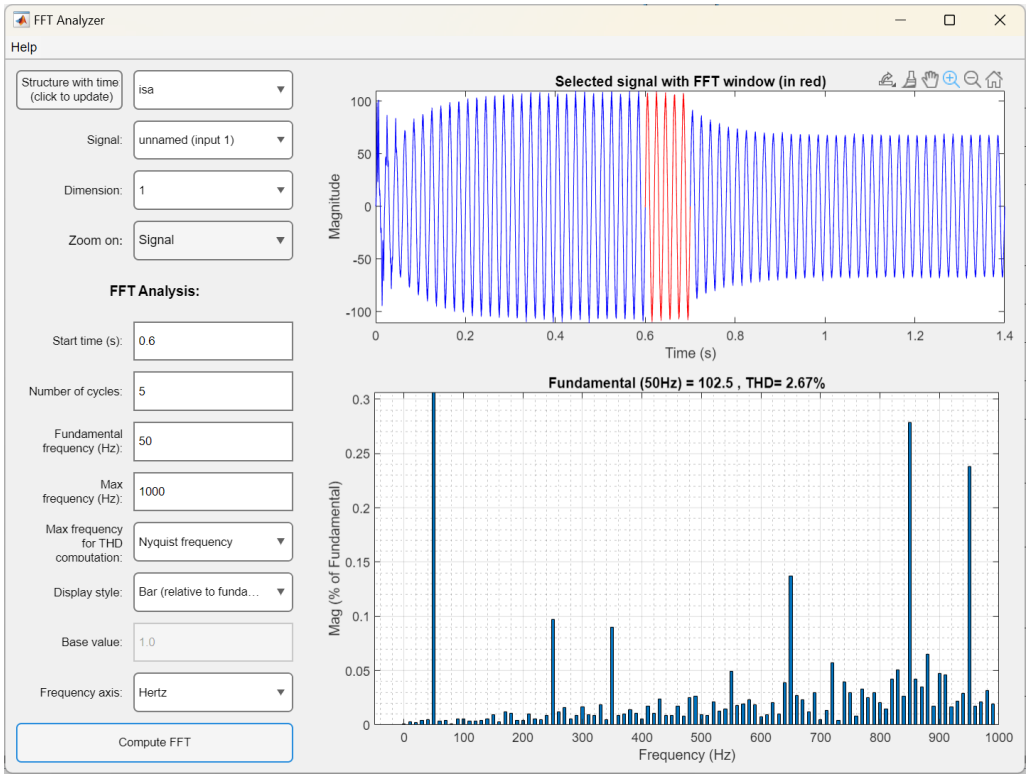

Figure 4.25: The FFT analysis on the input current (phase A) of the three-phase PFC

5

Conclusion

Inductive power transfer (IPT) emerges as a promising solution for Electric Vehicle (EV) charging. This thesis is dedicated to the meticulous modelling and control of an IPT system, aiming to achieve a solution with robustness, high efficiency, and adaptability for EV and ferry charging applications. The system integrates a dynamically adjustable working frequency mode alongside a DC-link voltage tuning strategy. Employing SiC MOSFETs in the power inverter and rectifier facilitates the pursuit of heightened efficiency. Consequently, the system shows the ability to output specific power with high efficiency, irrespective of variations in coupling factor and load characteristics.

An initial focus on understanding the electromagnetic field surrounding the magnetic coupler reveals the significant influence of the inductive charging pad's geometry on IPT system parameters such as self inductance and mutual inductance. Subsequently, this thesis proceeds with the modelling of IPT system. First, the conventional fixed-frequency operational mode of the IPT system is investigated. Theoretical formulations for the system's output power and efficiency are derived. The simulation and experiment result are compared for this working mode. Notably, under fixed-frequency conditions with an 85.5kHz switching frequency, the system's output power is observed to fluctuate with alterations in coupling factor. Specifically, as the coupling factor ascends from 0.2 to 0.6, the output power of system decreases significantly. To obtain a high output power, low coupling condition is preferred. However, the transmission efficiency of fundamental component is getting lower as the coupling decreases. Moreover, the investigation reveals the lurking risk of overload under low coupling conditions. Thus, prioritizing a control strategy that ensures consistent output power and efficiency amidst varying coupling conditions emerges as imperative.

Upon further investigation into the system, it becomes evident that synchronizing the inverter output voltage with the transmission current yields constant output power under varying coupling factor conditions. This assertion is substantiated by simulation and experimental results, wherein, within a misalignment range of 0-160 mm, the system exhibits nearly constant output power with a 10Ω load, while the working frequency varies from 68.5kHz to 74kHz. However, the control scheme faces challenges due to the inherent propagation delays in the control circuit, leading to frequency drift and heightened switching losses. Consequently, system efficiency and output power suffer. To address this issue, a digital compensation scheme for the IPT system is proposed. Experimental findings demonstrate that this scheme

effectively compensates for delays without necessitating additional compensation circuits. Notably, constant output power is achieved upon full delay compensation. Furthermore, employing over-compensation enables soft switching, thereby enhancing DC-DC efficiency. The proposed control scheme stands to enhance the robustness and efficiency of wireless charging systems. Its implementation in hardware experiments is straightforward, requiring no high-precision processors.

Additionally, methods are proposed to exert control over the output power of the charging system. One approach involves activating the receiving-end rectifier to adjust the equivalent load of the IPT system. However, this control scheme introduces instability in the working frequency. Nonetheless, it represents a competitive solution for power control, as it necessitates no communication and holds the potential to expand the coupling-independent range. Apart from that, one can also control the output power by tunning the DC-link voltage, which requires the control of grid connected rectifier.

The trend toward reduced active switching devices, high input power factor, and low device voltage stress has significantly influenced the design of grid-connected rectifiers. This thesis delves into the modelling and control aspects of grid-connected rectifiers. Initially, controller design is elucidated for a single-phase rectifier and then extended to a three-phase Vienna rectifier. The simulation result shows that the input current THD of a three-phase Vienna rectifier is 2.67%, with the output voltage ripple remaining below 2V under conditions of 800V output voltage, 50kW output power, and a switching frequency of 50kHz. Furthermore, the unbalance voltage between two output power capacitors is controlled to within 1V.

Further study concerning the modeling of the transient state of PT-symmetric IPT systems will aid in determining the stability of such systems. The implementation of the receiving-end rectifier control scheme, as introduced in this thesis, remains incomplete. A more thorough analysis of this scheme is imperative to foster the development of a simpler, more efficient, and reliable IPT structure. Additionally, the implementation of an active rectifier at the receiving end enables bi-directional power flow, thereby significantly enhancing the flexibility of power delivery.

Bibliography

[1] P. R. Shukla, J. Skea, R. Slade, and A. Al Khourdajie, eds., *Climate Change 2022: Impacts, Adaptation and Vulnerability. Contribution of Working Group III to the Sixth Assessment Report of the Intergovernmental Panel on Climate Change.* 2022.

[2] H. Ritchie and M. Roser, "Sector by sector: Where do global greenhouse gas emissions come from?," *Our World in Data*, 2024.

[3] H. Ritchie and M. Roser, "Cars, planes, trains: Where do CO2 emissions from transport come from?," *Our World in Data*, 2024.

[4] "Executive summary – Global EV Outlook 2023 – Analysis." `https://www.iea.org/reports/global-ev-outlook-2023/executive-summary` Last accessed on 2024-03-27.

[5] "Decarbonising Maritime Transport: The Case of Sweden." `https://www.itf-oecd.org/decarbonising-maritime-transport-sweden` Last accessed on 2024-03-27.

[6] N. Campagna, V. Castiglia, F. Pellitteri, R. Miceli, and M. Caruso, "Opportunity charging for public transportation: Opportunities and challenges," in *2023 IEEE International Conference on Electrical Systems for Aircraft, Railway, Ship Propulsion and Road Vehicles & International Transportation Electrification Conference (ESARS-ITEC)*, pp. 1–4.

[7] A. Mikheenkova, A. J. Smith, K. B. Frenander, Y. Tesfamhret, N. R. Chowdhury, C.-W. Tai, T. Thiringer, R. W. Lindström, M. Hahlin, and M. J. Lacey, "Ageing of High Energy Density Automotive Li-Ion Batteries: The Effect of Temperature and State-of-Charge," *J. Electrochem. Soc.*, vol. 170, no. 8, p. 080503, 2023.

[8] N. R. Chowdhury, A. J. Smith, K. Frenander, A. Mikheenkova, R. W. Lindström, and T. Thiringer, "Influence of state of charge window on the degradation of Tesla lithium-ion battery cells," *Journal of Energy Storage*, vol. 76, p. 110001, 2024.

[9] A. A. S. Mohamed, A. A. Shaier, H. Metwally, and S. I. Selem, "A comprehensive overview of inductive pad in electric vehicles stationary charging," *Applied Energy*, vol. 262, p. 114584, 2020.

[10] Z. Li, S. Dong, K. Song, C. Zhu, Q. Zhang, and X. Huang, "Adaptive position alignment for wireless charging system with mutual inductance estimation and P&O algorithms employ only primary-side electrical parameters," *IET Power Electronics*, vol. 12, no. 10, pp. 2493–2500, 2019.

[11] D. Pehrman, *Design Aspects of Inductive Power Transfer Systems for Electric Vehicle Charging.* PhD thesis, Chalmers University of Technology, 2019.

[12] Y. Liu, R. Mai, D. Liu, Y. Li, and Z. He, "Efficiency Optimization for Wireless Dynamic Charging System With Overlapped DD Coil Arrays," *IEEE Transactions on Power Electronics*, vol. 33, no. 4, pp. 2832–2846, 2018.

[13] C. Wang, C. Zhu, K. Song, G. Wei, S. Dong, and R. G. Lu, "Primary-side control method in two-transmitter inductive wireless power transfer systems for dynamic wireless charging applications," in *2017 IEEE PELS Workshop on Emerging Technologies: Wireless Power Transfer (WoW)*, pp. 1–6, 2017-05.

[14] M. M. Alam, S. Mekhilef, M. Seyedmahmoudian, and B. Horan, "Dynamic Charging of Electric Vehicle with Negligible Power Transfer Fluctuation," *Energies*, vol. 10, no. 5, p. 701, 2017-05.

[15] "Smartroad Gotland." `https://electreon.com/projects/gotland` Last accessed on 2024-01-12.

[16] "Charging – Marine vessel charging systems." `https://www.wartsila.com/marine/products/ship-electrification-solutions/shore-power/charging` Last accessed on 2024/01/12.

[17] F. João Ramos, *Dynamic Control of Wireless Charging*. PhD thesis, Técnico Lisboa, 2022.

[18] G. Jonas, *Design and Simulation of a 300 kW Inductive Charging System (IPT) for a City Bus Application*. PhD thesis, Universität Stuttgart, 2023.

[19] K. Wenlin, *Thermal and Structural Analysis of IPT Pads for Electric Ferries*. PhD thesis, Linköping Universit, 2021.

[20] S. Qayyum, *Electric Design of Fast Wireless Charging for Electric Ferries*. PhD thesis, Chalmers University of Technology, 2021.

[21] K. Song, Y. Lan, X. Zhang, J. Jiang, C. Sun, G. Yang, F. Yang, and H. Lan, "A Review on Interoperability of Wireless Charging Systems for Electric Vehicles," *Energies*, vol. 16, no. 4, p. 1653, 2023-01.

[22] M. Mohammad, O. C. Onar, J. L. Pries, V. P. Galigekere, G.-J. Su, and J. Wilkins, "Analysis of Magnetic Field Emissions and Shield Requirements for Interoperating High-Power EV Wireless Charging System," in *2021 IEEE Applied Power Electronics Conference and Exposition (APEC)*, pp. 1586–1592, IEEE, 2021-06-14.

[23] J. Huang, Y. Dou, X. Huang, Z. Zhang, Z. Ouyang, and M. A. Andersen, "Optimization of a 6.78-MHz Inductive Power Transfer System for Unmanned Aerial Vehicles," *IEEE Transactions on Power Electronics*, vol. 38, no. 10, pp. 11940–11952, 2023.

[24] Z. Bie, J. Zhang, K. Song, D. Wang, and C. Zhu, "A Free-Rotation Asymmetric Magnetic Coupling Structure of UAV Wireless Charging Platform With Conformal Pickup," *IEEE Transactions on Industrial Electronics*, vol. 69, no. 10, pp. 10154–10161, 2022.

[25] D. Pehrman and Y. Liu, "Design and Stray Field Evaluation of Inductive Power Transfer in Electric Vehicle Charging," in *2019 Fourteenth International Conference on Ecological Vehicles and Renewable Energies (EVER)*, pp. 1–6, 2019-05.

[26] K. N. Mude and K. Aditya, "Comprehensive review and analysis of two-element resonant compensation topologies for wireless inductive power transfer sys-

tems," *Chinese Journal of Electrical Engineering*, vol. 5, no. 2, pp. 14–31, 2019-06.

[27] C. Liu, D. Thrimawithana, G. Covic, and M. Kesler, "A Novel Active Impedance Compression Network for IPT EV Charging," in *2023 IEEE Wireless Power Technology Conference and Expo (WPTCE)*, pp. 1–6, 2023-06.

[28] C. Liu, D. J. Thrimawithana, G. A. Covic, and M. Kesler, "Active Impedance Control for Inductive Charging of Electric Vehicles," in *2020 IEEE PELS Workshop on Emerging Technologies: Wireless Power Transfer (WoW)*, pp. 16–20, 2020-11.

[29] A. S. Jurkov, A. Radomski, and D. J. Perreault, "Tunable Matching Networks Based on Phase-Switched Impedance Modulation1," *IEEE Transactions on Power Electronics*, vol. 35, no. 10, pp. 10150–10167, 2020.

[30] E. S. Lee, B. G. Choi, J. S. Choi, D. T. Nguyen, and C. T. Rim, "Wide-Range Adaptive IPT Using Dipole-Coils With a Reflector by Variable Switched Capacitance," *IEEE Transactions on Power Electronics*, vol. 32, no. 10, pp. 8054–8070, 2017.

[31] L. Chen, S. Liu, Y. C. Zhou, and T. J. Cui, "An Optimizable Circuit Structure for High-Efficiency Wireless Power Transfer," *IEEE Trans. Ind. Electron.*, vol. 60, no. 1, pp. 339–349, 2013.

[32] C. Cui, D. Pehrman, Y. Liu, and Q. Zhang, "Zero Voltage Switching for High Power Threephase Inductive Power Transfer with a Dual Active Bridge," *IEEE Access*, pp. 1–1, 2024.

[33] C. Cui, Y. Liu, D. Pehrman, X. Huang, and Q. Zhang, "A Full Power Range ZVS Control Technology for Bidirectional Inductive Power Transfer System," in *IECON 2020 The 46th Annual Conference of the IEEE Industrial Electronics Society*, pp. 3861–3865, 2020.

[34] E. S. Lee, "Frequency-Modulation-Based IPT With Magnetic Communication for EV Wireless Charging," *IEEE Transactions on Industrial Electronics*, vol. 70, no. 2, pp. 1398–1408, 2023.

[35] E. Gati, G. Kampitsis, and S. Manias, "Variable Frequency Controller for Inductive Power Transfer in Dynamic Conditions," *IEEE Trans. Power Electron.*, vol. 32, no. 2, pp. 1684–1696, 2017.

[36] N. T. Diep, N. K. Trung, and T. T. Minh, "Power Control in the Dynamic Wireless Charging of Electric Vehicles," in *2019 10th International Conference on Power Electronics and ECCE Asia (ICPE 2019 - ECCE Asia)*, pp. 1–6, 2019.

[37] S. Assawaworrarit, X. Yu, and S. Fan, "Robust wireless power transfer using a nonlinear parity–time-symmetric circuit," *Nature*, vol. 546, no. 7658, pp. 387–390, 2017.

[38] J. Zhou, B. Zhang, W. Xiao, D. Qiu, and Y. Chen, "Nonlinear Parity-Time-Symmetric Model for Constant Efficiency Wireless Power Transfer: Application to a Drone-in-Flight Wireless Charging Platform," *IEEE Transactions on Industrial Electronics*, vol. 66, no. 5, pp. 4097–4107, 2019-05.

[39] L. Wu, B. Zhang, and Y. Jiang, "Position-Independent Constant Current or Constant Voltage Wireless Electric Vehicles Charging System Without Dual-

Side Communication and DC–DC Converter," *IEEE Transactions on Industrial Electronics*, vol. 69, no. 8, pp. 7930–7939, 2022-08.

[40] C.-S. Wang, G. Covic, and O. Stielau, "Power transfer capability and bifurcation phenomena of loosely coupled inductive power transfer systems," *IEEE Transactions on Industrial Electronics*, vol. 51, no. 1, pp. 148–157, 2004-02.

[41] D. Iannuzzi, L. Rubino, L. P. Di Noia, G. Rubino, and P. Marino, "Resonant inductive power transfer for an E-bike charging station," *Electric Power Systems Research*, vol. 140, pp. 631–642, 2016.

[42] S. Assawaworrarit and S. Fan, "Robust and efficient wireless power transfer using a switch-mode implementation of a nonlinear parity–time symmetric circuit," *Nat Electron*, vol. 3, no. 5, pp. 273–279, 2020.

[43] R. Okada, R. Ota, and N. Hoshi, "Novel Soft-Switching Active-Bridge Converter for Bi-directional Inductive Power Transfer System," *IEEJ Journal IA*, vol. 11, no. 1, pp. 97–107, 2022-01-01.

[44] R. Ota, D. J. Thrimawithana, U. K. Madawala, and G. A. Covic, "Boundary of Soft-switching for Efficient Operation of Bi-directional IPT Systems," in *2020 IEEE PELS Workshop on Emerging Technologies: Wireless Power Transfer (WoW)*, pp. 164–169, 2020-11.

[45] Y. Zhao, Y. Li, and T. A. Lipo, "Force Commutated Three Level Boost Type Rectifier," *IEEE Transactions on Industry Applications*, vol. 31, no. 1, pp. 155–161, 1995-01.

[46] H. Kanaan, K. Al-Haddad, R. Chaffai, L. Duguay, and F. Fnaiech, "A new low-frequency state model of a three-phase three-switch three-level fixed-frequency PWM rectifier," in *2001 Twenty-Third International Telecommunications Energy Conference INEC 2001*, pp. 384–391, 2001.

[47] N. Backman and R. Rojas, "Modern circuit topology enables compact power factor corrected three-phase rectifier module," in *24th Annual International Telecommunications Energy Conference*, pp. 107–114, IEEE, 2002.

[48] Rixin Lai, Fei Wang, R. Burgos, D. Boroyevich, Dong Jiang, and Di Zhang, "Average Modeling and Control Design for VIENNA-Type Rectifiers Considering the DC-Link Voltage Balance," *IEEE Trans. Power Electron.*, vol. 24, no. 11, pp. 2509–2522, 2009-11.

DEPARTMENT OF SOME SUBJECT OR TECHNOLOGY
CHALMERS UNIVERSITY OF TECHNOLOGY
Gothenburg, Sweden
www.chalmers.se

CHALMERS
UNIVERSITY OF TECHNOLOGY